

UNCLASSIFIED

AD NUMBER

AD472210

LIMITATION CHANGES

TO:

Approved for public release; distribution is unlimited.

FROM:

Distribution authorized to U.S. Gov't. agencies and their contractors;
Administrative/Operational Use; OCT 1965. Other requests shall be referred to Arnold Engineering Development Center, Arnold AFB, TN.

AUTHORITY

AEDC ltr 23 Jan 1980

THIS PAGE IS UNCLASSIFIED

AEDC-TR-65-195

^{by}
**ARCHIVE COPY
DO NOT LOAN**



**AN INVESTIGATION AND CALIBRATION
OF A DEVICE FOR THE GENERATION
OF TURBULENT FLOW AT THE INLET
OF A TURBOJET ENGINE**

PROPERTY OF U.S. AIR FORCE
AEDC TECHNICAL LIBRARY

TECHNICAL REPORTS
FILE COPY

W. F. Kimzey

ARO, Inc.

This document has been approved for public release
and its distribution is unlimited. *per TAB No 80-8*

October 1965



PROPERTY OF U.S. AIR FORCE
AEDC LIBRARY
AF 40(600)1200

**ROCKET TEST FACILITY
ARNOLD ENGINEERING DEVELOPMENT CENTER
AIR FORCE SYSTEMS COMMAND
ARNOLD AIR FORCE STATION, TENNESSEE**

AEDC TECHNICAL LIBRARY



5 0720 00031 1375

NOTICES

When U. S. Government drawings specifications, or other data are used for any purpose other than a definitely related Government procurement operation, the Government thereby incurs no responsibility nor any obligation whatsoever, and the fact that the Government may have formulated, furnished, or in any way supplied the said drawings, specifications, or other data, is not to be regarded by implication or otherwise, or in any manner licensing the holder or any other person or corporation, or conveying any rights or permission to manufacture, use, or sell any patented invention that may in any way be related thereto.

Qualified users may obtain copies of this report from the Defense Documentation Center.

References to named commercial products in this report are not to be considered in any sense as an endorsement of the product by the United States Air Force or the Government.

Defense Documentation Center release to the Clearinghouse for Federal, Scientific, and Technical Information (CFSTI) and foreign announcement and dissemination are prohibited. The distribution of this report is limited because it contains technology identifiable with items excluded from export by the Department of State.

AN INVESTIGATION AND CALIBRATION
OF A DEVICE FOR THE GENERATION
OF TURBULENT FLOW AT THE INLET
OF A TURBOJET ENGINE

W. F. Kimzey
ARO, Inc.

FOREWORD

The work reported herein was performed at the request of the Aeronautical Systems Division (ASD), Air Force Systems Command (AFSC), for the General Electric Company under Program Element 64403034, System 110A.

The results of this investigation were obtained by ARO, Inc. (a subsidiary of Sverdrup and Parcel, Inc.), contract operator of the Arnold Engineering Development Center (AEDC), AFSC, Arnold Air Force Station, Tennessee, under Contract AF 40(600)-1200. The test was conducted in Propulsion Engine Test Cell (J-1) of the Rocket Test Facility (RTF) from September 8 to November 3, 1964, under ARO Project No. RJ0374, and the manuscript was submitted for publication on August 24, 1965.

This technical report has been reviewed and is approved.

Ralph W. Everett
Major, USAF
AF Representative, RTF
DCS/Test

Jean A. Jack
Colonel, USAF
DCS/Test

ABSTRACT

An investigation and calibration of a device consisting of an airflow metering venturi with a variable position aerodynamic centerbody for the production of turbulent flow at the inlet of a turbojet engine was conducted in an altitude test cell. The device provided turbulent flow conditions by producing shock-wave systems of variable severity. Turbulence and distortion values were obtained at the front face of a simulated turbojet engine compressor inlet located slightly downstream of the turbulence producing device. Various screen configurations with area blockages of from zero to 70 percent were inserted between the device and the simulator front face, and their effect on distortion and turbulence characteristics at several different corrected airflow settings was determined. Wave analysis techniques were applied to the turbulent pressure data, and the effects on turbulence of Reynolds number, corrected airflow, centerbody position, and screen configuration were determined. Values of peak-to-peak turbulent pressure amplitude up to 28.4 (0- to 50-cps bandwidth) and 57.0 (0- to 600-cps bandwidth) percent of the steady-state total pressure level were obtained with total pressure distortion values up to 52 percent. An airflow coefficient for the turbulence generating device and the structural integrity of the apparatus were also determined.

CONTENTS

	<u>Page</u>
ABSTRACT	iii
NOMENCLATURE	xii
I. INTRODUCTION	1
II. APPARATUS	
2.1 Test Article	2
2.2 Installation	3
2.3 Instrumentation	3
III. PROCEDURE	6
IV. RESULTS AND DISCUSSION	
4.1 Basic Turbulence and Distortion Definitions and Analyses	8
4.2 Dependence of Turbulence on Flow Parameters and Screen Configurations	12
4.3 Turbulence and Distortion Calibration	17
4.4 Airflow Calibration	22
4.5 Structural Integrity	27
V. SUMMARY OF RESULTS	29
REFERENCES.	30
APPENDIX I - Methods of Calculation	115

ILLUSTRATIONS

Figure

1. YJ93 Airflow Simulator and Turbulence Generator . . .	31
2. Turbulence Generator	
a. Schematic	32
b. Variance of Throat Area with Centerbody Immersion Depth	33
c. Venturi and Centerbody Coordinates	34
d. Venturi Centerbody.	35
e. Venturi Centerbody Installed in Venturi	36
3. Installation of Venturi Centerbody	
a. Forward Guide Tube Supports	37
b. Aft Guide Tube Supports	38
4. YJ93 Airflow Simulator	
a. Photograph	39
b. Long Bullethead	40

<u>Figure</u>	<u>Page</u>
5. Screen Configurations	
a. Light Blockage Screen	41
b. Intermediate Blockage Screen.	42
c. Heavy Blockage Screen Configuration	43
d. Vortex Generator Screen Configuration	44
6. Installation of the YJ93 Simulator in Propulsion Engine Test Cell (J-1).	45
7. Instrumentation Station Locations	
a. Longitudinal Location of Simulator Measuring Planes	46
b. Venturi Wall Static Pressure Measuring Stations	47
8. Instrumentation Station Details (Looking Upstream)	
a. Station 00, Plenum Chamber	48
b. Station 1n-xu, Venturi Converging Wall (Upstream of Venturi Minimum Diameter)	48
c. Station 1n, Venturi Minimum Diameter	48
d. Station 1n-xd, Venturi Diverging Wall (Downstream of Venturi Minimum Diameter)	48
e. Station 2, Simulator Inlet 5.87 in. Upstream of Simulated Compressor Front Frame.	49
f. Station 7, Conic Nozzle Inlet Plane	50
g. Station 7.5, Mid-Plane of 550-in. ² Conic Nozzle	50
h. Station 8, Exit Plane of 550-in. ² Conic Nozzle	50
i. Station 8, Exit Plane of 778-in. ² Conic Nozzle	50
9. Graphical Definitions	
a. Turbulence	51
b. Distortion (Rectangular)	51
c. Distortion (Polar)	51
10. Turbulence Waveforms	
a. Open Screen Configuration, $Re_D = 1.0 \times 10^8$, $W_{ac} = 145 \text{ lbm/sec}$	52
b. Open Screen Configuration, $Re_D = 2.2 \times 10^8$, $W_{ac} = 185 \text{ lbm/sec}$	52
c. Heavy Screen Configuration, $Re_D = 1.0 \times 10^8$, $W_{ac} = 260 \text{ lbm/sec}$	52
d. Heavy Screen Configuration, $Re_D = 3.0 \times 10^8$, $W_{ac} = 260 \text{ lbm/sec}$	52

<u>Figure</u>		<u>Page</u>
11.	Typical Power Spectral Density Functions for Turbulent Pressure	
	a. Sloping Total Pressure Distribution, Open Screen Configuration, $Re_D = 1.0 \times 10^8$, $W_{ac} = 145 \text{ lb}_m/\text{sec}$	53
	b. Uniform Total Pressure Distribution, Open Screen Configuration, $Re_D = 4.0 \times 10^8$, $W_{ac} = 260 \text{ lb}_m/\text{sec}$	54
12.	Typical Auto-Correlation Functions for Turbulent Pressure	
	a. Sloping Total Pressure Distribution	55
	b. Uniform Total Pressure Distribution	55
13.	Turbulence Waveforms at Different Immersion Depth into the Airstream	56
14.	Turbulence Transmissibility	
	a. Lag Time	57
	b. Amplitude	57
15.	Variance of Turbulence Amplitude with Corrected Airflow, Open Screen Configuration	58
16.	Venturi Wall Static Pressure Distributions, $A_{an} = 110 \text{ in.}^2$, Open Screen Configuration	59
17.	Estimated Turbulence Generator Shock-Wave Systems, $A_{an} = 110 \text{ in.}^2$, Open Screen Configuration	
	a. $W_{ac} = 160 \text{ lb}_m/\text{sec}$	60
	b. $W_{ac} = 180 \text{ lb}_m/\text{sec}$	60
18.	Variance of the Normalized Turbulent Pressure Spectral Density with Corrected Airflow	61
19.	Effect on Normalized Turbulent Pressure Amplitude of Reynolds Number	
	a. $A_{an} = 110 \text{ in.}^2$	62
	b. $A_{an} = 246 \text{ in.}^2$	62
	c. $A_{an} = 410 \text{ in.}^2$	62
20.	Effect of Venturi Inlet Reynolds Number on the Normalized Turbulent Pressure Spectral Density	
	a. $W_{ac} = 145 \text{ lb}_m/\text{sec}$	63
	b. $W_{ac} = 260 \text{ lb}_m/\text{sec}$	64
21.	Variance of Turbulence Amplitude with Annulus Area, Open Screen Configuration, $W_{ac} = 145 \text{ lb}_m/\text{sec}$	
	a. 0- to 50-cps Bandwidth	65
	b. 0- to 600-cps Bandwidth	65

<u>Figure</u>	<u>Page</u>
21. Continued	
c. Single Probe, 0- to 200-cps Bandwidth	65
d. Estimated Wall Static Pressure, 0- to 2000-cps Bandwidth	65
22. Relative Turbulence Amplitude Radial Distribution, Open Screen Configuration, $W_{ac} = 145 \text{ lb}_m/\text{sec}$	
a. $A_{an} = 410 \text{ in.}^2$	66
b. $A_{an} = 246 \text{ in.}^2$	66
c. $A_{an} = 110 \text{ in.}^2$	66
23. Normalized Turbulent Pressure Spectral Density, Open Screen Configuration, $W_{ac} = 145 \text{ lb}_m/\text{sec}$	
a. $A_{an} = 410 \text{ in.}^2$	67
b. $A_{an} = 246 \text{ in.}^2$	67
c. $A_{an} = 110 \text{ in.}^2$	67
24. Total Pressure Distortion Characteristics, Open Screen Configuration, $W_{ac} = 145 \text{ lb}_m/\text{sec}$	
a. Variance with Annulus Area	68
b. Distortion Pattern, $A_{an} = 410 \text{ in.}^2$	69
c. Distortion Pattern, $A_{an} = 246 \text{ in.}^2$	69
d. Distortion Pattern, $A_{an} = 110 \text{ in.}^2$	69
25. Variance of Turbulence Amplitude with Annulus Area, Open Screen Configuration, $W_{ac} = 260 \text{ lb}_m/\text{sec}$	
a. 0- to 50-cps Bandwidth	70
b. 0- to 600-cps Bandwidth	70
c. Single Probe, 0- to 200-cps Bandwidth	70
d. Estimated Wall Static Pressure, 0- to 2000-cps Bandwidth	70
26. Relative Turbulence Amplitude Radial Distribution, Open Screen Configuration, $W_{ac} = 260 \text{ lb}_m/\text{sec}$	
a. $A_{an} = 410 \text{ in.}^2$	71
b. $A_{an} = 246 \text{ in.}^2$	71
c. $A_{an} = 110 \text{ in.}^2$	71
27. Normalized Turbulent Pressure Spectral Density, Open Screen Configuration, $W_{ac} = 260 \text{ lb}_m/\text{sec}$	
a. $A_{an} = 410 \text{ in.}^2$	72
b. $A_{an} = 246 \text{ in.}^2$	72
c. $A_{an} = 110 \text{ in.}^2$	72
28. Total Pressure Distortion Characteristics, Open Screen Configuration, $W_{ac} = 260 \text{ lb}_m/\text{sec}$	
a. Variance with Annulus Area	73
b. Distortion Pattern, $A_{an} = 410 \text{ in.}^2$ (Slip Ring Leadout Strut at Normal Position).	74

<u>Figure</u>		<u>Page</u>
28.	Continued	
	c. Distortion Pattern, $A_{an} = 246 \text{ in.}^2$ (Slip Ring Leadout Strut at 0-deg Position)	74
	d. Distortion Pattern, $A_{an} = 246 \text{ in.}^2$ (Slip Ring Leadout Strut at Normal Position)	74
	e. Distortion Pattern, $A_{an} = 110 \text{ in.}^2$ (Slip Ring Leadout Strut at 0-deg Position)	74
29.	Variance of Turbulence Amplitude with Annulus Area, Light Blockage Screen Configuration, $W_{ac} = 260 \text{ lb}_m/\text{sec}$	
	a. 0- to 50-cps Bandwidth	75
	b. 0- to 600-cps Bandwidth	75
	c. Single Probe, 0- to 200-cps Bandwidth	75
	d. Estimated Wall Static Pressure, 0- to 2000-cps Bandwidth.	75
30.	Relative Turbulence Amplitude Radial Distribution, Light Blockage Screen Configuration, $W_{ac} = 260 \text{ lb}_m/\text{sec}$	
	a. $A_{an} = 410 \text{ in.}^2$	76
	b. $A_{an} = 246 \text{ in.}^2$	76
	c. $A_{an} = 110 \text{ in.}^2$	76
31.	Normalized Turbulent Pressure, Spectral Density Light Blockage Screen Configuration, $W_{ac} = 260 \text{ lb}_m/\text{sec}$	
	a. $A_{an} = 330 \text{ in.}^2$	77
	b. $A_{an} = 246 \text{ in.}^2$	77
	c. $A_{an} = 110 \text{ in.}^2$	77
32.	Total Pressure Distortion Characteristics, Light Blockage Screen Configuration, $W_{ac} = 260 \text{ lb}_m/\text{sec}$	
	a. Variance with Annulus Area.	78
	b. Distortion Pattern, $A_{an} = 410 \text{ in.}^2$	79
	c. Distortion Pattern, $A_{an} = 246 \text{ in.}^2$	79
	d. Distortion Pattern, $A_{an} = 110 \text{ in.}^2$	79
33.	Variance of Turbulence Amplitude with Annulus Area, Intermediate Blockage Screen Configuration, $W_{ac} = 260 \text{ lb}_m/\text{sec}$	
	a. 0- to 50-cps Bandwidth	80
	b. 0- to 600-cps Bandwidth	80
	c. Single Probe, 0- to 200-cps Bandwidth	80
34.	Relative Turbulence Amplitude Radial Distribution, Intermediate Blockage Screen Configuration, $W_{ac} = 260 \text{ lb}_m/\text{sec}$	
	a. $A_{an} = 410 \text{ in.}^2$	81
	b. $A_{an} = 246 \text{ in.}^2$	81
	c. $A_{an} = 110 \text{ in.}^2$	81

<u>Figure</u>	<u>Page</u>
35. Normalized Turbulent Pressure Spectral Density, Intermediate Blockage Screen Configuration, $W_{ac} = 260 \text{ lb}_m/\text{sec}$	
a. $A_{an} = 410 \text{ in.}^2$	82
b. $A_{an} = 246 \text{ in.}^2$	82
c. $A_{an} = 110 \text{ in.}^2$	82
36. Total Pressure Distortion Characteristics, Intermediate Blockage Screen Configuration, $W_{ac} = 260 \text{ lb}_m/\text{sec}$	
a. Variance with Annulus Area	83
b. Distortion Pattern, $A_{an} = 410 \text{ in.}^2$	84
c. Distortion Pattern, $A_{an} = 246 \text{ in.}^2$	84
d. Distortion Pattern, $A_{an} = 110 \text{ in.}^2$	84
37. Variance of Turbulence Amplitude with Annulus Area, Heavy Blockage Screen Configuration, $W_{ac} = 260 \text{ lb}_m/\text{sec}$	
a. 0- to 50-cps Bandwidth	85
b. 0- to 600-cps Bandwidth	85
c. Single Probe, 0- to 200-cps Bandwidth	85
38. Relative Turbulence Amplitude Radial Distribution, Heavy Blockage Screen Configuration, $W_{ac} = 260 \text{ lb}_m/\text{sec}$	
a. $A_{an} = 410 \text{ in.}^2$	86
b. $A_{an} = 246 \text{ in.}^2$	86
c. $A_{an} = 110 \text{ in.}^2$	86
39. Normalized Turbulent Pressure Spectral Density, Heavy Blockage Screen Configuration, $W_{ac} = 260 \text{ lb}_m/\text{sec}$	
a. $A_{an} = 246 \text{ in.}^2$	87
b. $A_{an} = 170 \text{ in.}^2$	87
c. $A_{an} = 110 \text{ in.}^2$	87
40. Total Pressure Distortion Characteristics, Heavy Blockage Screen Configuration, $W_{ac} = 260 \text{ lb}_m/\text{sec}$	
a. Variance with Annulus Area	88
b. Distortion Pattern, $A_{an} = 410 \text{ in.}^2$	89
c. Distortion Pattern, $A_{an} = 246 \text{ in.}^2$	89
d. Distortion Pattern, $A_{an} = 110 \text{ in.}^2$	89
41. Variance of Turbulence Amplitude with Annulus Area, Vortex Generator Screen Configuration, $W_{ac} = 260 \text{ lb}_m/\text{sec}$	
a. 0- to 50-cps Bandwidth	90
b. 0- to 600-cps Bandwidth	90
c. Single Probe, 0- to 200-cps Bandwidth	90
d. Estimated Wall Static Pressure, 0- to 2000-cps Bandwidth	90

<u>Figure</u>	<u>Page</u>
42. Relative Turbulence Amplitude Radial Distribution, Vortex Generator Screen Configuration, $W_{ac} = 260 \text{ lb}_m/\text{sec}$	
a. $A_{an} = 410 \text{ in.}^2$	91
b. $A_{an} = 246 \text{ in.}^2$	91
c. $A_{an} = 110 \text{ in.}^2$	91
43. Normalized Turbulent Pressure Spectral Density, Vortex Generator Screen Configuration, $W_{ac} = 260 \text{ lb}_m/\text{sec}$	
a. $A_{an} = 330 \text{ in.}^2$	92
b. $A_{an} = 170 \text{ in.}^2$	92
c. $A_{an} = 110 \text{ in.}^2$	92
44. Total Pressure Distortion Characteristics, Vortex Generator Screen Configuration, $W_{ac} = 260 \text{ lb}_m/\text{sec}$	
a. Variance with Annulus Area	93
b. Distortion Pattern, $A_{an} = 410 \text{ in.}^2$	94
c. Distortion Pattern, $A_{an} = 246 \text{ in.}^2$	94
d. Distortion Pattern, $A_{an} = 110 \text{ in.}^2$	94
45. Turbulence Generator Performance Map	
a. 0- to 50-cps Bandwidth	95
b. 0- to 600-cps Bandwidth	95
46. Schematic of Venturi Flow Passages	
a. $A_{an} = 410 \text{ in.}^2$	96
b. $A_{an} = 246 \text{ in.}^2$	96
c. $A_{an} = 110 \text{ in.}^2$	96
47. Variance of Venturi Annulus Airflow Measurement Plane Area with Centerbody Position	97
48. Effect of Annulus Area Change on Venturi Annulus Pressure Ratio	98
49. Reynolds Number Effect on Venturi Annulus Flow Coefficient	
a. $A_{an} = 410 \text{ in.}^2$	99
b. $A_{an} = 246 \text{ in.}^2$	99
c. $A_{an} = 110 \text{ in.}^2$	99
50. Combined Flow Coefficient Curves	
a. Open Screen Configuration	100
b. Light Blockage Screen Configuration	101
c. Intermediate and Heavy Blockage Screen Configuration	102
d. Vortex Generator Screen Configuration	103

<u>Figure</u>	<u>Page</u>
51. Simulator Inlet Flow Coefficient	
a. Variance with Distortion	104
b. Variance with Mach Number	105
52. Venturi Centerbody Deformation and Modifications	
a. Photograph	106
b. Schematics	107
53. Venturi Centerbody Loading	108
54. Turbulence Total Pressure Rake	109

TABLES

I. Screen Configurations	111
II. Index to Tabulated Data	112
III. Tabulated Data Headings.	113

NOMENCLATURE

A	Area, in. ²
B	Electrical filter bandwidth used in spectral analysis, cps
C _d	Nozzle discharge coefficient
C _f	Flow coefficient
C _t	Temperature coefficient (ratio of area at existing temperature to area at 540°R)
c _p	Specific heat at constant pressure, $\frac{\text{Btu}}{\text{lb}_m\text{-}^\circ\text{R}}$
c _v	Specific heat at constant volume, $\frac{\text{Btu}}{\text{lb}_m\text{-}^\circ\text{R}}$
D	Total pressure distortion
f	Frequency, cps
g	Dimensional constant, $32.174 \frac{\text{lb}_m \text{ ft}}{\text{lb}_f \text{ sec}^2}$

J	Mechanical equivalent of heat, 778.3 ft-lbf/Btu
M	Mach number
P	Total pressure, psia
P ₂₋₃₋₁	Example of individual pressure nomenclature meaning station 2, rake number 3, and probe number 1
PSD	Power spectral density function, $\frac{(\text{amplitude})^2}{\text{cps}}$
p	Static pressure, psia
R	Gas constant for air, 53.34 ft-lbf/lb _m °R
Re _D	Reynolds number based on the venturi inlet diameter
Re _I	Reynolds number index
RF	Thermocouple impact-recovery factor
R _{PL}	Radius of venturi plug (centerbody) at the airflow measuring plane, in.
R(τ)	Auto-correlation function, (amplitude) ²
T	Total temperature, °R
W	Weight flow, lb _m /sec
x	Centerbody immersion depth into the venturi, in.
α	Thermal coefficient of expansion, in./in. -°R
γ	Ratio of specific heats
Δ	Change
ΔP _{Δf}	Average value of peak-to-peak amplitude of the turbulent pressure waveform within the frequency band Δf, psid
$\left(\frac{\Delta P}{P}\right)_{\Delta f}$	Normalized turbulent pressure amplitude within the bandwidth, Δf
δ	Ratio of absolute total pressure to absolute pressure of ARDC model atmosphere at sea level (14.7 psia)
θ	Ratio of absolute total temperature to absolute temperature of ARDC model atmosphere at sea level (518.7°R)
μ	Viscosity, $\frac{\text{lb}_f\text{-sec}}{\text{ft}^2}$

τ	Lag time, msec
ϕ	Ratio of absolute viscosity to absolute viscosity of ARDC model atmosphere at sea level

SUBSCRIPTS

00, 0,	
1s, 1n,	Instrumentation stations
etc.	
a	Air
ad	Adiabatic
an	Venturi annulus
avg	Average
c	Corrected
d	Venturi wall location, downstream of venturi plane of minimum diameter
eff	Effective
eq	Equivalent (value converted to value that would be obtained using $\gamma = 1.4$ and measured areas at 540°R)
i	Indicated
max	Maximum
min	Minimum
PL	Plug (venturi centerbody)
p	Percent
u	Venturi wall location, upstream of venturi plane of minimum diameter
v	Venturi
VPS	Venturi plug (centerbody) support shaft (guide tube)
w	Wall
x	An arbitrary longitudinal location along the venturi wall
x	Venturi centerbody immersion depth into venturi
Δf	Frequency bandwidth of amplitude consideration, cps

SECTION I INTRODUCTION

Compatibility testing of a YJ93-GE-3 turbojet engine with a 0.577-scale model of the North American (NAA) XB-70 aircraft inlet duct was performed in the supersonic wind tunnel of the Propulsion Wind Tunnel Facility at AEDC. During testing at supersonic duct inlet Mach numbers with certain inlet duct bypass door configurations, unexpected engine compressor stalls occurred. The bypass door configurations, with which the stalls were associated, corresponded to normal shock-wave positions well downstream of the duct throat and near the engine compressor inlet. Limited transient pressure instrumentation at the front face of the engine indicated that high levels of pressure fluxuation existed at the time of the stalls. It is believed that this turbulent flow condition was produced by the normal shock system and was responsible for the engine compressor stalls.

To study in detail the effects of turbulent flow on YJ93 turbojet engine operation, a two-part investigation was initiated. The first portion was to develop apparatus and techniques whereby turbulent flow of known level and spectrum might be generated at the front face of a turbojet engine. The second phase of the program will be to subject a turbojet engine to the known turbulent flow conditions and to study the effects.

This report covers the first phase of the turbulence study, which was performed in Propulsion Engine Test Cell (J-1). The basic turbulence generation device was an airflow metering venturi with a variable position aerodynamic centerbody, which allowed the throat area and flow geometry of the device to be varied. This variance in geometry along with changes in flow properties produced shock-wave systems of differing severity. The shock system, in turn, was the turbulence producing mechanism.

A straight pipe engine airflow simulator equipped with a conic nozzle for airflow measurement was used to provide simulation of a turbojet engine compressor inlet at the exit of the turbulence generator.

The specific requirements of this investigation were to:

- (1) Determine the turbulence and pressure distortion producing characteristics of the turbulence generating device and determine if modifications are necessary to obtain sufficiently high turbulence levels so that meaningful testing of a YJ93 engine may be accomplished.

- (2) Obtain detailed information on the turbulent flow field produced such as its frequency spectrum, correlation from point to point at the inlet, attenuation from the generator to the simulator inlet, and in general any information pertaining to the flow phenomenon which might aid in gaining insight into the inlet turbulent flow problem as it affects engine operation.
- (3) Determine a flow coefficient for the venturi-centerbody combination.
- (4) Demonstrate the structural integrity of the turbulence generating mechanism and of the instrumentation at the front face of the simulator under turbulent flow conditions.
- (5) Develop instrumentation sensor configurations so that the turbulent flow condition at the simulator and engine inlets may be properly defined.

SECTION II APPARATUS

2.1 TEST ARTICLE

The test article consists of a YJ93 turbojet airflow simulator and a remotely positionable aerodynamic centerbody located in the primary airflow measuring venturi as shown in Fig. 1.

2.1.1 Turbulence Generator

The centerbody and the venturi (Fig. 2a) serve as a turbulence generator. Figures 2b and c give details of the variance of throat area with immersion depth and of centerbody and venturi geometry, respectively. Figures 2d and e are photographs of the centerbody.

The centerbody is supported in the venturi by a 6-in. -diam guide tube extending from the plenum chamber to the exit of the venturi (Fig. 2a). A support assembly (Fig. 3a) attached to the plenum bulkhead provides a rigid brace for positioning the forward end of the guide tube; the aft end is supported by a four-leg spider support at the exit of the venturi (Fig. 3b).

The centerbody is actuated by an inverted 10-ton capacity screw-jack driven by an electric motor (Figs. 2a and 3a). The motor is mounted outside the plenum chamber and actuates the screw-jack gear box by a drive shaft terminated at both ends by universal joints. The

screw-jack shaft is contained within the guide tube and is attached to a screw-drive dog which bolts to the forward collar of the centerbody. A slot in the top of the guide tube allows motion of the dog and centerbody along the guide tube. Centerbody travel is limited at both ends by limit switches.

2.1.2 Simulator

The YJ93 airflow simulator (Fig. 4a) consists of a YJ93 engine front frame (without the inlet guide vanes), several sections of straight pipe (which approximate YJ93 engine length and diameter), and a fixed conic nozzle. The front frame provides a mounting point for a special long bulletnose and slip ring lead-out tube (Fig. 4b), which will be used during the second portion of the turbulence investigation to lead out compressor rotor instrumentation signals. An 11-deg half-angle transition section with an exit area of 1117 in.² joined the conic nozzle to the straight pipe section of the simulator. Two previously calibrated conic nozzles were used, one with an exit area of 777.7 in.² and another with a 549.8 in.² exit area.

2.1.3 Flow Straightening Screens

Several different screen configurations (Figs. 5a through d) were installed on screen retaining grids between the turbulence generator and the simulator for use as distortion reducing and turbulence controlling devices and in one case as a vortex generator. Table I is a list of the principal configurations used during testing and identifies each screen arrangement by a configuration number.

2.2 INSTALLATION

The simulator and venturi were installed in the Propulsion Engine Test Cell (J-1) (Figs. 4a and 6 and Ref. 1) with a duct and expansion joint between them. The front of the venturi was suspended inside a labyrinth seal attached to the rear face of the plenum chamber bulkhead. The ducting between the venturi and the simulator contained the various flow straightening screens. The venturi and engine were supported by a flexure-pivot thrust stand, which was locked down during testing since thrust measurement was not a requirement.

2.3 INSTRUMENTATION

Pressure, temperature, and vibration data for airflow, pressure distortion, and turbulence determination were measured in the planes

shown in Fig. 7a. Normal shock-wave position data in the form of wall static pressure were measured at the locations shown in Fig. 7b. Details of each instrumented station are shown in Fig. 8.

2.3.1 High Response Pressure

Time varying pressure information in the frequency range from 5 to 600 cps was sensed using strain-gage-type transducers connected to total head probes (ten tubes with a length of 27 in. and one with a length of 2.68 in.). The probes with the 27-in. tube length were installed in rakes 1 and 9 (Fig. 8e), and the 2.68-in. tube length was installed in rake 10. The electrical outputs of the transducers were recorded by a magnetic tape system. All parameters recorded on magnetic tape during this test utilized the frequency modulation mode and were recorded at a tape speed of 60 in./sec. The output of one of the ten 27-in. tube connected transducers was recorded on a direct-writing recorder.

Pressure fluctuations in the frequency range from 10 to 2500 cps were recorded from two total head probes of approximately 0.6-in. tube length (Fig. 8e, rakes 2 and 14) and one flush wall static sensor (Fig. 8e, rake 13). The transducers were piezoelectric and variable capacitance, respectively, and the outputs were recorded on magnetic tape.

All high response pressure waveforms were displayed in the control room during testing on a multiple oscilloscope monitor panel system.

Frequency response characteristics of the high response pressure instrumentation are discussed in Appendix I.

2.3.2 Vibration

Vibration measurements in the form of instantaneous velocity were made by sensors consisting of a coil suspended around a permanent magnet core rigidly mounted to the simulator front frame (Fig. 8e). The sensor output was recorded by a magnetic tape system. The vibration data were used primarily to correct dynamic pressure data as discussed in Appendix I.

2.3.3 Steady-State Pressure

Total and static aerodynamic pressures were measured using absolute- or differential-type, strain-gage transducers. The differential

transducers were referenced to either floating references (established by the average of the output of three transducers redundantly measuring the reference pressure value) or to atmospheric pressure.

Steady-state pressure measurements were made at the plenum chamber, along the venturi wall, at the simulator inlet, at the conic nozzle inlet, and at the lip of the conic nozzle at the locations shown in Figs. 8a through c. The floating reference points (where applicable) were also indicated in Fig. 8.

The electrical output of the steady-state pressure transducers was scanned, digitized, and stored by a commutated analog-to-digital converter and high-speed paper tape punch system. The stored data were converted to engineering units and tabulated by a digital computer. Redundant recording of selected pressures was made with an analog direct-writing recorder.

2.3.4 Temperature

Aerodynamic temperatures at the simulator inlet and wall temperature at the exit of the conic nozzle were measured with Chromel®-Alumel® thermocouples. Iron constantan thermocouples were used to measure cell ambient temperature, venturi centerbody guide tube, and venturi wall temperatures.

All thermocouples were referenced to a 150°F (precision $\pm 0.5^\circ\text{F}$) junction. The electrical output of each thermocouple was processed in the same manner as the steady-state pressure transducer outputs.

2.3.5 Position

Venturi centerbody position was sensed by a null-balance potentiometer system using two ten-turn potentiometers. One potentiometer was chain-driven by the centerbody actuating mechanism; the other was driven by a vernier dial installed in the control room. A galvanometer indicated when the two potentiometers were at the same position.

The centerbody position was redundantly recorded on a direct-writing recorder and on magnetic tape.

2.3.6 Calibration

Both high response and steady-state strain-gage-type pressure transducers were laboratory-calibrated using a secondary standard prior to installation. Calibration information on the piezoelectric and

variable capacitance pressure transducers and vibration sensors was provided by the test user.

The magnetic tape and steady-state recording systems used with strain-gage-type transducers were calibrated by shunting precision resistors across one leg of the transducer bridge. The magnetic tape system recording data from the piezoelectric and variable capacitance pressure sensors and the vibration sensors was calibrated by the insertion of an electrical signal of known voltage. The steady-state system recording temperature data was calibrated by the insertion of a known voltage in series with the thermocouples. A calibration relating the venturi centerbody position to the control room vernier dial was established by moving the centerbody to its extreme positions and noting the vernier dial readings. The direct-writing recorder and magnetic tape systems were calibrated simultaneously with the control room vernier dial system.

All calibrations of recording systems were made both prior to and after each test period.

SECTION III PROCEDURE

Conditioned air at several different density levels was supplied to the inlet of the simulator by setting different values of simulator inlet total pressure and temperature. The principal total pressure and temperature levels of interest were 5, 10, 15, and 20 psia and 540 and 1083°R, respectively. The total pressure at the simulator inlet was set by adjusting the venturi inlet (plenum chamber) pressure to compensate for the total pressure loss across the turbulence generator shock system and screens. Venturi inlet pressure was increased as turbulence generator throat area was decreased to hold the total pressure at the simulator inlet to a desired level. Setting the total pressure and temperature at the simulator inlet determined actual airflow through the system. Simulator corrected airflow was set by either choking the simulator conic nozzle or by adjusting nozzle pressure ratio in the nozzle unchoked case.

Different levels of turbulence and pressure distortion were obtained by varying the turbulence generator throat area, thereby varying the shock-wave structure at several different values of simulator corrected airflow and venturi inlet Reynolds number (Appendix I). Further variance of turbulence and distortion was obtained by operation with different screen configurations between the venturi exit and the simulator inlet.

Venturi flow coefficient information was obtained by choking the simulator nozzle and measuring airflow at the conic nozzle exit, at the simulator inlet, and at the venturi throat planes. Flow coefficient data were obtained over the range of desired operation by moving the centerbody by distinct increments between the zero and fully-immersed positions. This procedure was performed with various screen configurations and two different conic nozzles.

The structural integrity of the centerbody and associated mounting and actuating components, the screen and screen support grids, and the instrumentation rakes at the simulator inlet was investigated by visual inspection both prior to and after each test period.

The methods of calculation used in the reduction of flow coefficient and pressure distortion data are presented in Appendix I. Statistical data reduction methods were applied to the time varying pressure data to yield power spectral density, auto-correlation, and statistical amplitude distribution properties for several representative data conditions by the methods described in Appendix I and Ref. 2. The tabulated data obtained during this investigation and plots of the power spectral density function for a portion of the time varying pressure data are included in a data package which is available upon request from AEDC Headquarters. An index of the tabulated data in this package is shown in Table II. Table III presents a listing of the parameters tabulated.

In addition to the determination of the functions given above, time-varying pressure data were reduced by the playback of waveforms from magnetic tape to oscillograph. Various bandwidths of electronic filters were used to eliminate electrical and mechanical noise from the data.

SECTION IV

RESULTS AND DISCUSSION

The objectives of this investigation were to (1) determine the turbulence and distortion producing characteristics of the turbulence generator and what, if any, modifications must be made so that meaningful testing of a YJ93 turbojet engine may be accomplished, (2) obtain detailed information on the turbulent flow fields produced so that the effects of turbulent flow on turbojet engine performance may be better understood, (3) determine an airflow coefficient for the turbulence generator, and (4) demonstrate the structural integrity of the turbulence generating apparatus and of the instrumentation at the simulator inlet under turbulent flow conditions.

The results obtained in this investigation are discussed below in terms of the basic turbulence waveform and type of distortion produced and their dependence on different flow parameters and screen configurations. Calibration data for the turbulence and distortion produced by each of the different configurations tested are also discussed. A discussion of the airflow calibration results and the structural integrity of the apparatus follows the turbulence and distortion calibration.

4.1 BASIC TURBULENCE AND DISTORTION DEFINITIONS AND ANALYSES

The output of the turbulence generator must be considered both in terms of distortion and turbulence. For the purposes of this discussion, the following definitions of these two parameters will apply.

4.1.1 Definitions and Terminology

Turbulence is the variation with time of pressure (either total or static, but more commonly total) in a pulsating manner about some mean or steady-state pressure level. Quantitatively, turbulence is expressed as the ratio of the average value of the peak-to-peak fluctuation about the mean to the mean value itself. The result is termed "normalized turbulent pressure amplitude," the normalizer being the steady-state pressure level value. Figure 9a is a graphical presentation of turbulence, and more detailed information on the measurement and calculations of turbulence is contained in Appendix I.

Distortion is the variation of pressure (either total or static but more commonly total) with geometric location in the plane of the simulator inlet. In quantitative terms, distortion is expressed as the ratio of the difference between the maximum and minimum values at any point in the field divided by the overall average value of the pressure in that plane (see Appendix I). Although no regard is given to the location of the maximum and minimum pressures in the field in calculating distortion, by convention, high pressure at the center of the flow field is termed positive and the opposite case is termed negative. The situation of high pressure at the center (positive case) is sometimes referred to as "tip radial distortion," and the high pressure at the outer edge is called "hub radial distortion." (This nomenclature may be pictured by considering the span-wise sense of flow direction along a compressor blade caused by a pressure potential provided by the distortion in the flow field.)

The sign convention given above describes only the geometric variance of pressure in the radial direction. In addition to this, pressure

may vary circumferentially. No sign convention is used to indicate this; however, certain nomenclature is used to describe circumferential distortion. A circumferential distortion pattern with one depressed pressure region is termed a "one/rev" pattern. In a like manner, two depressed pressure regions would be called a "two/rev" pattern. This set of nomenclature is derived from the number of impulses a compressor blade would feel in the course of one revolution through a circumferentially distorted flow field caused by the flow distortion itself.

Figure 9b is an illustration of both radial and circumferential distortion presented in rectangular coordinates. Figure 9c combines both radial and circumferential distortion into a polar graph with lines of constant normalized pressure. Again, the steady-state pressure, averaged over the plane of the simulator inlet, serves as the normalizer.

4.1.2 Turbulence Waveform and Statistical Analysis

To permit evaluation of the effect on YJ93 engine performance under turbulent inflow conditions, it is important that the type of dynamic disturbance entering the compressor be known. The engine for example might be quite tolerant of disturbances in one frequency range, whereas it might be quite intolerant to disturbances in another range. Waveform and statistical analyses were performed on the turbulent pressure data so that this end might be accomplished.

Figures 10a through d are waveforms of turbulent pressure, taken at different flow conditions and with two different screen configurations between the turbulence generator and the simulator inlet. It may be observed from the waveforms that they are either random or aperiodic complex waves. It may also be observed that little difference is found among the four different traces.

Evaluation of the power spectral density function for these waveforms yields additional information on their nature. Figures 11a and b are typical frequency distributions of turbulent total pressure recorded during this investigation.¹ In keeping with the terminology previously

¹The spectral analyses presented in this report are based on a frequency range from 0 to 200 cps for several different reasons. First, it is believed that this frequency range contains the bulk of the activity which will affect turbojet engine operation; secondly, instrumentation limitations (nonlinear frequency response characteristics discussed in

defined, the power spectral density function (Appendix I and Ref. 2) will be termed the "normalized turbulent pressure spectral density" in this report.

Figure 11a depicts a sloping distribution of the turbulent pressure with frequency. Figure 11b shows a uniform or "white" distribution. With a few exceptions (to be discussed in more detail later), all outputs of the turbulence generator fall somewhere between these two extremes. The important thing to note about these two distributions is that they are both predominately random. To further investigate the nature of the waveform the auto-correlation function was estimated. Figures 12a and b are the auto-correlation functions for the sloping and the uniform distributions, respectively. The strong self-dependence (maximum amplitude at zero lag time) of both cases indicates that the waves are predominately random; the small fluctuation about the zero level for τ greater than 5 msec indicates a small degree of periodic content present in the wave. (See Appendix I and Ref. 2 for a discussion of the auto-correlation function.)

Consideration of the skewness and kurtosis functions (Appendix I) of the amplitude distribution parameters along with the auto-correlation function indicates that the distribution of the turbulent pressure is near Gaussian if the periodic wave content is small.

Data discussed in Ref. 3 show that instantaneous velocity measurements made in a turbulent flow field behind a grid were found to have a similar frequency distribution (the power spectral density functions were similarly shaped). In the same reference, the amplitude distribution of turbulent velocity correlation functions was found to be near Gaussian also.

Appendix I) make reduction of spectral data extremely laborious; and third, correction for these instrumentation limitations indicates that a liner extrapolation of the mean level of the spectra at the slope of the spectra which exist between 100 and 200 cps is a good approximation of the data recorded up to 600 cps, thereby providing a method of determining the spectra in the higher frequency range if such information is required.

Turbulent pressure amplitude information for the frequency bands of 0 to 50, 0 to 200, 0 to 600, and 0 to 2000 cps is presented in this report to show in detail the relative importance of the different frequency ranges as they relate to other parameters. Amplitude data were corrected for nonlinear frequency response of instrumentation units using an approximation technique given in Appendix I which is easily applied to the data.

Repeated measurement of the mean square amplitude of the wave at different points in time revealed essentially the same values indicating that the random process is stationary.

4.1.3 Standing Wave and Periodic Wave Content

As was previously mentioned, the data waveform included varying degrees of periodic content. This periodic content can result from several different sources. Acoustical resonances (tube or Helmholtz or standing waves between the bullet nose and simulator wall) along with von Kármán vortices shed by the venturi centerbody guide tube aft support struts are possible sources. A large amount of periodic noise appeared in some of the raw data but was distinguished from true data by the techniques given in Appendix I.

A survey of the data recorded indicated the existence of a large number of low amplitude resonance spikes in the spectrum. Some of the spikes seemed to form harmonic families. A few of the families were 30, 60, 90 cps; 10, 20, 40, 80 cps; and 50, 100, 150, 200 cps. Repeatable individual spikes appeared at 5 to 10 cps, 15 cps, and at 110 cps. The complexity of the turbulence generator and simulator geometry prevented reliable matching of these observed components to acoustical modes which might have been excited within the system. Approximate calculation, however, shows that the longitudinal resonance of the simulator pipe should occur with its fundamental near 30 cps. This indicates that the 30-, 60-, 90-cps family is possibly caused by this mode.

The largest repeatable spike appeared in the vicinity of 5 to 10 cps and occasionally doubled the amplitude level as compared to the random background level upon which it is superimposed. All other resonance points are of even less relative magnitude. The relative magnitude of the spikes diminished as the Reynolds number at the inlet to the venturi increased.

The important observation to be made concerning the periodics is that they are generally small compared to the random content of the wave, or stated otherwise, there were no extremely high concentrations of energy in the frequency spectra investigated.

4.1.4 Pressure Distortion at the Simulator Inlet

Inspection of static and total pressure profiles indicated that a large degree of total pressure distortion existed (depending on flow conditions and turbulence generator geometry), whereas little distortion of static pressure occurred. In one case, total pressure distortion was 52 percent, whereas static pressure distortion was only 3.1 percent. The

indication of this situation is that the distortion in total pressure essentially represents a distorted velocity field.

Distortion patterns in both the radial and circumferential modes were encountered during testing. More detailed discussion of specific total pressure distortion patterns is given in Section 4.3. The relationship between turbulence and distortion is discussed in Sections 4.1.5 and 4.2.5.

4.1.5 Distribution of Turbulence over the Plane of the Simulator Inlet

Figure 13 shows waveforms of turbulent pressure taken at several different immersion depths in the airstream. Inspection of these waveforms indicates that correlation exists among them. Lag or lead times from wave to wave were estimated by noting the occurrence of significant pulsations which appeared in all waves (pulsation A in Fig. 13, for example) and measuring the time difference among them referred to a point at 0.86-in. immersion depth into the stream. Figure 14 presents the results of measurements of lag or lead times for two different cases. The measured values are the average of five separate pulsations for each point shown. As might be expected, a good deal of scatter was present in the results, but the average points are indicative of the trends of lag or lead times individually measured.

Figure 14b shows the relative amplitude distribution in the field for two cases of distortion under consideration. Distortion is seen to affect the amplitude characteristics as well as the time characteristics.

Figures 14a and b establish representative transmissibility of turbulence in the plane of the simulator inlet. It is seen that the characteristics are governed by distortion. Amplitude distributions for the different geometric configurations tested are given in detail in Section 4.3.

4.2 DEPENDENCE OF TURBULENCE ON FLOW PARAMETERS AND SCREEN CONFIGURATIONS

The change of turbulence with flow parameters is important for several different reasons. Primarily, the flow conditions at the inlet to the engine will be the same as those experienced during this investigation, and for any given screen configuration, the flow parameters will determine the turbulent flow conditions which will exist at the engine inlet. Secondly, similarity of the flow from the turbulence generator and aircraft inlet duct can be described only in terms of flow parameters since the geometries are quite different. Third, the basic mechanism of

turbulence generation, the normal shock system, should be related to the flow conditions which exist in the turbulence generator and these relations noted.

The variance of turbulence with other parameters will be discussed in terms of normalized amplitude and spectral density. Turbulence was found to vary as a function of corrected airflow, venturi annulus area, venturi inlet Reynolds number, simulator inlet total pressure distortion, and screen configuration between the venturi exit and the simulator inlet.

4.2.1 Corrected Airflow

Figure 15 shows the change in amplitude as a function of corrected airflow for several different values of venturi annulus area and for the situation of no screens between the venturi exit and the simulator inlet. At a fixed value of annulus area, the amplitude is seen to increase to a maximum somewhere in the vicinity of 160 lb/sec and then decrease again. Following the decrease, an increase again occurs, but the lack of data between 180 and 260 lb/sec prevents definition of the manner in which the second increase takes place. This behavior suggests that a transition in the mode of flow takes place within the turbulence generator as corrected airflow increases.

Changing corrected airflow causes changes in the normal shock parameters, shock inlet Mach number, static pressure rise, total pressure loss, and the structure of the shock system in general. Figure 16 shows the distribution of wall static to inlet total pressure along the venturi wall for several different values of corrected airflow. The annulus area is 110 in.² for this particular case. As would be expected, essentially the same flow acceleration curves are formed. Observation of the deceleration curves for the different corrected airflow values show, however, quite a variation in pattern. Relatively narrow, normal shock patterns followed by gradual subsonic diffusion are indicated for the 140 and 160 lb/sec corrected airflow cases. These two cases correspond to the first region of increasing turbulence amplitude with increasing corrected airflow shown in Fig. 15. The pressure ratio patterns indicated for the 180 and 260 lb/sec cases show a series of decelerations and accelerations. This pattern is strongly indicative of an extended lamda-type shock system. Figure 17 is a sketch of the shock systems corresponding to the two different airflow regimes made from the pressure ratio distribution of Fig. 16 and Schlieren photographs of somewhat similar flow geometry and pressure ratio distribution situations found in Ref. 4. Criteria for the formation of the branched or lamda shock systems in diffuser flow are discussed in Ref. 5.

The effect of these two different modes of flow on the production of turbulence from Figs. 15 and 17 seems to indicate that the narrow shock systems are more efficient in the production and transmission of turbulence to a point downstream of the shock system. A possible explanation of this behavior is that the turbulent energy produced by the initial shock wave is dissipated in mixing with the turbulence produced by the downstream members of the system. It may be noted, however, that turbulence production in both modes increases with increasing corrected airflow. This may be explained by the fact that in both modes (1) increasing corrected airflow increases the energy input at the shock systems for the production of turbulence and (2) increasing corrected airflow translates the shock system further downstream to a point nearer the turbulence measuring station, therefore decreasing the viscous damping which occurs between the points of turbulence production and measurement.

Although the above analysis was made based on a value of annulus area of 110 in.² and with no screens installed at the exit of the venturi, the results are qualitatively representative of all the configurations investigated. Further discussion of the effects of throat area and screen blockage will be covered in Sections 4.2.2 and 4.2.5.

Figure 18 shows the normalized turbulent pressure density spectra for several different values of corrected airflow. Little significant change other than in general level which was discussed above in terms of amplitude is seen to exist.

4.2.2 Venturi Annulus Area

The change in turbulence production with annulus area ranged from a situation of extremely little change to the case of a strong increase with decreasing annulus area. The magnitude of the increase depended on the corrected airflow setting and screen configuration being investigated. Specific curves of turbulent amplitude versus venturi annulus area for the different screen configurations are discussed in Section 4.3.

In general, changes in the normalized turbulent pressure spectral density with annulus area were only in level and not in distribution shape.

4.2.3 Venturi Inlet Reynolds Number

The effects on turbulence of changes in pressure and temperature at the inlet to the venturi were combined by considering the effects of Reynolds number changes at that station. Venturi inlet Reynolds number (Appendix I) was calculated using the diameter of the venturi inlet

as the characteristic length. Figures 19a, b, and c show the variance in the normalized turbulent pressure amplitude for values of venturi annulus area of 110, 245, and 410 in.², respectively. Curves for corrected airflow values of 145 and 260 lb/sec are given. Above a value of Reynolds number of 0.5×10^8 , little change in amplitude with Reynolds number is seen for any of the area values. For all but the case of the 110 in.² setting, this statement may be made over the entire range of venturi inlet Reynolds numbers tested.

Some of the scatter in the region below Reynolds number values of 1.0×10^8 in Figs. 17b and c was caused by slight deviations in airflow setting from the nominal value of 145 lb/sec. (This airflow value is in the region of large sensitivity of turbulence to corrected airflow.)

Essentially the same trend of variance of amplitude with Reynolds number exists whether the amplitude content of the 0- to 50-cps bandwidth or the 0- to 600-cps bandwidth is considered. As can be noted from Fig. 19, as the venturi annulus area becomes smaller, the effect of Reynolds number is more pronounced. This should be expected since the viscous flow region (boundary layer) becomes a greater percentage of the total physical area as physical annulus area decreases and, therefore, exerts more influence on the overall flow field.

Figures 20a and b show the effect of venturi inlet Reynolds number on the normalized turbulent pressure spectral density for corrected airflow values of 145 and 260 lb/sec, respectively. As the Reynolds number is increased, the turbulent total pressure distribution with frequency tends to become uniform. The Reynolds number is representative of the relative importance of inertia and viscous forces present in the stream. The damping of the turbulence is dependent on viscosity and the propagation dependent on inertia; therefore, the change in spectral distribution with Reynolds number can, at least in part, be explained by the amount of viscous damping which occurs in the transmission of the turbulence to the measurement plane from the point of generation. At relatively low Reynolds numbers, the viscous forces will be greater (as compared to the inertial forces) than they would be at a higher value of Reynolds number. Stated differently, viscous damping of turbulence will be greater as the Reynolds number is decreased. The actual attenuation of turbulence because of viscous damping is dependent on both viscosity and particle velocity; therefore, the viscous damping would be more pronounced at higher frequencies (corresponding to higher particle velocity). From Fig. 20, it may be seen that this explanation of the curve shape fits very well. Similar distribution curves and verification of attenuation of higher frequency components are contained in Ref. 3.

The observations given above on the effect of Reynolds number are qualitatively true for all of the configurations tested (see Section 4.3).

4.2.4 Simulator Inlet Total Pressure Distortion

Distortion of the steady-state total pressure and turbulence amplitude are closely related. The general variance of turbulence with physical parameters essentially describes the variance of distortion with the same parameters. Generally, high values of distortion accompanied high values of turbulence, and low with low.

Although no complete theoretical explanations have been made which describe the relationship of turbulence and distortion, several working theories which relate steady-state velocity profiles with turbulence amplitude have been forwarded. Prandtl's mixing length theory and von Kármán's similarity hypothesis are two such theories which have been found to be in good agreement with experimental data (see Ref. 6).

4.2.5 Screen Configuration

The effect of inserting screens between the venturi exit and the simulator inlet is manifest in several different ways.

First, the addition of blockage at the venturi exit causes an additional pressure drop to exist and allows the normal shock system in the venturi to be less severe. (The shock system moves further upstream.) This will cause less turbulence to be produced at the shock wave (unless the additional blockage of the screens causes a transition from the lamda to the narrow shock system flow regimes, in which case the turbulence production at the shock could increase).

Secondly, the screens themselves act as attenuators of turbulence. They dissipate energy viscously as the turbulent flow passes through them. In this manner, the transmission of turbulence is affected.

Third, air flowing over the screen wire (or edges) causes vortex shedding, the frequency of which is proportional to the diameter of the wire (or width of the concentric rings in the case of the vortex generator configuration). This action, therefore, creates turbulence. Because of the physical dimension of the screen wires, the frequency of shedding is very high, and as a result, this energy is dissipated very rapidly. (The vortices which originate as high frequency periodics will degenerate because of mixing in the stream to a random frequency distribution; see Ref. 3.)

The net result of the above three effects was found generally to be a reduction in turbulence at the simulator inlet.

Inlet total pressure distortion was also affected by the screens. The shape and size of screens were the great influencing factors in this case.

4.3 TURBULENCE AND DISTORTION CALIBRATION

Specific performance information for each of the configurations tested is required so that known levels of turbulence and distortion may be introduced to the inlet of a YJ93 turbojet engine during the second phase of this study.

Calibration information and peculiarities of each of the configurations tested are given in Sections 4.3.1 through 4.3.6 in terms of turbulence amplitude, spectra, and distribution over the simulator inlet plane. Also included is distortion magnitude and distribution information for each of the configurations tested.

4.3.1 Open Configuration – Low Corrected Airflow Case

Figures 21a through d depict the variance of several different forms of the normalized turbulent pressure amplitude for the case of no screens at a nominal corrected airflow value of 145 lb/sec. Turbulence amplitude is seen to form a single curve for the different steady-state pressure levels except at the 5.0-psia levels where the Reynolds number effect (Section 4.2.3) is evident (Figs. 21a and b). The difference between the high temperature and low temperature cases is exaggerated by the fact that the corrected airflow setting during the high temperature test was somewhat lower (approximately 138 lb/sec) than the nominal 145 lb/sec (see Section 4.2.1). The solid curves shown in Fig. 21a and b represent the average value of the pressure probes which cross the simulator inlet at angles of 22.5 and 202.5 deg (see Fig. 8, rakes 1 and 9).

The dashed curves in Figs. 21a and b present the maximum and minimum values of turbulence amplitude experienced along rakes 1 and 9 and indicate the degree of variance which exists in turbulence amplitude from point to point in the field as a function of venturi annulus area. It is seen that in both the 0- to 50- and the 0- to 600-cps bandwidth cases that the spread increases with decreasing annulus area.

Turbulence amplitude in the 0- to 200-cps bandwidth at a point near the simulator wall (0.86-in. immersion depth) is shown in Fig. 21c and

indicates a slight increase in amplitude with decreasing venturi annulus area. Similar variance of the estimated wall static pressure (Appendix I), based on a bandwidth of 0 to 2000 cps, is seen in Fig. 21d.

Profiles of the ratio of turbulence amplitude to the average value of turbulence are shown in Figs. 22a, b, and c for annulus area values of 410, 246, and 110 in.², respectively. Only a slight increase in slope and spread is shown in decreasing annulus area from 410 to 246 in.². A marked increase in the spread occurs between the 246 and the 110 in.² area settings.

Figures 23a, b, and c show the normalized turbulent pressure spectral density for several different pressure levels with annulus area values of 410, 246, and 110 in.². The spectra is smoothed to ignore any fluctuation less than 10 cps in width so that the basic frequency distributions occurring for several different pressure levels may be compared. Section 4.1.1 defines the normalized turbulent pressure spectral density. Inspection of the figure shows that little change in the shape of the frequency distribution is experienced in decreasing the annulus area and that, in general, the distributions are of the sloping type. For this configuration, venturi inlet Reynolds number values were generally below that required to produce the uniform spectrum discussed in Section 4.2.3.

The distortion producing characteristics of this configuration are given in Fig. 24. Figure 24a shows that a steady increase in distortion takes place as the annulus area is decreased. The results are valid for both values of inlet temperature under consideration. Figures 24b, c, and d are representative polar plots showing the normalized pressure distribution over the simulator inlet. The plots were obtained by cross-plotting radial and circumferential pressure profiles, assuming linear variance from probe and probe. The distortion patterns indicate a slight circumferential pattern which seems to rotate slightly and become strong as annulus area is decreased. The patterns are circumferentially of a one/rev type and radially of a tip radial nature. The patterns shown were taken with a value of total temperature at the simulator inlet of 1083°R. The patterns at the lower value of temperature were similar in shape, but generally slightly less severe.

4.3.2 Open Configuration – High Corrected Airflow Case

The variance of the averaged values of turbulence amplitude with venturi annulus area is shown in Figs. 25a and b. Maximum and minimum values are indicated by the dashed lines. Data are shown for two different aft venturi centerbody guide tube support positions (see

Section 2.1.1 and Fig. 3b). In the case of the slip ring leadout strut at 0 deg, the guide tube supports are positioned such that the rakes sensing turbulence are in the wake of the guide tube supports and do not truly represent turbulence amplitude in the free stream. The single probe data shown in Fig. 25c may be affected by the support position also.¹

Generally, turbulent total pressure increased with decreasing annulus area and the estimated wall static pressure (Fig. 25d) decreased.

Figure 26 shows typical profiles of turbulence amplitude in the stream for this configuration. In all cases the higher values occurred near the bulletnose.

Representative spectra are shown in Fig. 27. Two different distribution shapes are seen to occur for this configuration. Both the sloping and uniform distributions are present. The uniform spectra occurs for pressure levels at the simulator inlet of 15 and 20 psia which correspond to high venturi inlet Reynolds numbers.

Figure 28a shows that distortion becomes very large as venturi annulus area decreases. A maximum value of 52 percent occurs at an annulus area of 110 in.².

Contours of constant pressure are shown in Figs. 28b through e. All profiles are essentially of a tip radial, one/rev nature (although some additional minor circumferential depressions do exist). Figures 28c and d show the effect of changing the orientation of the center-body guide tube aft support assembly.

4.3.3 Light Screen Blockage Configuration

A slight increase of the averaged turbulent amplitude is seen to occur with decreasing annulus area in Figs. 29a and b. The spread between the maximum and minimum values in the field also increases. Little change is found in the single probe data with decreasing area as shown in Fig. 29c, whereas the wall static pressure in Fig. 29d shows an increase.

Figures 30a through c show that the turbulence near the bulletnose becomes the higher value as the smallest annulus area is obtained.

¹All other configurations tested which are included in this report were conducted with the turbulence pressure rakes exposed to the free stream.

Spectra shown in Figs. 31a, b, and c indicate the insensitivity of the frequency distribution to changes in annulus area. The uniform distribution is seen again to evolve at the higher pressure levels.

Figure 32a shows that distortion increases with decreasing annulus area to a value of 32 percent for pressure levels above 10 psia and to 43 percent for the 5-psia case. Very little variation in pressure is seen to exist in Fig. 32b which represents the distortion distribution for this configuration with an annulus area value of 410 in.². Figures 32c and d show that as the area decreases a predominately tip radial, one/rev, distortion pattern with additional smaller circumferential variation is produced.

4.3.4 Intermediate Screen Blockage Configuration

Figures 33a, b, and c show that very little variance of turbulence amplitude with annulus area occurs for the averaged cases, whereas a decrease takes place with decreasing area for the single probe. The spread between the maximum and minimum values shown in Figs. 33a and b indicates little change until the area is decreased below 150 in.².

The slope of the curve of turbulence amplitude versus immersion depth into the stream is seen in Figs. 34a through c to become steeper as annulus area decreases. The difference between the two angular locations indicates that a circumferential variance of turbulence also exists with the rake at the 22.5-deg location having the higher values.

Typical spectra shown in Figs. 35a, b, and c for this configuration indicate some variance in the shape of the curve for the 10-psia level between the 410 and 110 in.² area settings (Figs. 35a and b). This difference (along with the large relative circumferential variance in turbulence amplitude) results from a change in the mode of flow which exists in the venturi as the annulus area is decreased. Figure 36a indicates that an abrupt change in the distortion magnitude also occurs as annulus area is decreased. Inspection of venturi wall static pressure longitudinal distributions indicates that the flow is attached to the venturi wall for both modes of flow. A large change in radial distortion (from hub radial at 410 in.² to tip radial at 110 in.²) is shown in Figs. 36b, c, and d as annulus area decreases and suggests that flow separation may occur on the centerbody wall as it moves downstream. The high blockage concentrated near the center of the stream at the venturi exit is the instrument whereby back pressure causing separation could be produced (see Fig. 5b).

4.3.5 Heavy Screen Blockage Configuration

Low values and little variance of turbulence amplitude with annulus area are seen to exist for this configuration (Figs. 37a, b, and c). The spread between the maximum and minimum values increases slightly with decreasing annulus area.

Figures 38a, b, and c indicate that little variance in turbulence amplitude radial profile exist for this configuration.

Spectra shown in Figs. 39a, b, and c indicate the presence of both the sloping- and uniform-type frequency distributions. In addition to these random distributions, a harmonic family exists in some of the spectra (see Section 4.1.3).

Figure 40a shows that little distortion occurs at any setting of annulus area (generally less than 5 percent). Pressure contours shown in Figs. 40b, c, and d indicate very mild distortion at all settings of annulus area in both the radial and circumferential modes.

4.3.6 Vortex Generator Screen Configuration

Figures 41a through c show little variance of turbulence amplitude with annulus area for the averaged or the single probe data with this configuration. An increase in wall static pressure occurs with decreasing annulus area as shown in Fig. 41d.

Figures 42a, b, and c show that very little difference exists in the radial profiles of turbulence amplitude from area settings of 410 to 110 in.².

Typical spectra produced by the vortex generator configuration are shown in Figs. 43a, b, and c. Some periodics exist for this configuration.

Distortion varied little with annulus area as shown in Fig. 44a. Figures 44b and c indicate that the distortion pattern is predominately hub radial at annulus areas of 410 and 246 in.². Figure 44d shows that a more complex pattern (still hub radial) results with an area setting of 110 in.².

4.3.7 Miscellaneous Observations and Summary of Turbulence and Distortion Calibration Data

Comparison of amplitude levels and trends as given in terms of averaged values to single probe values indicates that single probe values

are not sufficient to describe the flow field. Averages calculated using one probe near the simulator wall and one probe near the bulletnose were found to compare well in most cases to averages based on five values along a radius from the bulletnose to the venturi wall. Since variations in turbulence with circumferential location were experienced, a more suitable arrangement of turbulent pressure probes would then be a number (possibly four or six) of two probe rakes equally positioned circumferentially.

Little difference is found in the shape of the spectra produced by the different screen configurations. This allows simulation of frequency distributions of shock-wave-induced turbulent flow at levels of turbulence amplitude and distortion different from that obtainable only with the open configuration.

The overall capabilities of the turbulence generator are shown in Figs. 45a and b. The representative points plotted indicate that values of turbulence up to 28.4 (0- to 50-cps bandwidth) and 57.0 (0- to 600-cps bandwidth) percent of the steady-state total pressure level are available from the generator. Distortion levels up to 52 percent are produced by the system. The coverage of the "turbulence-distortion map" (Fig. 45) provided by the turbulence generator is sufficient to allow meaningful testing of a YJ93 turbojet engine based on the estimations (supplied by the user) of turbulence amplitude existing in the aircraft duct.

4.4 AIRFLOW CALIBRATION

To facilitate calculation of airflow, and thereby calculation of performance parameters, in the second (engine) phase of the turbulence investigation, a flow coefficient must be determined at some point in the flow system. Flow coefficients at both the venturi annulus and at the simulator inlet were investigated for this purpose. Airflow calculated at the exit plane of the conic nozzle served as a standard for the calculation of flow coefficients. Flow coefficients were calculated as described in Appendix I.

The flow coefficient at the venturi annulus was found to vary primarily as a function of annulus area, venturi inlet Reynolds number, and the configuration of the flow straightening screens installed at the exit of the venturi. Variance of flow coefficient at any given venturi annulus area setting with static-to-total pressure ratio at the plane of airflow measurement was negligible because, over the airflow range of interest, the system was choked.

4.4.1 Effect of Varying Centerbody Immersion Depth

To properly understand the variance of flow coefficient and static-to-total annulus pressure ratio with area, the behavior of annulus area with centerbody immersion depth must be understood. Figures 46a, b, and c are schematics of the flow passage of the venturi-centerbody combination and show the plane of airflow measurement for annulus area settings of 410, 246, and 110 in.². The minimum cross-section area of the system exists at a point five inches upstream of the minimum venturi diameter for centerbody immersion depths less than 87 percent of full travel (30.6 in.) and at various locations between the 5-in. upstream plane and the minimum venturi diameter for the last 13 percent (5.4 in.) of centerbody travel. To keep the plane of airflow measurement at a near critical flow position over the entire range of centerbody movement, airflow is calculated at the location 5 in. upstream of the venturi minimum diameter for the first 30.6 in. of motion and then at the plane of venturi minimum area for the last 5.4 in. of travel. These cross-section areas will normally be somewhat greater than the minimum flow area, and therefore the flow coefficients will be lower than would be expected if the true minimum flow area (throat) had been used. Figure 47 shows the variance of airflow measurement plane area with centerbody immersion depth.¹

The effect of the plane area change on static-to-total pressure ratio is shown in Fig. 48. For the greater portion of the area variation, the pressure ratio is very nearly the critical pressure ratio. As the area decreases to 150 in.², the pressure ratio begins to rise indicating that the throat of the system is starting to move toward the plane of minimum venturi diameter as shown in Fig. 48; the flow is initially supersonic but rapidly moves upward through the critical value of pressure ratio to an unchoked value at the fully inserted position of the centerbody. Although the pressure ratio varies considerably as area is changed, the value of pressure ratio for any given value of area is essentially constant which allows its effect on flow coefficient to be incorporated into the variation of flow coefficient with area. Between

¹Original design of the apparatus assumed operation over only the first 87 percent of venturi centerbody travel which would have provided a very straightforward variance of area with venturi centerbody immersion depth. Testing however showed that the greater immersion depths were required so that the range of turbulence and distortion desired could be properly covered, therefore making necessary the somewhat complex behavior of the venturi airflow measurement plane described above.

200 and 370 in.² (corresponding to centerbody immersion depths of 23 and 4 in., respectively), the pressure ratio curve is very flat and takes on a value of 0.505 on the average indicating slightly supercritical operation (Mach number of 1.04). This region would then be the most favorable for use in measuring airflow for the determination of engine performance parameters. Measurement at area values of less than 160 in.² should be avoided.

4.4.2 Reynolds Number and Screen Blockage Effects

Figures 49a, b, and c show the variance of flow coefficient with venturi inlet Reynolds number for different screen configurations at venturi annulus areas of 410, 246, and 110 in.². The variation of flow coefficient with Reynolds number in general is most pronounced for Reynolds numbers below 2 to 3×10^8 . Above this point, the effect is seen to become less significant; that is, the curve becomes essentially flat above 3×10^8 . Figure 49 also shows that the slope of the curves of Reynolds number versus flow coefficient below Reynolds number values of 3×10^8 are negative for both the open and vortex generator screen configurations and positive for the light, intermediate, and heavy configurations. The main physical difference between these two groups of screen configurations is that the vortex generator and the open configurations both have very light area blockage immediately at the exit of the venturi (and at the end of the centerbody guide tube), whereas the other configurations have relatively heavy blockage at this point. The blockage of the upstream screen then seems to be the slope determining factor. (Figures 5 and 7 show screen locations and configurations, and Table I lists their major characteristics.) The fact that the screen configurations which are downstream of the plane of airflow measurement have any effect on flow coefficient (since supersonic flow exists for a portion of the distance between the two planes) suggests that feedback through the boundary layer along both the centerbody guide tube and venturi wall is the mechanism providing the effect. The change in the slope of the flow coefficient versus Reynolds number curves then would have to be a result of different manifestations of the back pressure feedback through the boundary layer.

For the case of the light, intermediate, and heavy screen configurations, venturi flow coefficient increased with increasing Reynolds number. This behavior may be explained by decreasing boundary layer displacement thickness which occurs with increasing Reynolds number. In the case of the open and vortex generator screen configurations the effect is reversed. Centrifugal effects, shifting sonic plane, or other effects that may change the effective flow area appear to be predominate in this case rather than the normal displacement thickness growth of the

boundary layer. These mainstream changes may be caused by relatively large differences in the boundary layer, which are caused by changes in screen configuration at the venturi exit.

Generally flow coefficient increased with increasing blockage at the venturi exit for any given centerbody immersion depth and Reynolds number.

4.4.3 Miscellaneous Effects on Venturi Annulus Flow Coefficient

Venturi annulus wall temperature, centerbody and support assembly elastic deformation, and airflow leakage between the centerbody and the guide tube were effects which were found to be either accountable in calculation or to have negligible effect on the venturi annulus flow coefficient.

Inaccuracies in the determination of centerbody immersion depth resulted in some scatter in the flow coefficient data. The inaccuracies resulted from mechanical slack in the centerbody driving mechanism, instrument and reading error, nonrepeatability of limit switches used to establish minimum and maximum centerbody immersion depths, and in several cases, plastic deformation of the centerbody (Section 4.5.1). Comparison of data from several different tests allowed the effect of the scatter to be diminished. The extent to which the scatter exists is shown in the combined flow coefficient curves in Fig. 50.

4.4.4 Combined Flow Coefficient Curves

Figures 50a through d are representations of venturi annulus flow coefficient and combine all effects into the variation of flow coefficient with annulus area and venturi inlet Reynolds numbers. Each individual plot is for a particular screen configuration. Figure 50c serves to describe the characteristics of both the heavy and intermediate screen configurations.

The lines of constant Reynolds number were obtained by cross-plotting flow coefficient with Reynolds number for each screen configuration at several different values of centerbody immersion depth. (Figure 49 is typical of the crossplots used to obtain these curves.) The data shown on these plots indicate the degree of scatter present.

The discontinuity in the slope of the flow coefficient curves results from the change in planes of airflow calculation previously discussed.

With knowledge of screen configuration installed, venturi inlet Reynolds number, and venturi annulus area, a flow coefficient may be

found from these curves for the calculation of engine performance parameters during the engine portion of the turbulence investigation.

4.4.5 Simulator Inlet Flow Coefficient

The flow coefficient at the inlet to the simulator varied primarily with pressure distortion. The degree to which the flow coefficient scattered depended on the Mach number at the inlet.

Figure 51a shows the effect of pressure distortion on the flow coefficient at the simulator inlet. Generally, the coefficient decreases as distortion increases. The effect is more severe as corrected airflow is decreased. The decrease in flow coefficient with distortion is caused by the manner of calculation used to determine airflow at the inlet (Appendix I). An arithmetic average of static pressure, total pressure, and total temperature is used to calculate airflow. This type of calculation is exactly correct for the case of no pressure or temperature distortion only. In practice, however, good results are obtained for values of distortion up to approximately 5.0 percent. (This may be seen from the grouping of data below 5.0-percent distortion in Fig. 51a). To further illustrate the effect of distortion on the flow coefficient calculation, values of flow coefficient for a sample condition were calculated by dividing the simulator inlet plane into segments, calculating airflow on a local basis (using local values of pressure and temperature), and then summing the airflow values of each segment. This operation was performed using five concentric circles as segments and using 80 segments (four 90-deg arcs of 20 concentric circles). The value of distortion for the condition under consideration was 52 percent. The flow coefficient based on average pressure and temperature was 0.8814; based on the five-segment calculation, it was 0.9102; and based on the 80-segment calculation, the value was increased to 0.9346. Application of segmented area techniques of calculation is then a method whereby the distortion effects may be diminished; however, a great number of pressure and temperature samples must be obtained, and the calculation procedure becomes very lengthy.

Figure 51b shows the scatter of the simulator inlet flow coefficient as a function of Mach number for different nominal values of distortion. The scatter bands decrease greatly as Mach number increases. This result is to be expected since the differential between static and total pressure increases with increasing Mach number and may then be measured with greater accuracy and repeatability. A scatter band for distortion values less than for 5.0 percent is shown in Fig. 51b and indicates a reasonably well-behaved flow coefficient at values of inlet Mach number above 0.40. At lower values of Mach number and higher values

of distortion, the scatter is so great that the airflow measurement at this location is unsuitable for calculation of engine performance parameters.

4.5 STRUCTURAL INTEGRITY

One major objective of this test was to determine if the structural integrity of the turbulence generating system was sufficient to allow safe operation with an engine installed instead of the simulator. The elements in the airstream were subjected to both static and dynamic loading.

4.5.1 Venturi Centerbody Assembly

Several structural problems occurred during testing which resulted from static loading (aerodynamic forces) on the centerbody. Cap screws which retain the centerbody to the drive mechanism and the centerbody forward collar were deformed on two different occasions. Figure 52a shows collar deformation which took place on one occasion, and Fig. 52b indicates the modifications which were made. During subsequent testing, the turbulence generator was operated successfully up to the loads produced by the conditions shown in Fig. 53.

On the first occasion of centerbody collar deformation, binding occurred between the collar and the guide tube imposing highly increased loads on the driving mechanism. Because of these loads, two universal joints on the centerbody drive shaft failed. The damage was repaired, and no difficulties with the drive mechanism were experienced during the remainder of the test.

4.5.2 Flow Straightening Screens and Grid Supports

The grid supports which retain the flow straightening screens were sound and performed without failure during testing. Tie wires (used to retain the screens to the grids) failed, and the screen wire chaffed and shed wires on several different occasions. Fatigue due to the turbulent airstream was the cause. It was found during subsequent testing that this problem could be eliminated by using a greater number of wire ties to prevent relative motion among ties, screens, and retaining grids.

To ensure to the highest degree possible that no wires or wire ties fail and are ingested into the engine compressor during the engine portion of this program, the screens and wire ties must be closely inspected prior to each test period.

4.5.3 Instrumentation Rakes and Apparatus

On several different occasions the pressure rakes, installed at the 22.5- and 202.5-deg locations at the simulator inlet (Fig. 54), experienced a loss of the bulletnose alignment pins. Replacement of the pins was made only to have them fail again shortly thereafter. Since the rakes are very solidly constructed and the data sensed by the rakes were not adversely affected by the loss of the pins, operation without the pins (or a change in the type of rake to be used) would be highly desirable during the engine portion of this test to prevent possible damage to the engine.

The slip ring instrumentation lead-out tube (Fig. 3c and Section II) experienced several difficulties during testing. On several different occasions lock and alignment pins in the tube and on the lead-out strut were found to be broken, bent, or jammed in retracted positions and did not lock properly. Repair of the broken pins by brazing was accomplished, but failure again occurred. A design change to alleviate the pin problem will be required to prevent ingestion of such pins into the engine during the second phase of this program. In addition to the pin problem, slip ring inner cooling air tube supports were found broken when the assembly was removed after testing. It is believed that this was caused by improper assembly or the lack of proper support resulting from the omission in the assembly of internal components which will be installed for the engine portion of the test. (These internal components were not required during the simulator phase of the test since aerodynamic similarity of the tube was not altered by their absence.)

4.5.4 High Dynamic Pressure Proof Test

To ensure that the turbulence generator and installation was sound enough to use in front of an engine, the system was operated at a steady-state condition of 23.0-psia total pressure at the simulator inlet (this pressure level is the highest to be used during the engine phase of testing). In addition to this steady-state operation, the inlet of the simulator was subjected to a pressure spike with a total pressure of 34.0 psia for 12-sec duration and a level in excess of 25 psia for approximately 25 sec. (The spike was provided by the failure of a control valve at the inlet to the test cell.) Inspection of the installation after these loads were applied revealed no failures in the apparatus.

SECTION V

SUMMARY OF RESULTS

The results obtained during this investigation and calibration are summarized as follows:

1. Sufficiently high values of turbulence amplitude may be obtained at various values of total pressure distortion to allow meaningful testing of a turbojet engine under turbulent inlet flow conditions. Values of peak-to-peak turbulent pressure amplitude up to 28.4 (0- to 50-cps bandwidth) and 57.0 (0- to 600-cps bandwidth) percent of the steady-state total pressure level were obtained with total pressure distortion ranging to 52 percent by using five different screen configurations at the exit plane of the venturi.
2. The turbulent pressure output of the generator is a stationary random (or random with sine mixed) waveform whose frequency distribution (power spectral density function) from 0 to 200 cps is sloping or uniform depending on the venturi inlet Reynolds number. Little difference in the shape of the power spectral density function is found in changing centerbody position or screen configuration.
3. The total pressure distortion produced by the turbulence generator may be either tip or hub radial and is generally of a one/rev circumferential nature.
4. Good airflow measurement at the venturi annulus may be obtained with the centerbody immersed into the venturi between 4 and 23 in. Over this range, the coefficient was found to vary with venturi inlet Reynolds number, annulus area, and screen configuration from 0.929 to 0.978. Satisfactory airflow measurement at the simulator inlet is possible only if the Mach number exceeds 0.40 and total pressure distortion is less than 5 percent.
5. Several difficulties which were experienced with the apparatus during testing have been corrected. Generally, the structural integrity of the turbulence generator, its support assembly, and instrumentation rakes was found to be sufficient to permit safe operation of a turbojet engine. To ensure as safe a situation as possible, extremely careful inspection of retaining pins, screen wires, and retaining wires for the flow straightening screens should be performed prior to each test period with an engine behind the generator.

REFERENCES

1. Test Facilities Handbook, (5th Edition). "Rocket Test Facility, Vol. 2." Arnold Engineering Development Center, July 1963.
2. Bendat, J. S., Enochson, L. D., and Piersol, A. G. "Analytical Study of Vibration Data Reduction Methods." Technical Products Company, September 1963.
3. Lin, C. C. Statistical Theories of Turbulence. Princeton University Press, Princeton, N. J., 1961.
4. Shapiro, A. H. The Dynamics and Thermodynamics of Compressible Fluid Flow, Vol. I. The Ronald Press Company, New York, 1953.
5. Nussdorfer, T. J. "Some Observation of Shock-Induced Turbulent Separation on Supersonic Diffusers." NACA RME51L26, May 1954.
6. Schlichting, H. Boundary Layer Theory, (4th Edition). McGraw-Hill Book Company, Inc., New York, 1960.

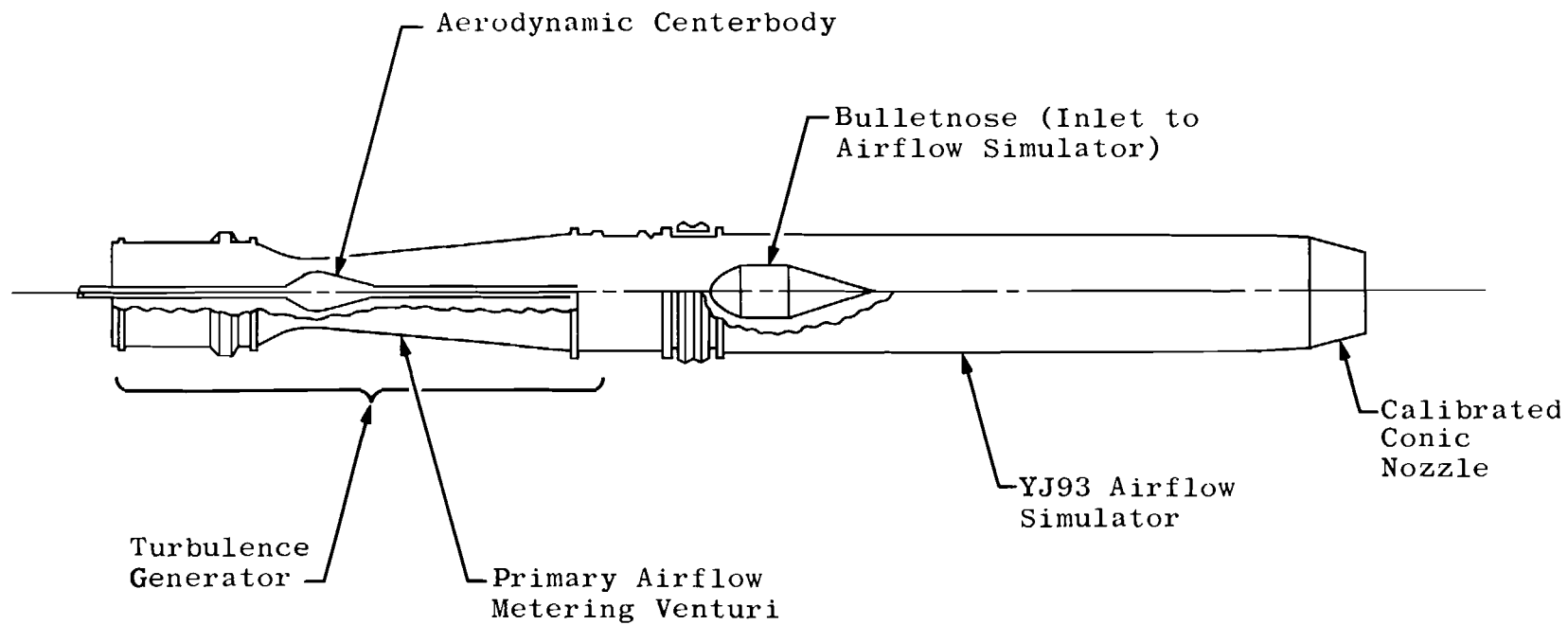
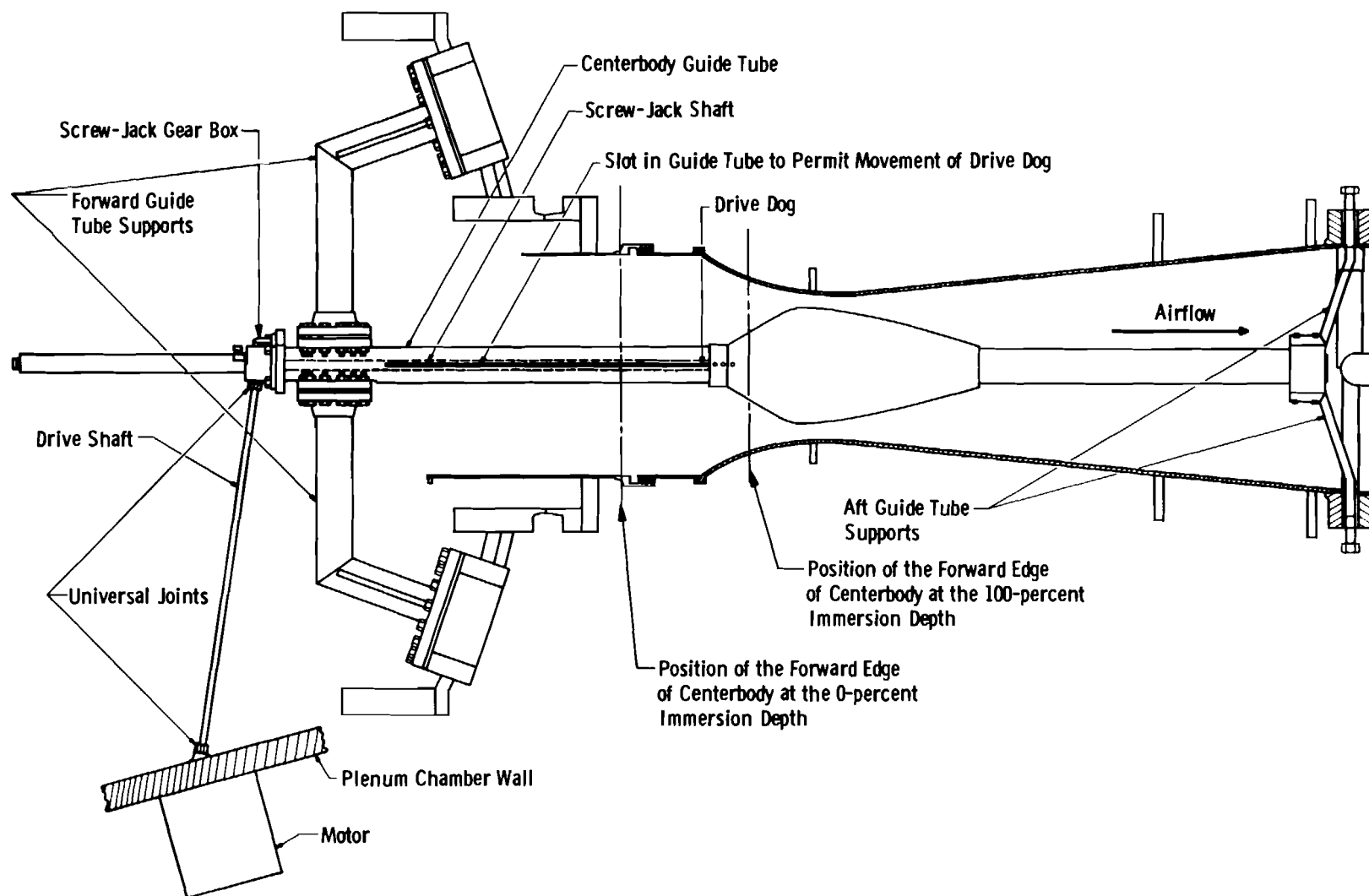
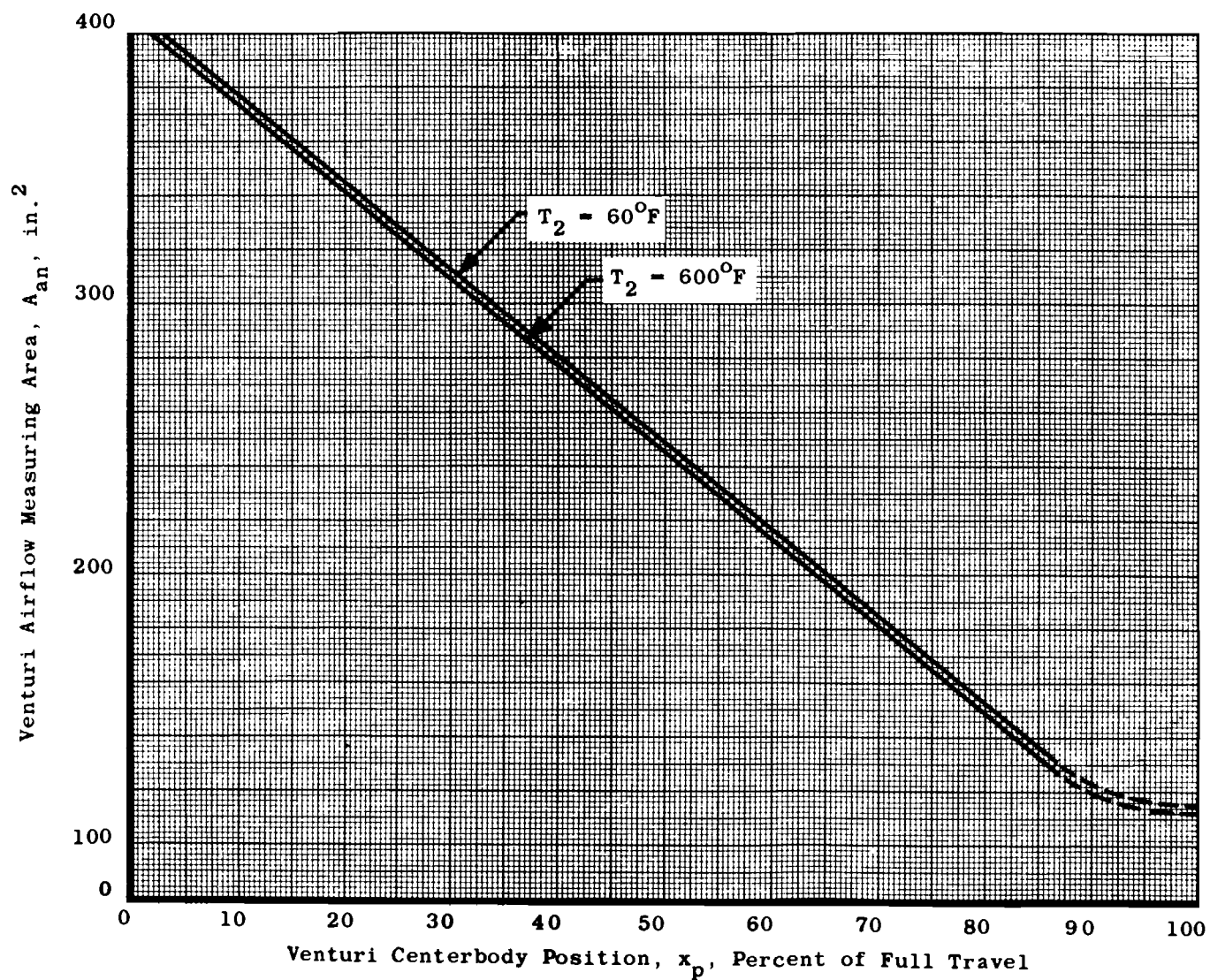


Fig. 1 YJ93 Airflow Simulator and Turbulence Generator



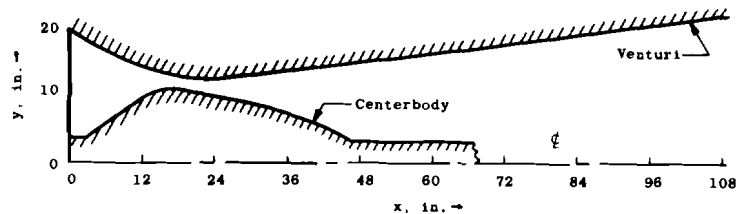
a. Schematic

Fig. 2 Turbulence Generator



b. Variance of Throat Area with Centerbody Immersion Depth

Fig. 2 Continued



Equations of Contour for Venturi Wall

$$\begin{aligned}
 0 \leq x \leq 23.09 & \quad x^2 - 46.18x + y^2 - 107.99y + 1655.509 = 0 \\
 23.09 \leq x \leq 29.97 & \quad y = 11.6502 + \left\{ 0.023586 (x - 23.09) \right. \\
 & \quad \left. + 0.011847 \left[\frac{(x - 23.09)^2}{2} \right. \right. \\
 & \quad \left. \left. - 2.41376 \cos \frac{\pi (x - 25.09)}{4.88089} \right] \right\} \\
 29.97 \leq x \leq 108.21 & \quad y - 0.1051x - 8.98 = 0
 \end{aligned}$$

Equations of Contour for Venturi Centerbody

$$\begin{aligned}
 0 \leq x \leq 3.0 & \quad y = \text{constant} = 3.489 \\
 3.0 \leq x \leq 11.572 & \quad y - 0.5773x - 1.757 = 0 \\
 11.572 \leq x \leq 16.588 & \quad x^2 - 33.176x + y^2 + 175.641 = 0 \\
 16.588 \leq x \leq 47.588 & \quad y = 6.19908 + 0.738182x \\
 & \quad - 0.04486315x^2 \\
 & \quad + 0.000989692x^3 \\
 & \quad - 0.00000838113x^4
 \end{aligned}$$

Coordinates of Venturi Wall

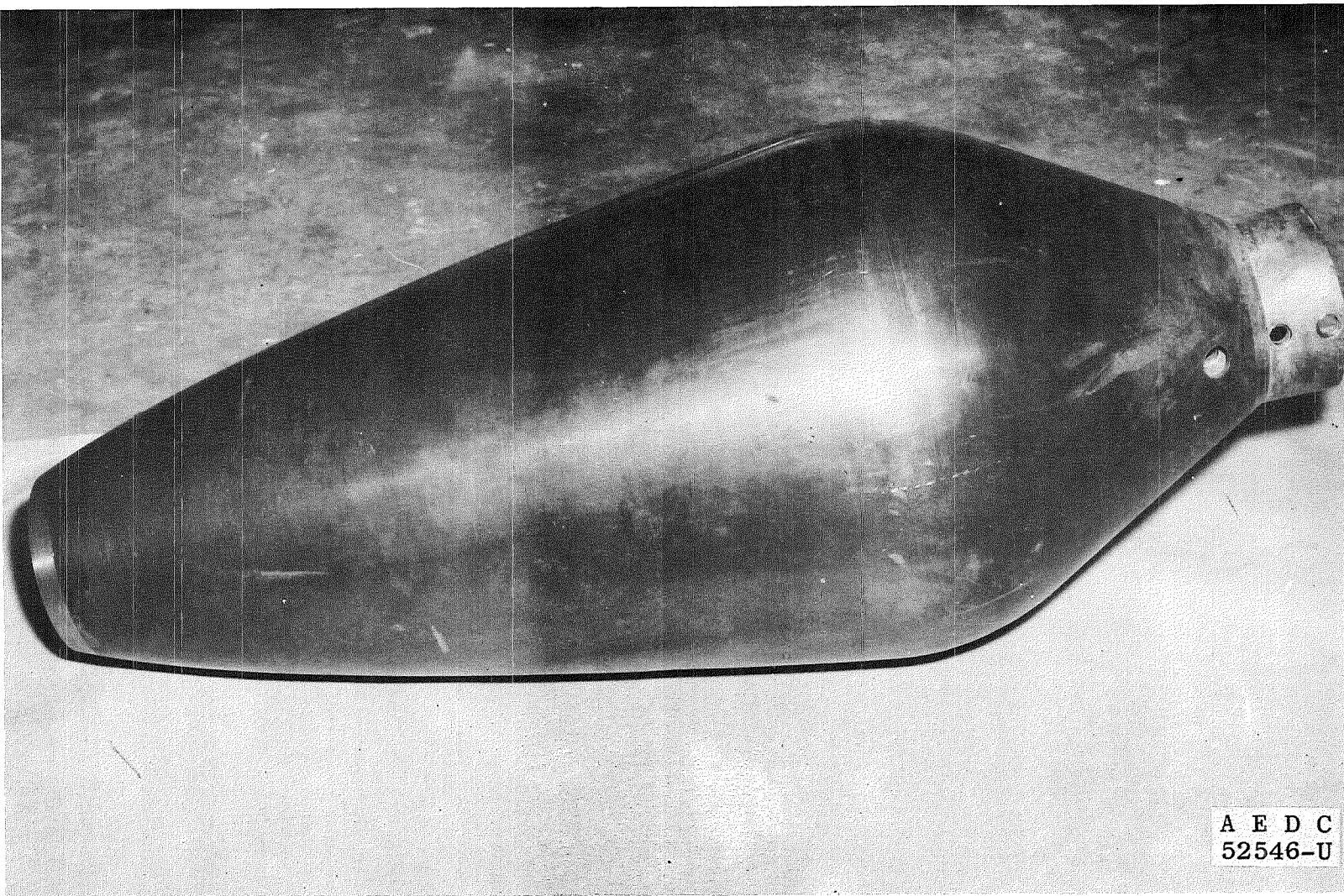
x	y
0.00	18.5000
4.00	16.2023
8.00	14.4338
12.00	13.1307
16.00	12.2495
19.09	11.8394
23.09	11.6500
25.00	11.6973
26.00	11.75
27.00	11.83
28.00	11.92
29.00	12.02
29.97	12.13
35.09	12.66
71.09	16.45
108.21	20.35

Coordinates of Venturi Centerbody

x	y
0.00	3.489
3.00	3.489
11.572	8.438
16.588	9.976
20.588	9.499
24.588	8.858
28.588	8.173
32.588	7.421
36.588	6.585
40.588	5.651
44.588	4.490
47.588	3.397

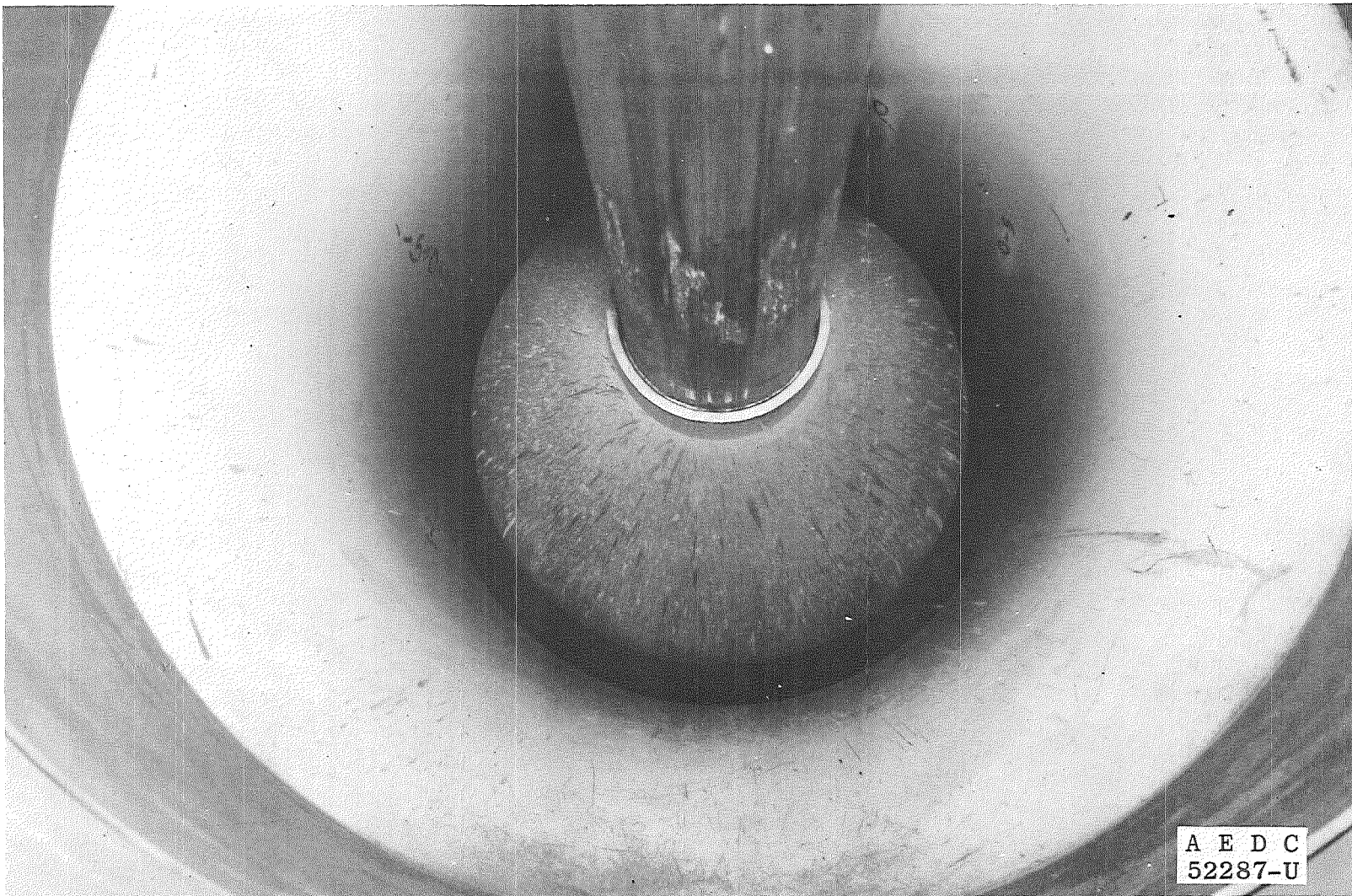
c. Venturi and Centerbody Coordinates

Fig. 2 Continued



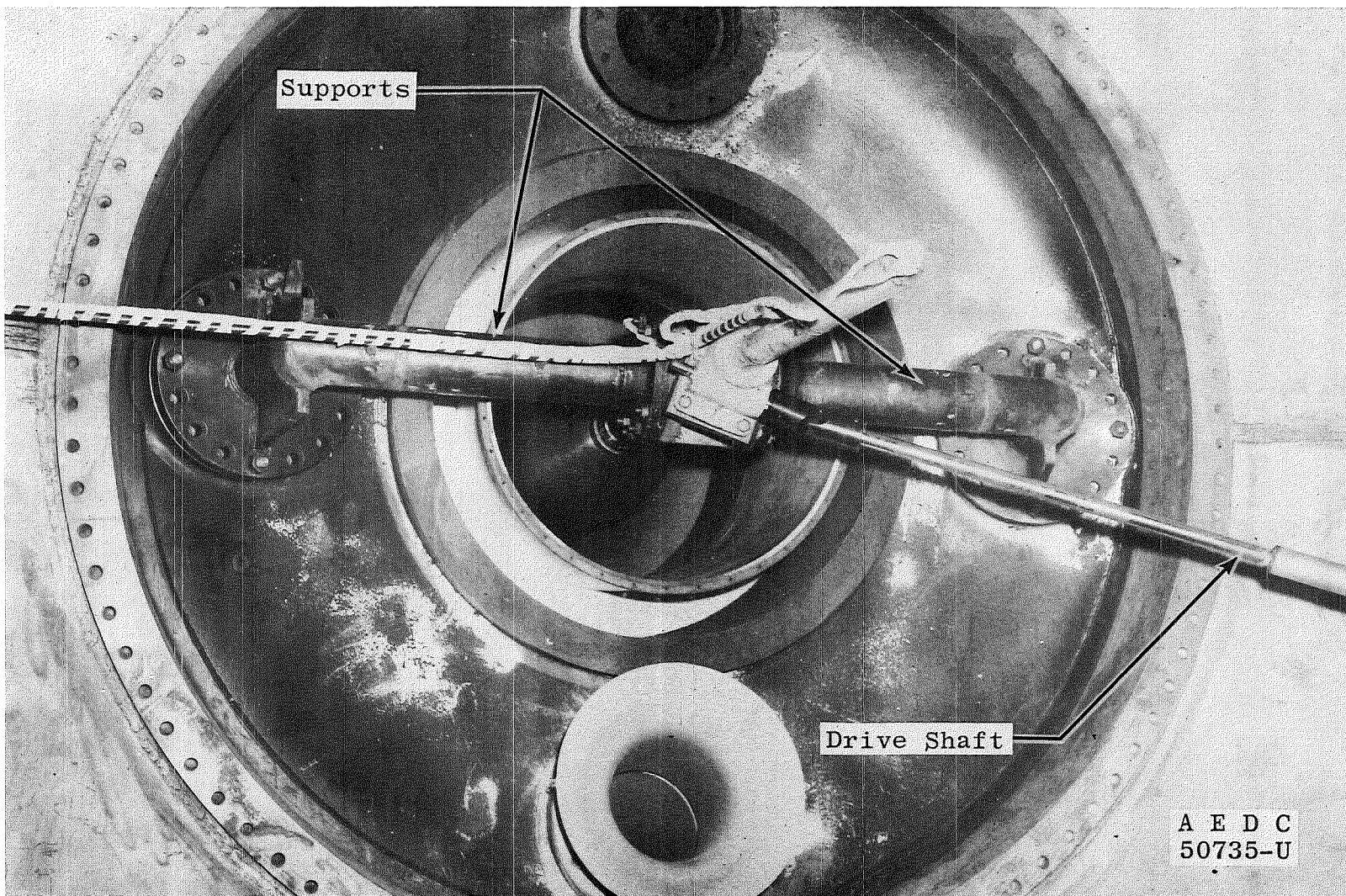
d. Venturi Centerbody

Fig. 2 Continued

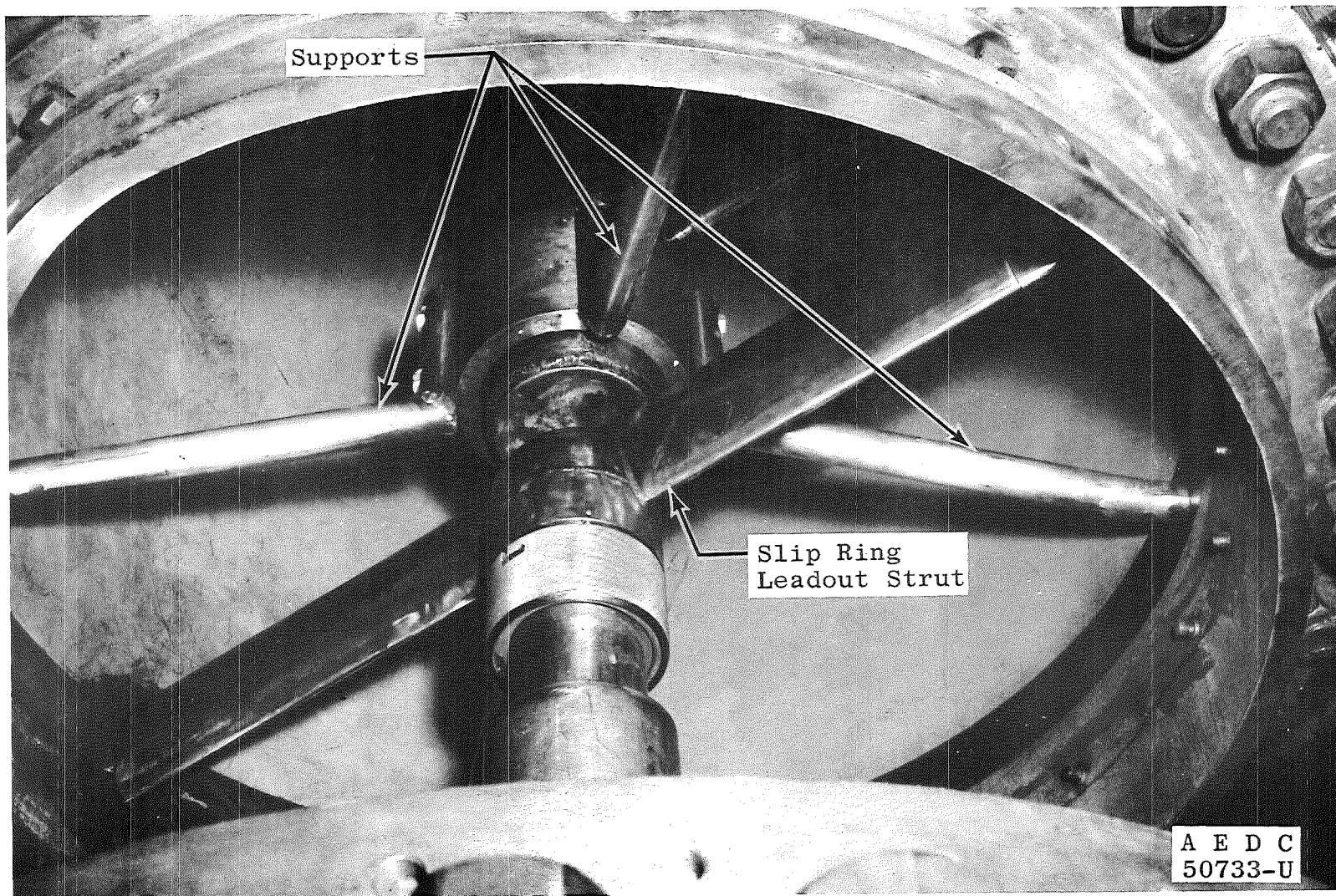


e. Venturi Centerbody Installed in Venturi

Fig. 2 Concluded

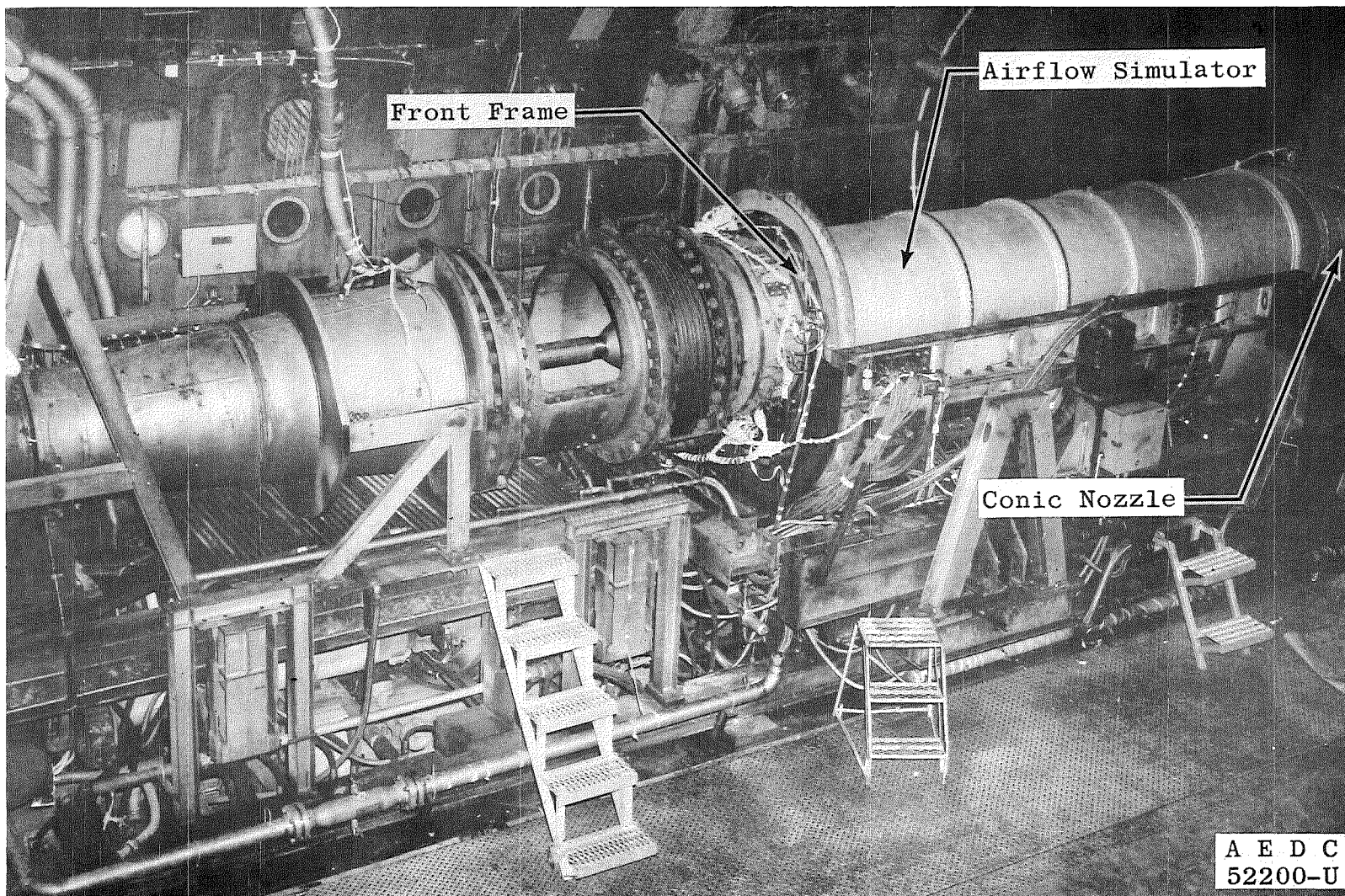


a. Forward Guide Tube Supports
Fig. 3 Installation of Venturi Centerbody



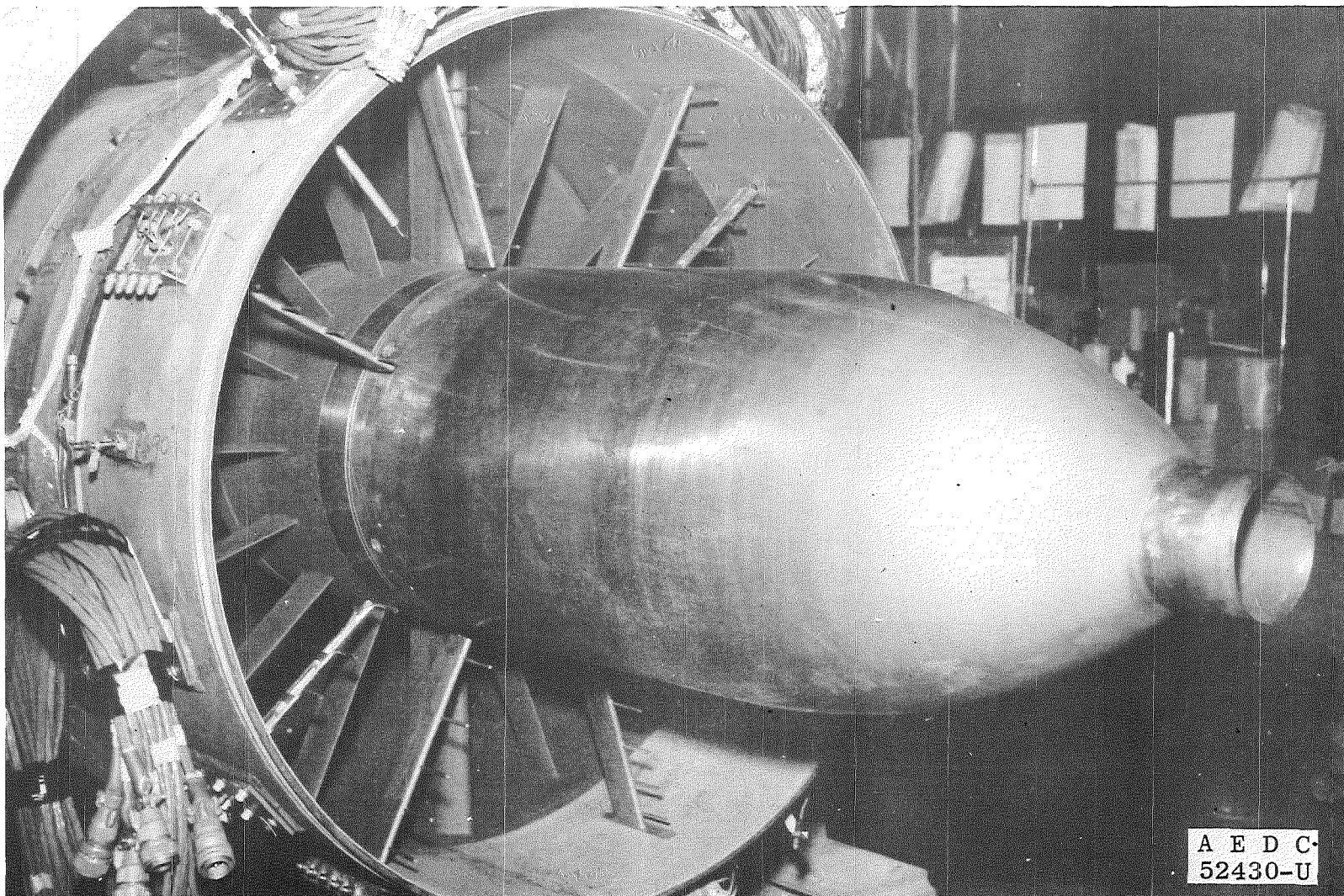
b. Aft Guide Tube Supports

Fig. 3 Concluded



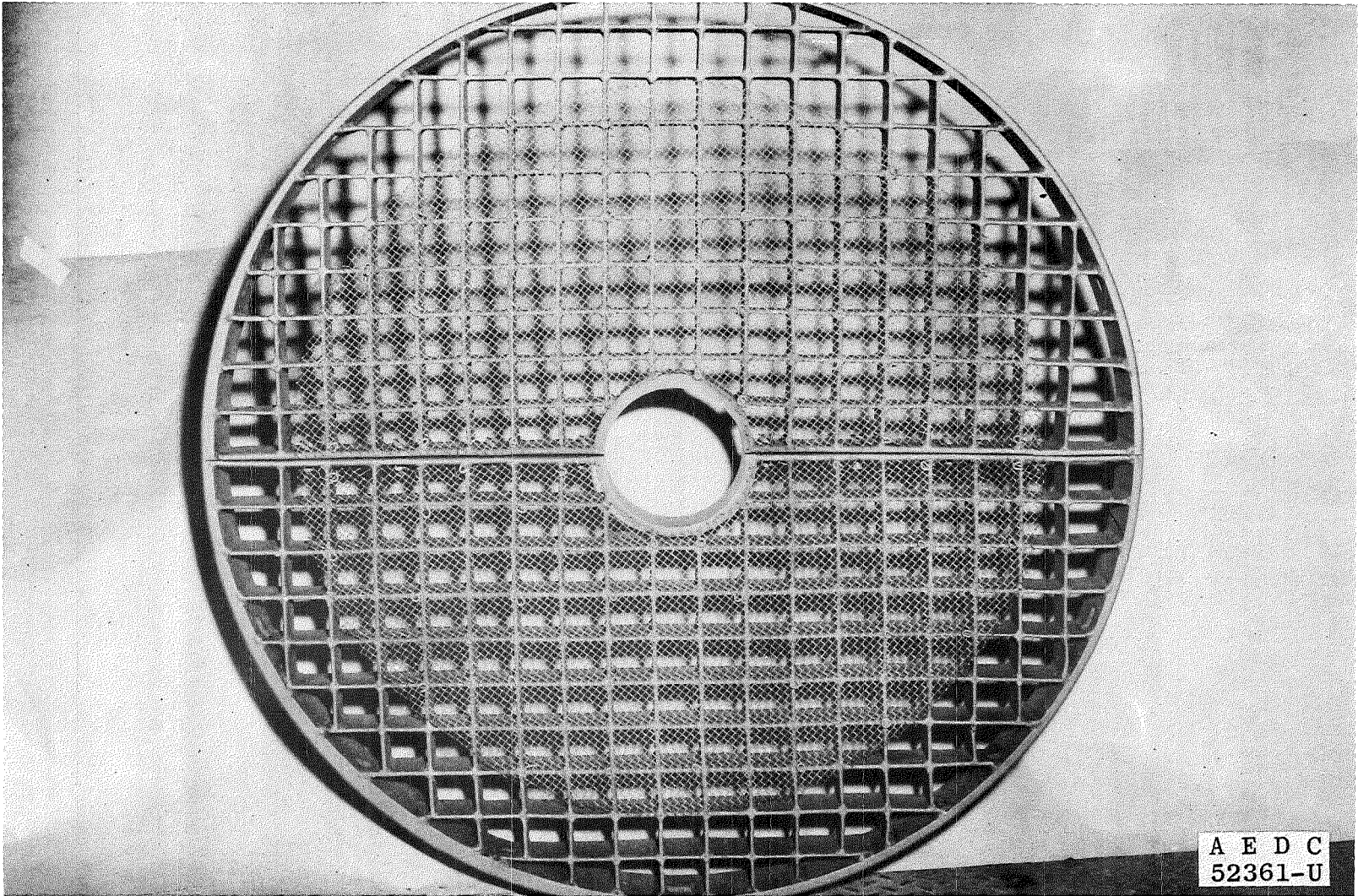
a. Photograph

Fig. 4 YJ93 Airflow Simulator



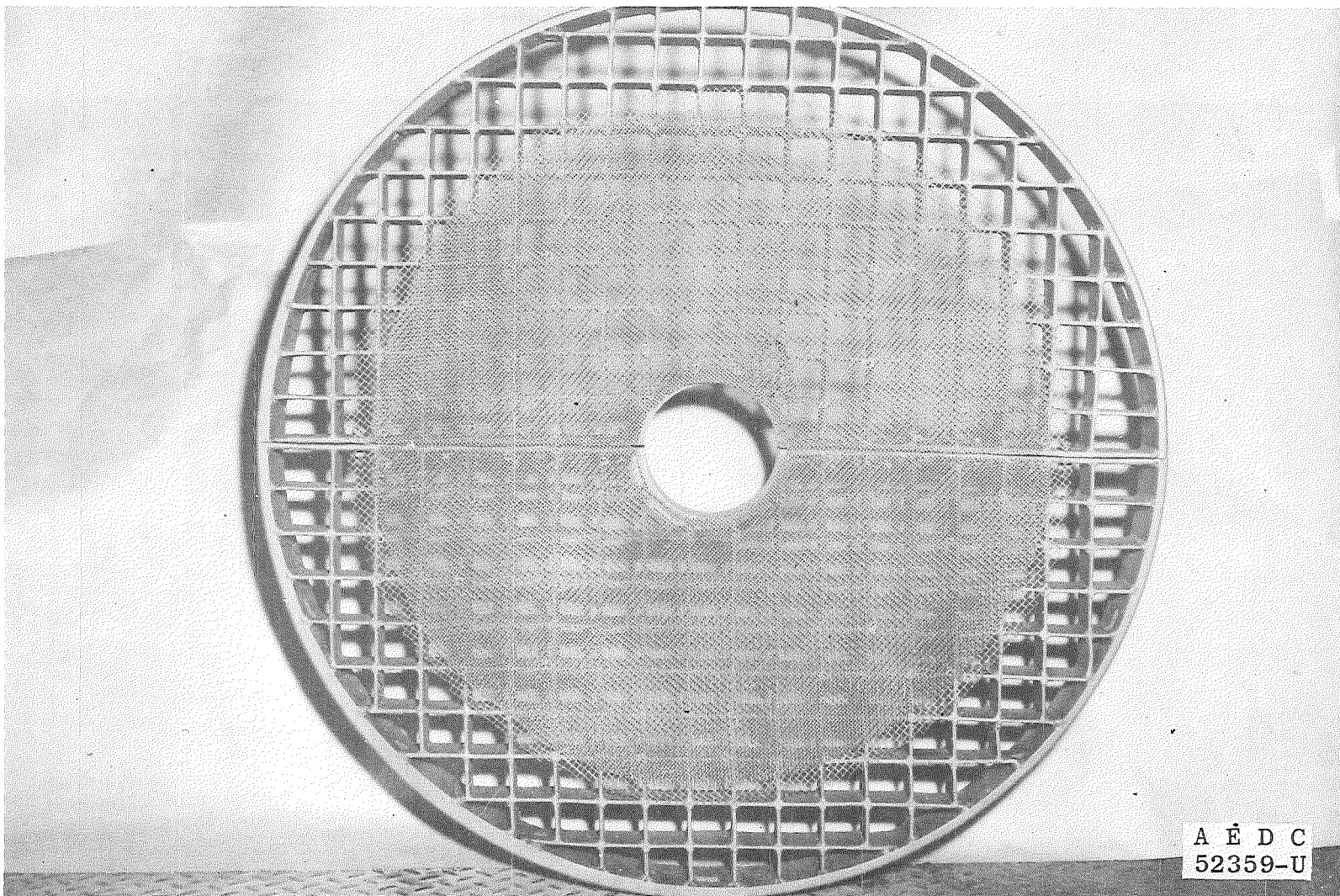
b. Long Bullethead

Fig. 4 Concluded



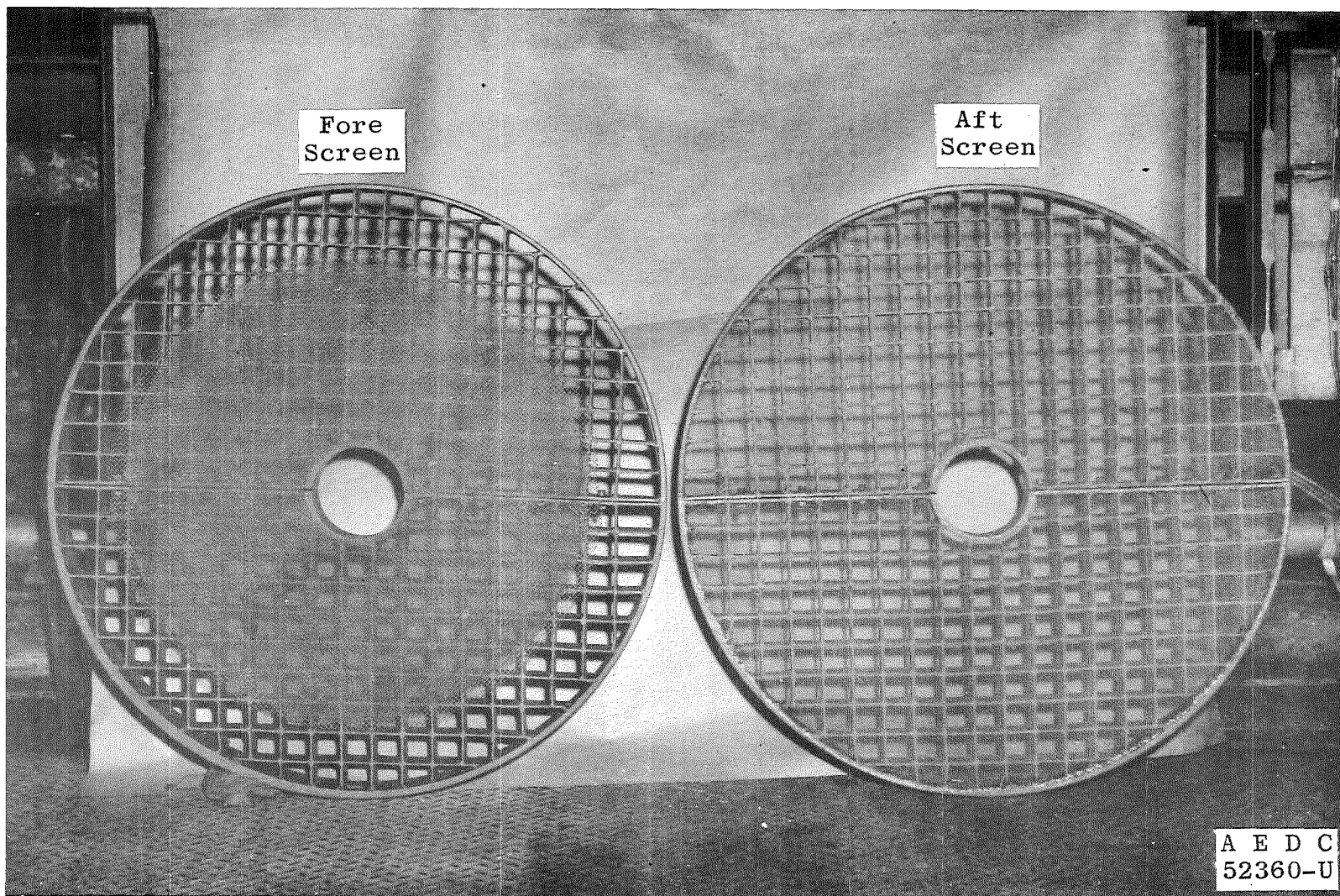
a. Light Blockage Screen

Fig. 5 Screen Configurations



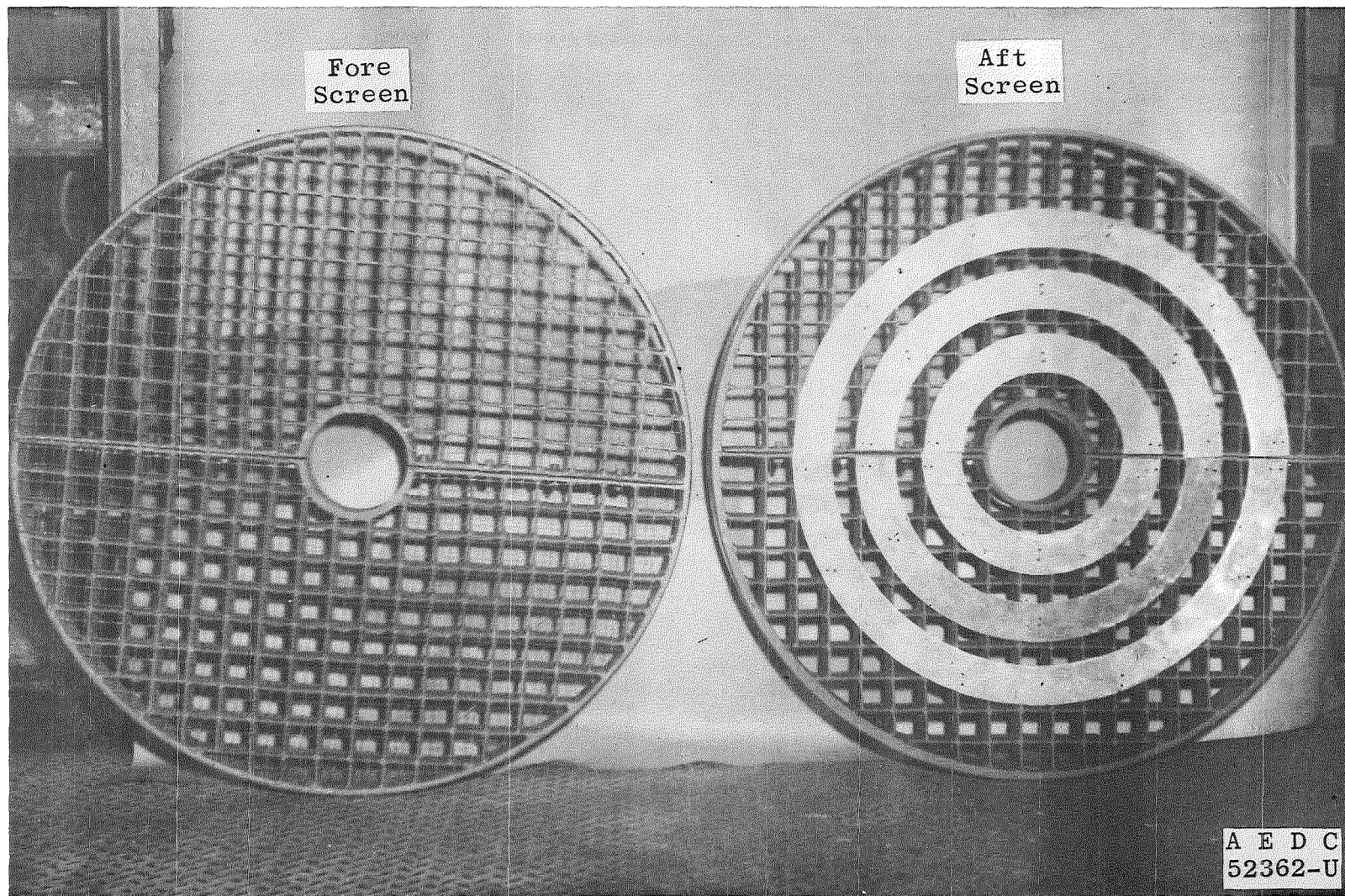
b. Intermediate Blockage Screen

Fig. 5 Continued



c. Heavy Blockage Screen Configuration

Fig. 5 Continued



d. Vortex Generator Screen Configuration

Fig. 5 Concluded

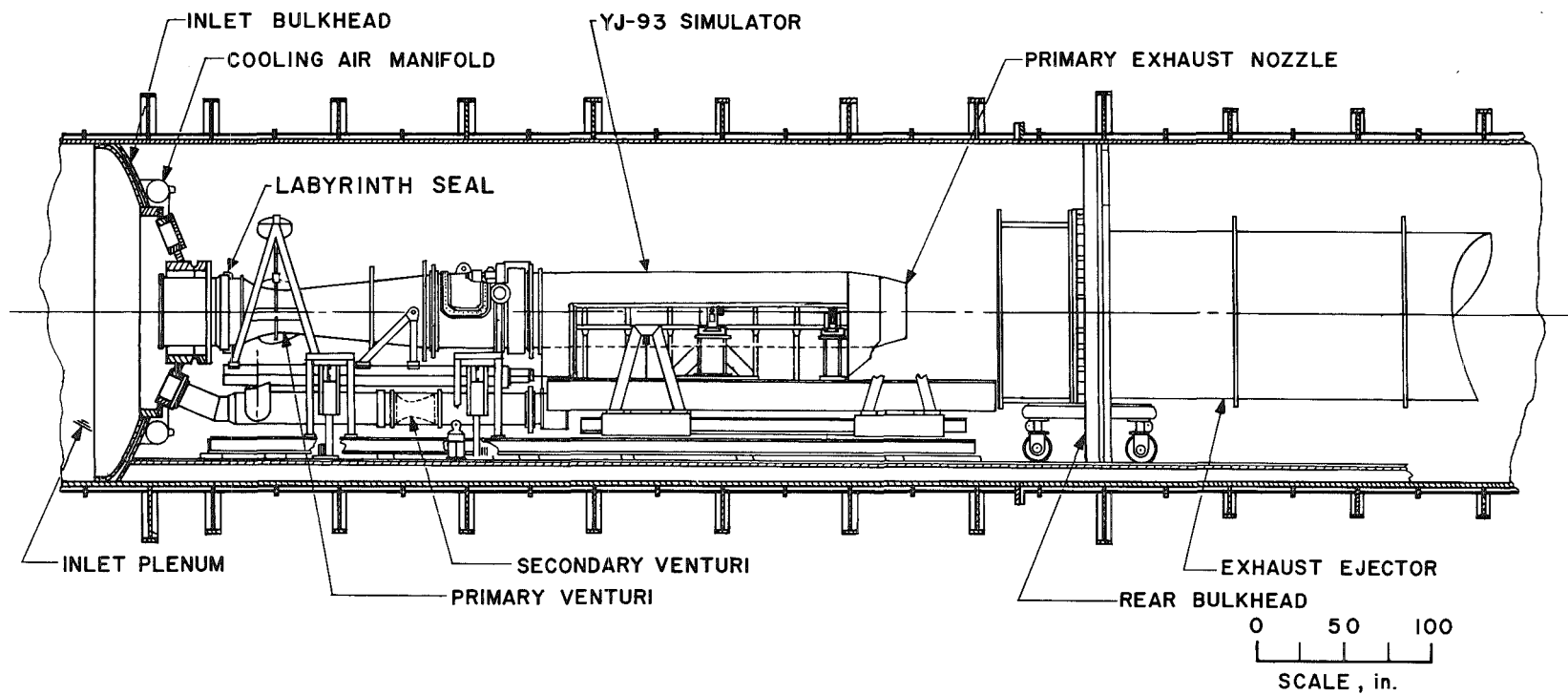
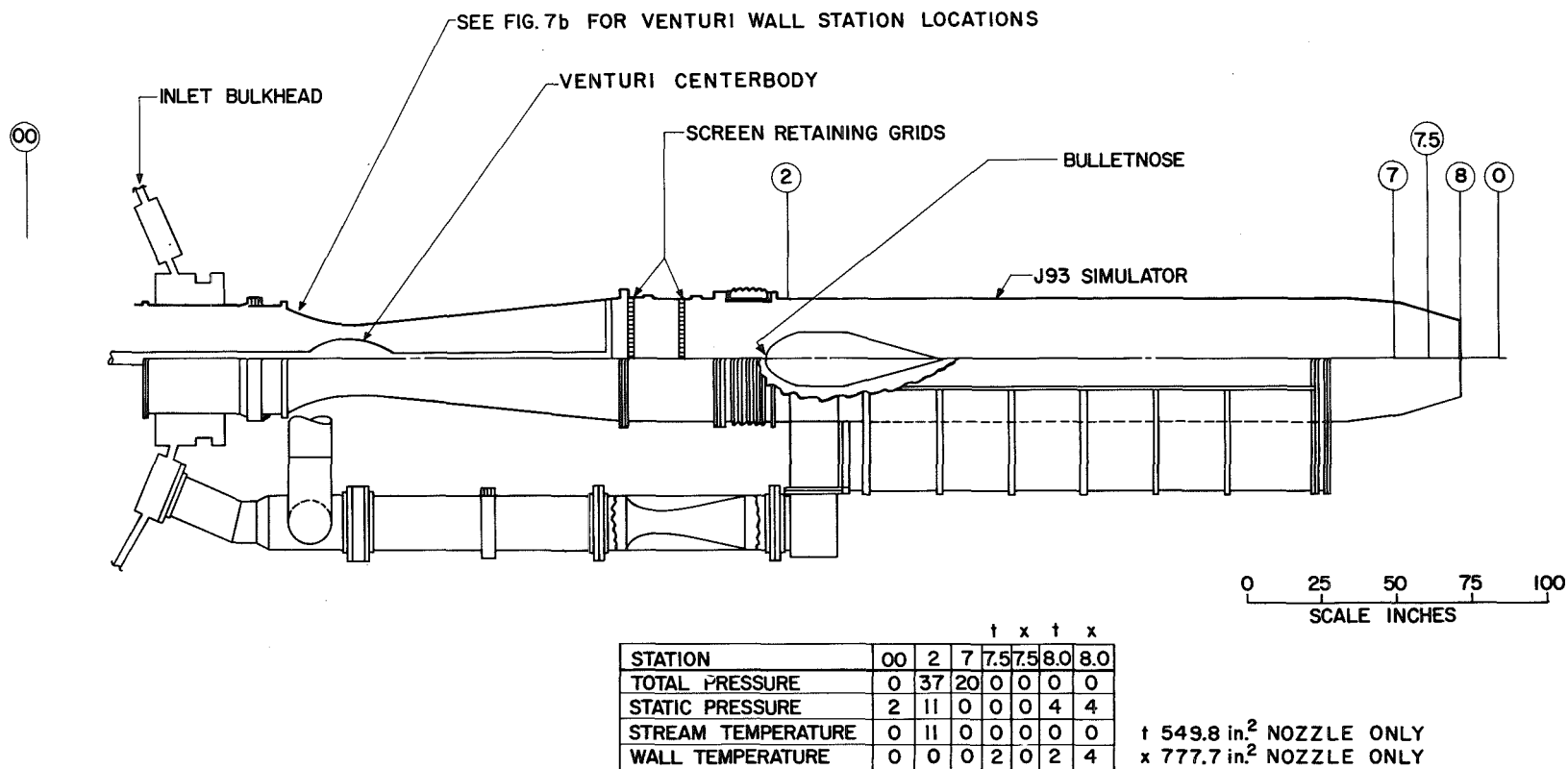
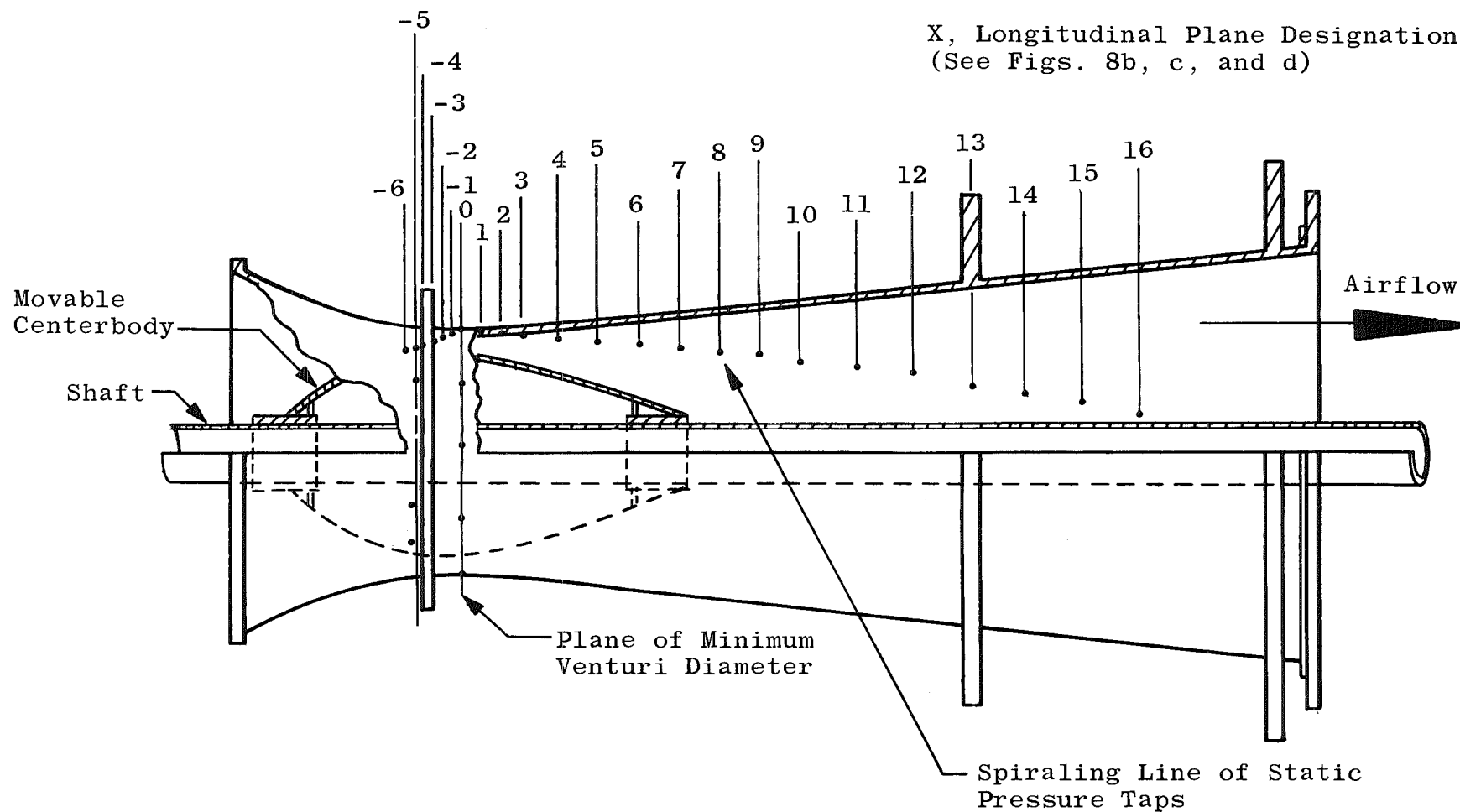


Fig. 6 Installation of the YJ93 Simulator in Propulsion Engine Test Cell (J-1)



a. Longitudinal Location of Simulator Measuring Planes

Fig. 7 Instrumentation Station Locations



b. Venturi Wall Static Pressure Measuring Stations

Fig. 7 Concluded

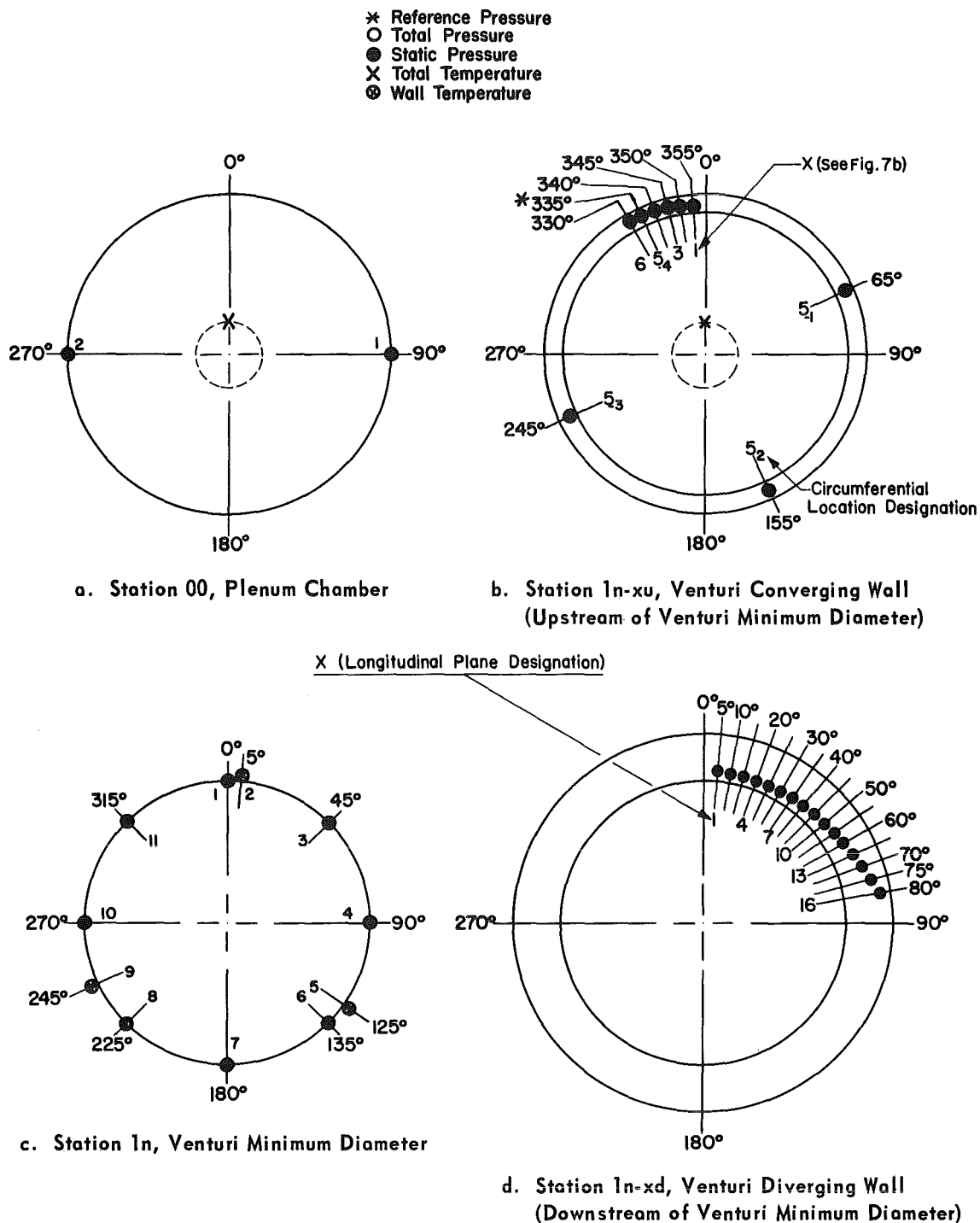
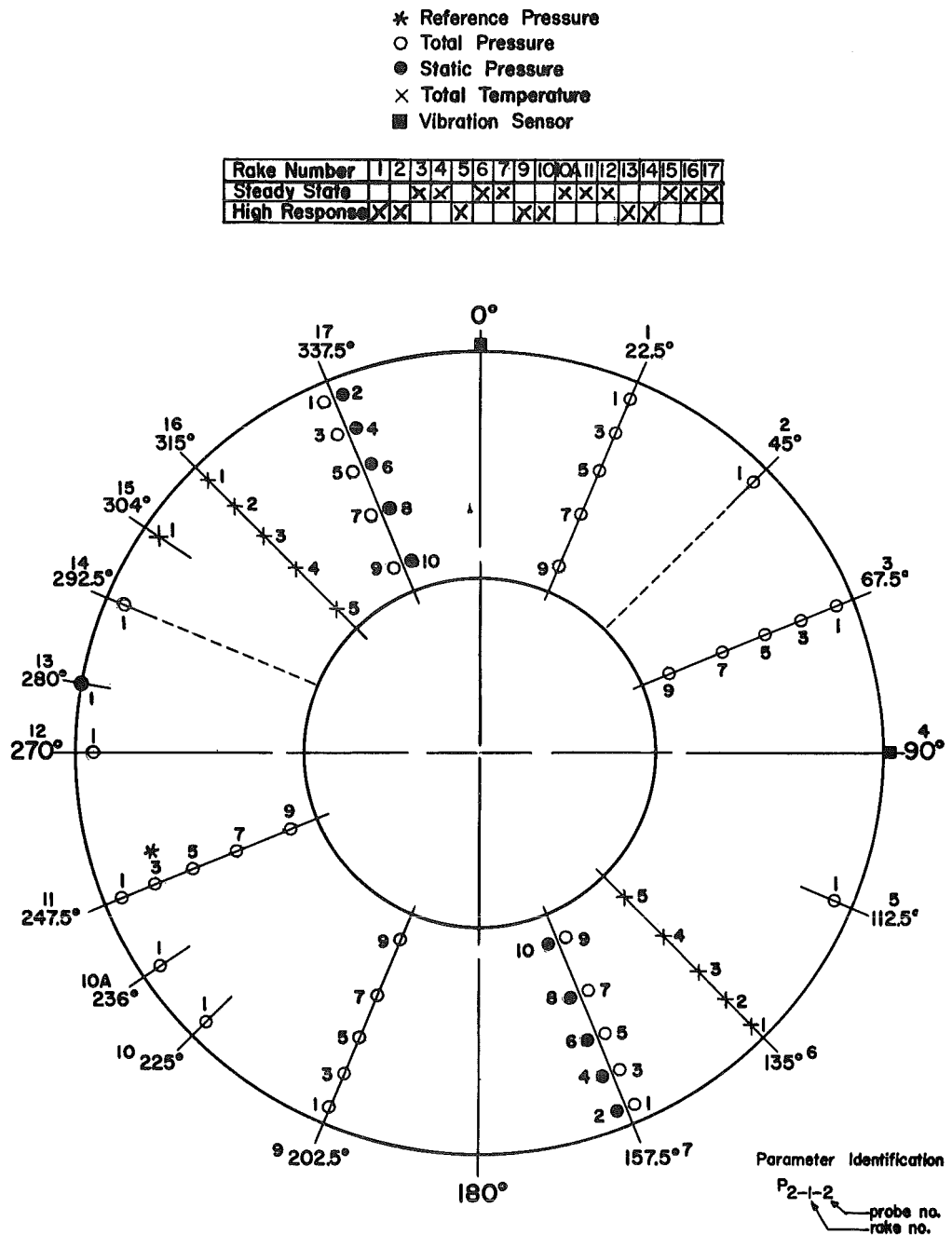


Fig. 8 Instrumentation Station Details (Looking Upstream)



e. Station 2, Simulator Inlet 5.87 in. Upstream of Simulated Compressor Front Frame

Fig. 8 Continued

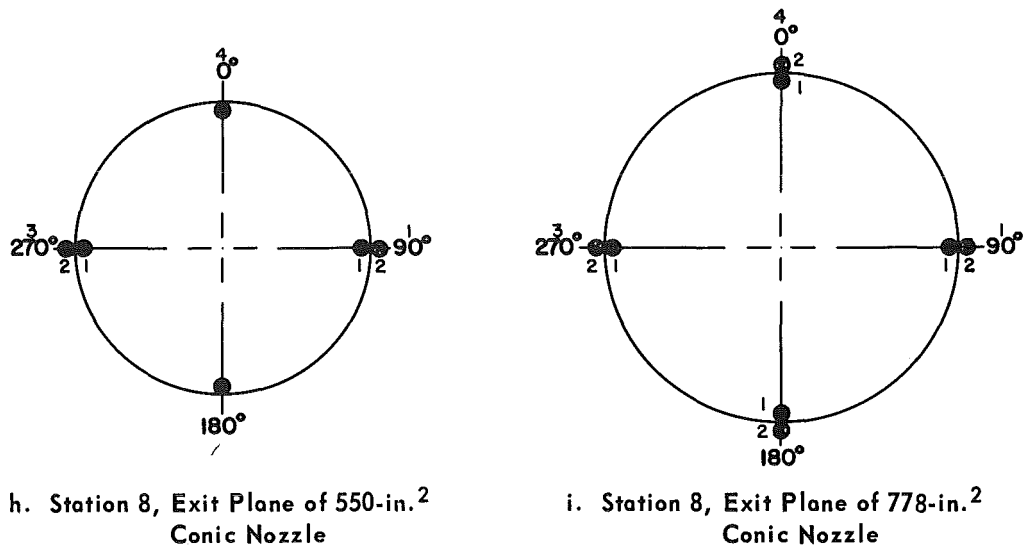
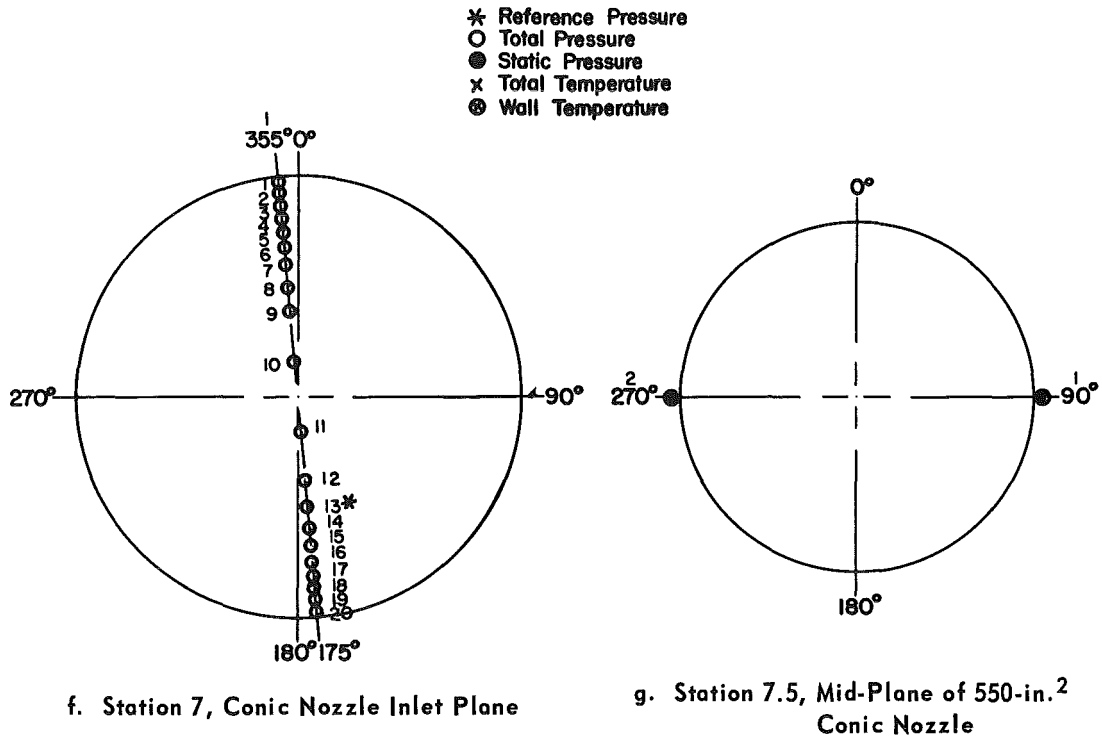
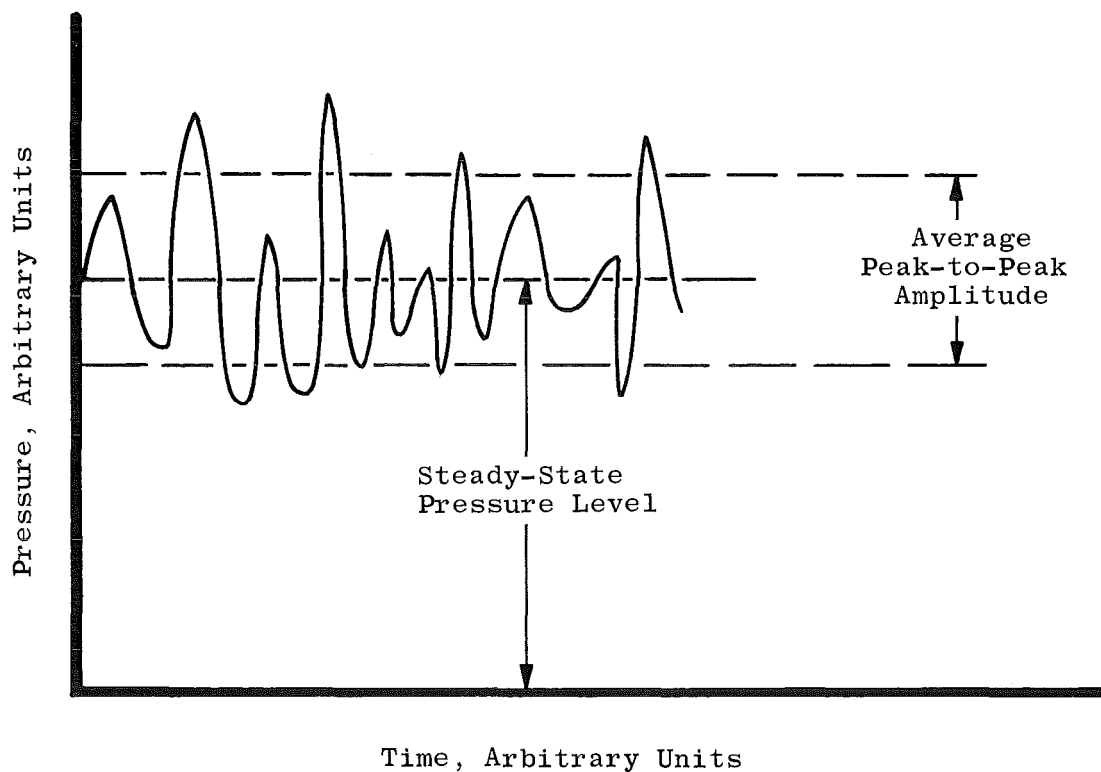
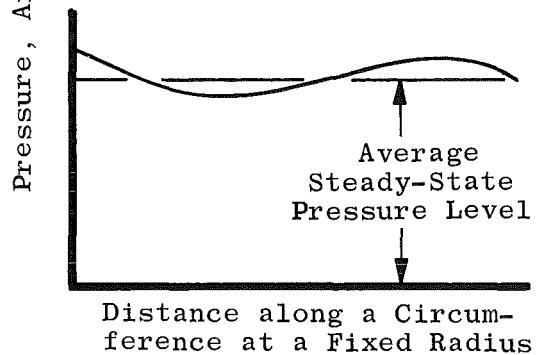
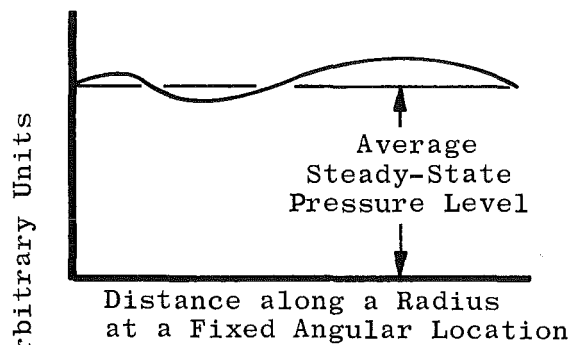


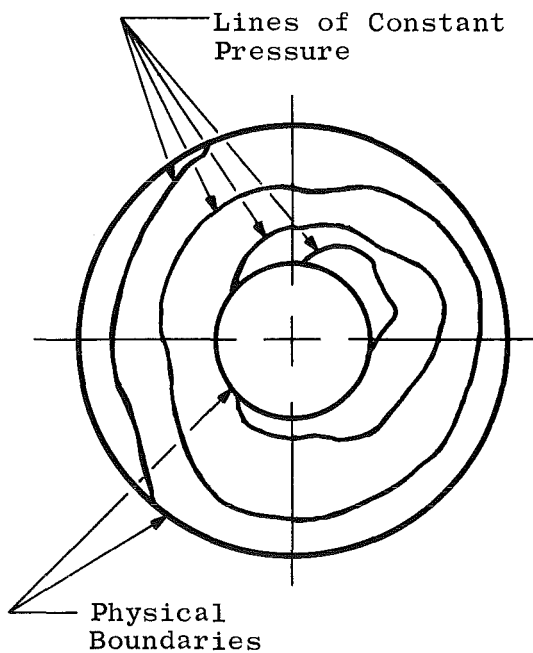
Fig. 8 Concluded



a. Turbulence

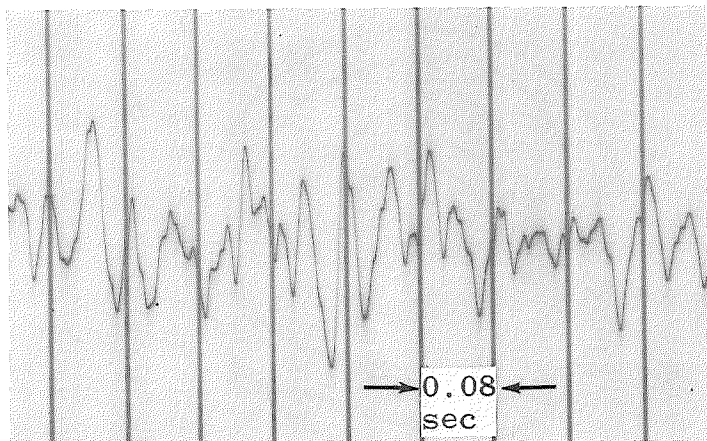


b. Distortion (Rectangular)

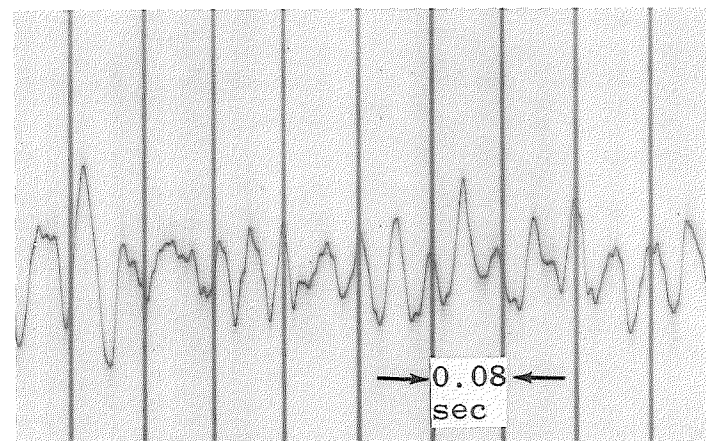


c. Distortion (Polar)

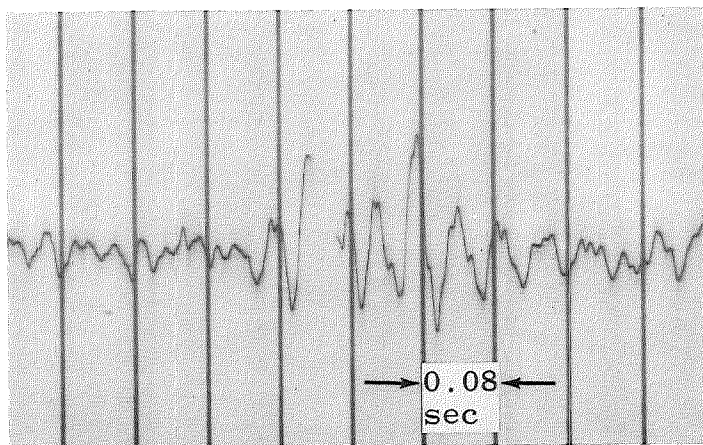
Fig. 9 Graphical Definitions



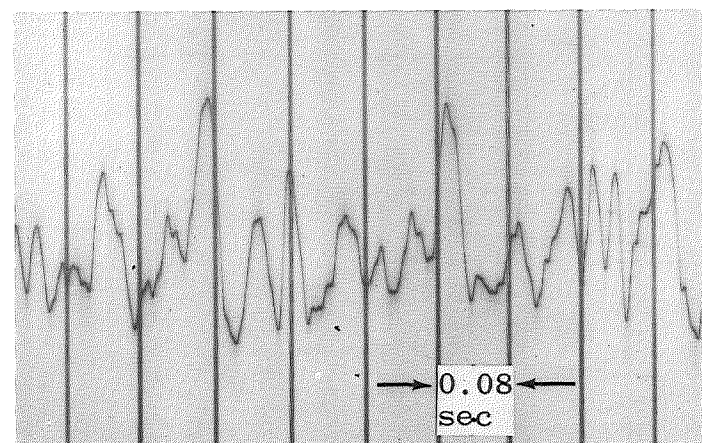
a. Open Screen Configuration,
 $Re_D = 1.0 \times 10^8$,
 $W_{ac} = 145 \text{ lb}_m/\text{sec}$



b. Open Screen Configuration,
 $Re_D = 2.2 \times 10^8$,
 $W_{ac} = 185 \text{ lb}_m/\text{sec}$

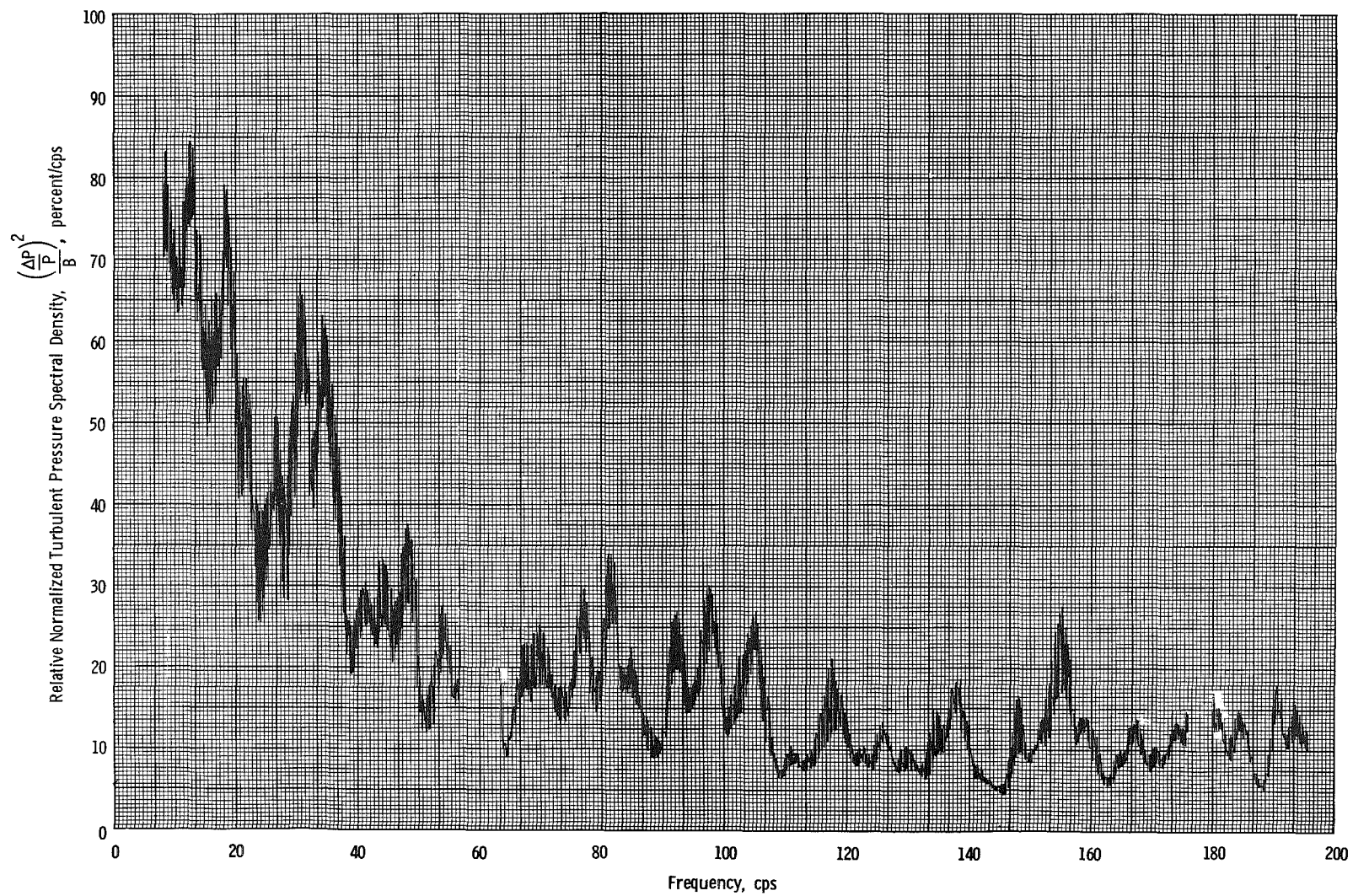


c. Heavy Screen Configuration,
 $Re_D = 1.0 \times 10^8$,
 $W_{ac} = 260 \text{ lb}_m/\text{sec}$



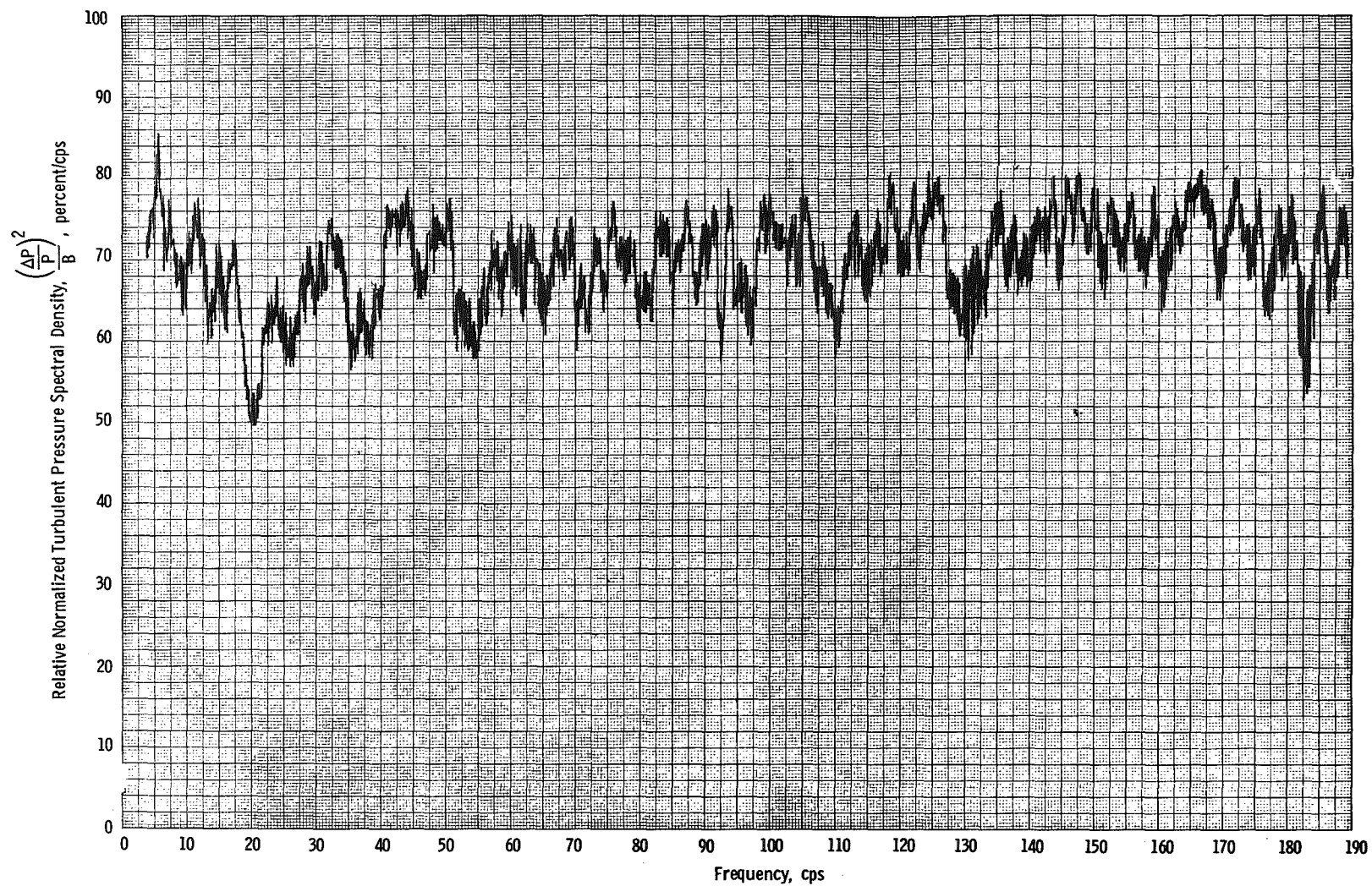
d. Heavy Screen Configuration,
 $Re_D = 3.0 \times 10^8$,
 $W_{ac} = 260 \text{ lb}_m/\text{sec}$

Fig. 10 Turbulence Waveforms



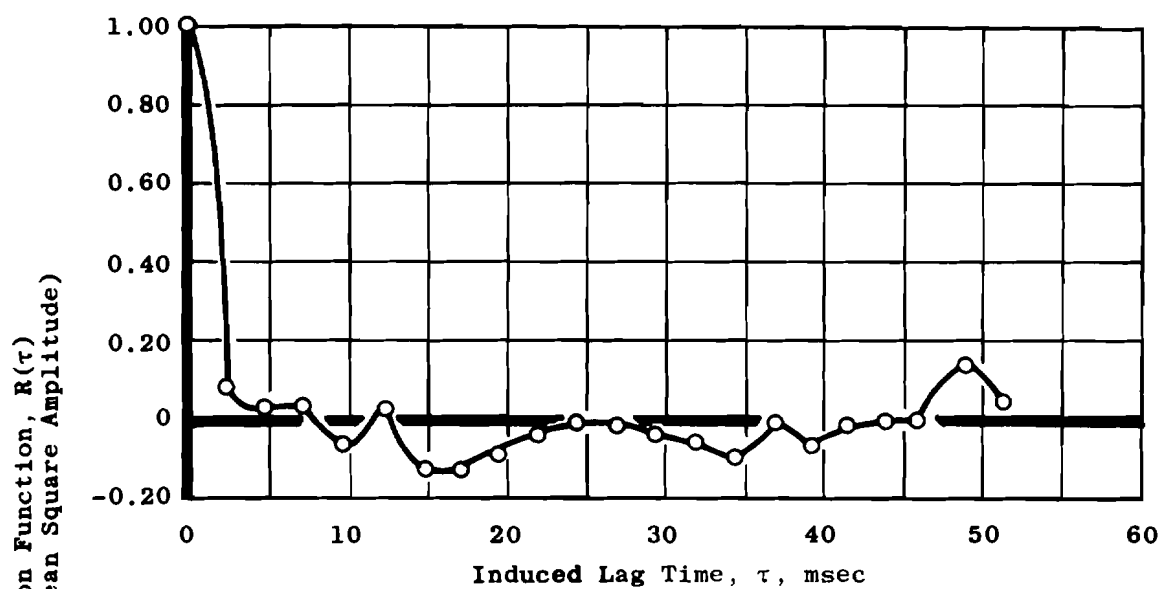
a. Sloping Total Pressure Distribution, Open Screen Configuration, $Re_D = 1.0 \times 10^8$, $W_{ac} = 145 \text{ lb}_m/\text{sec}$

Fig. 11 Typical Power Spectral Density Functions for Turbulent Pressure

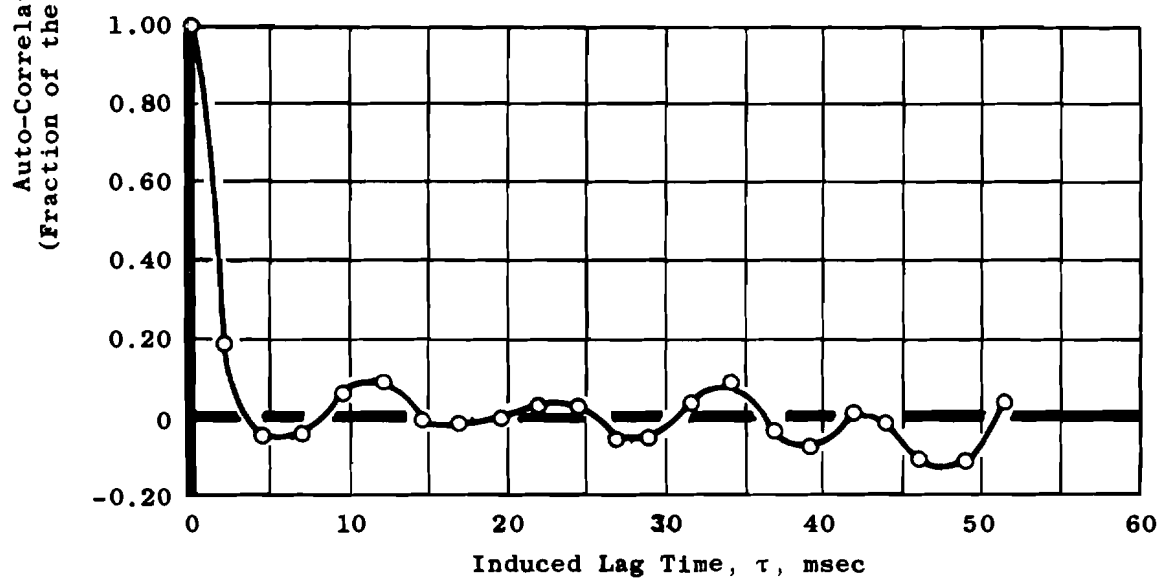


b. Uniform Total Pressure Distribution, Open Screen Configuration, $Re_D = 4.0 \times 10^8$, $W_{ac} = 260 \text{ lb}_m/\text{sec}$

Fig. 11 Concluded



a. Sloping Total Pressure Distribution



b. Uniform Total Pressure Distribution

Fig. 12 Typical Auto-Correlation Functions for Turbulent Pressure

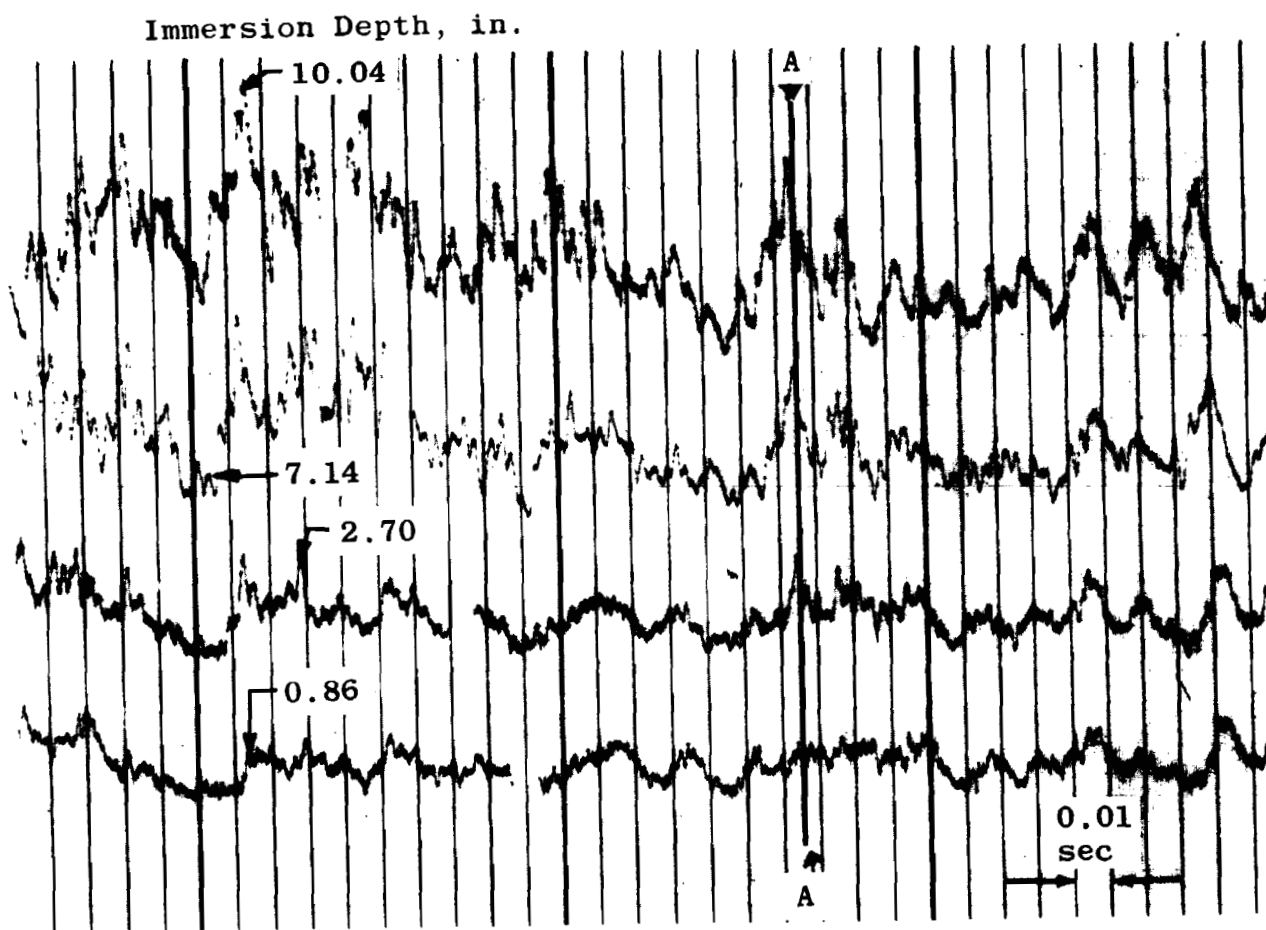


Fig. 13 Turbulence Waveforms at Different Immersion Depth into the Airstream

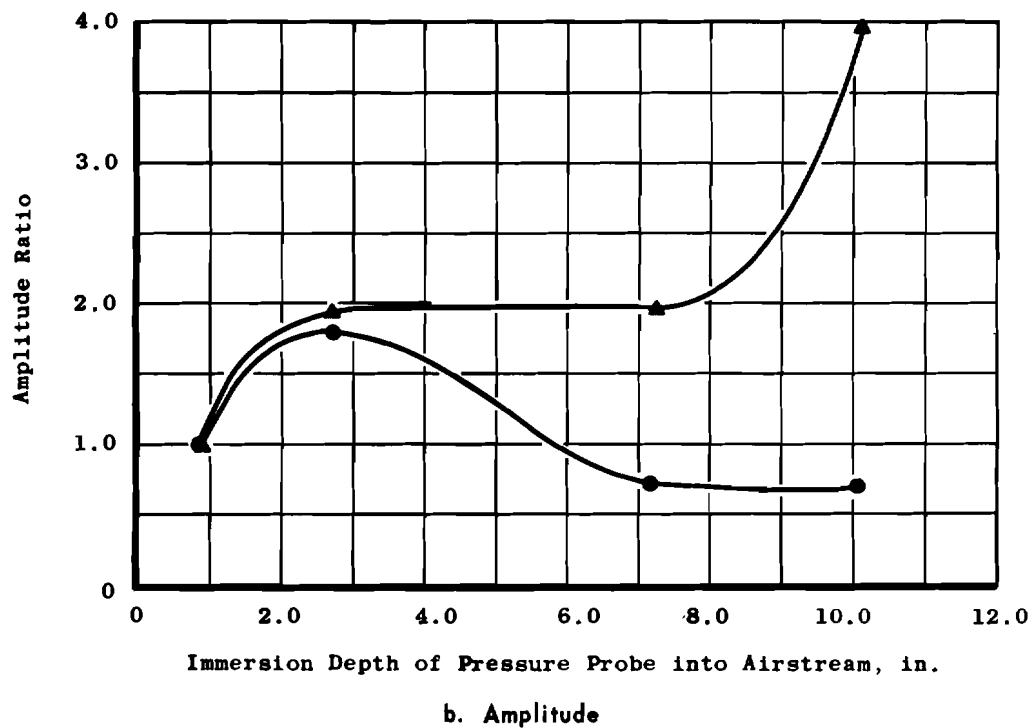
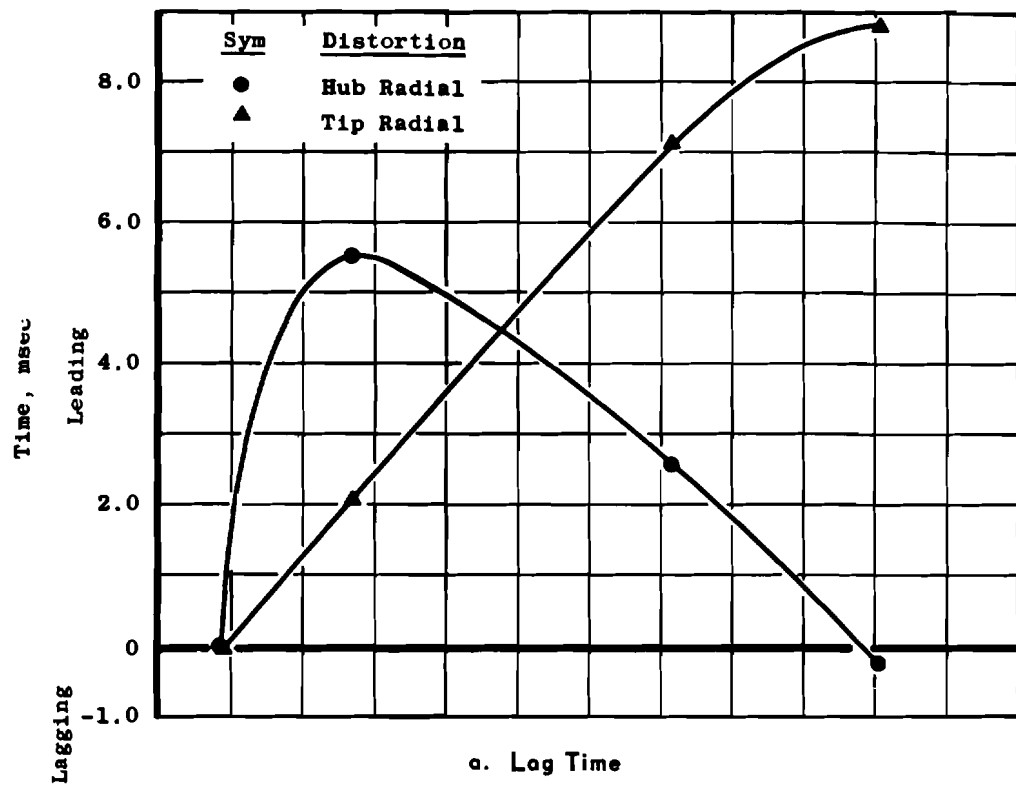


Fig. 14 Turbulence Transmissibility

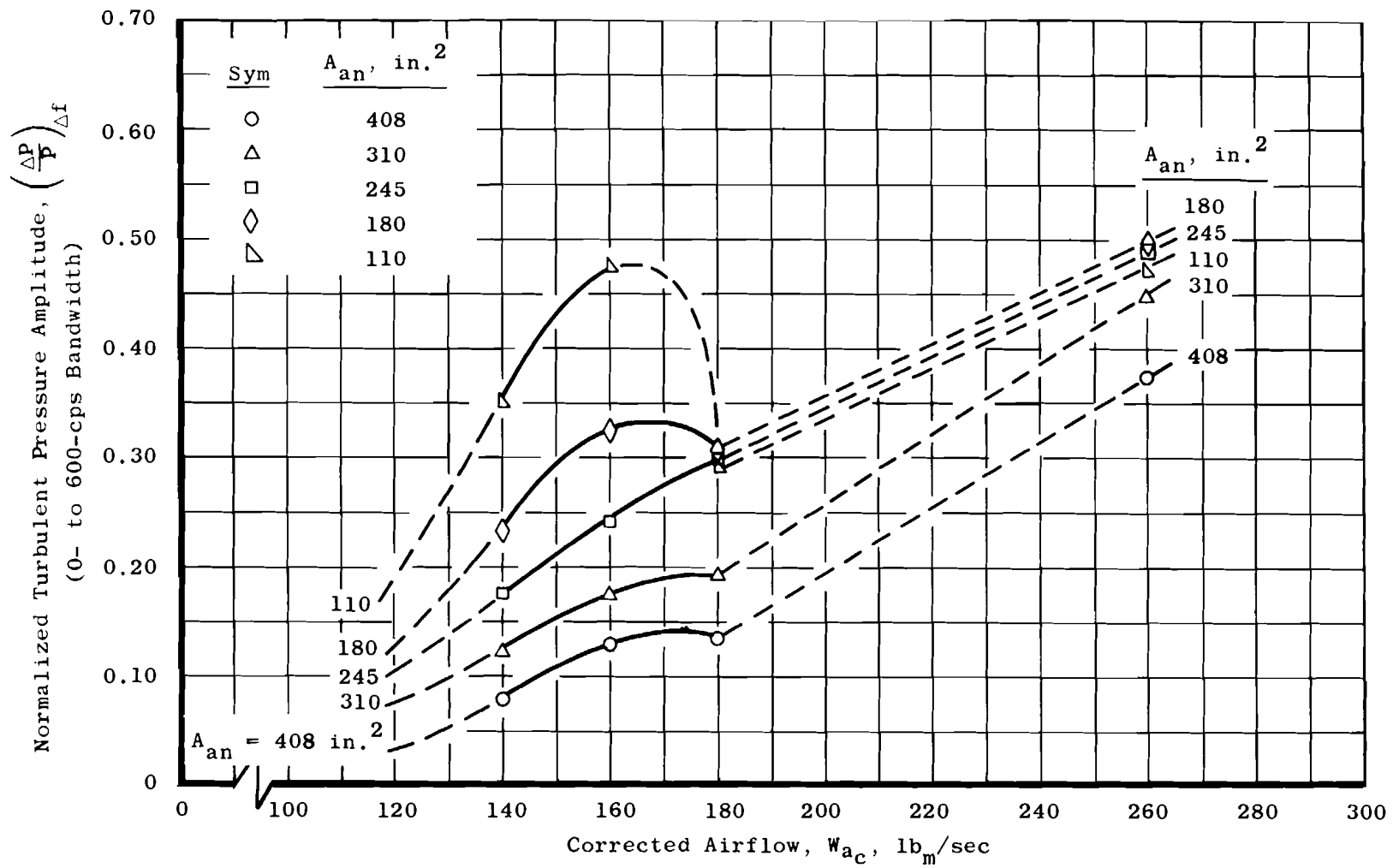


Fig. 15 Variance of Turbulence Amplitude with Corrected Airflow, Open Screen Configuration

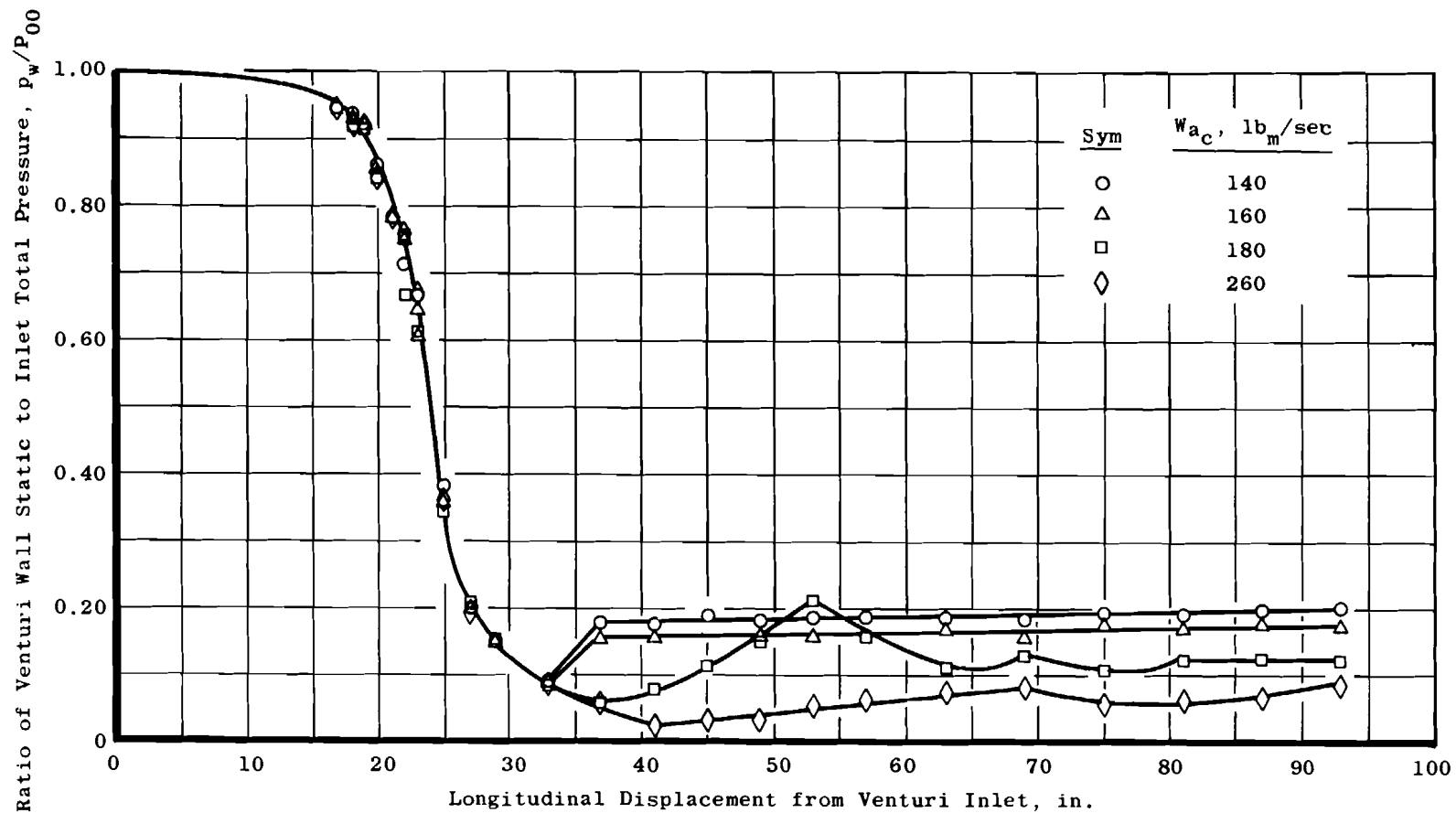
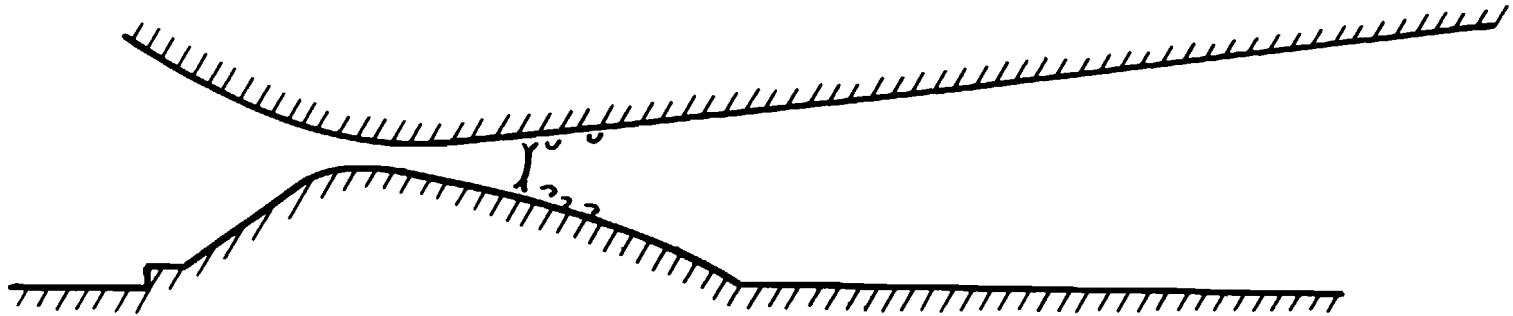
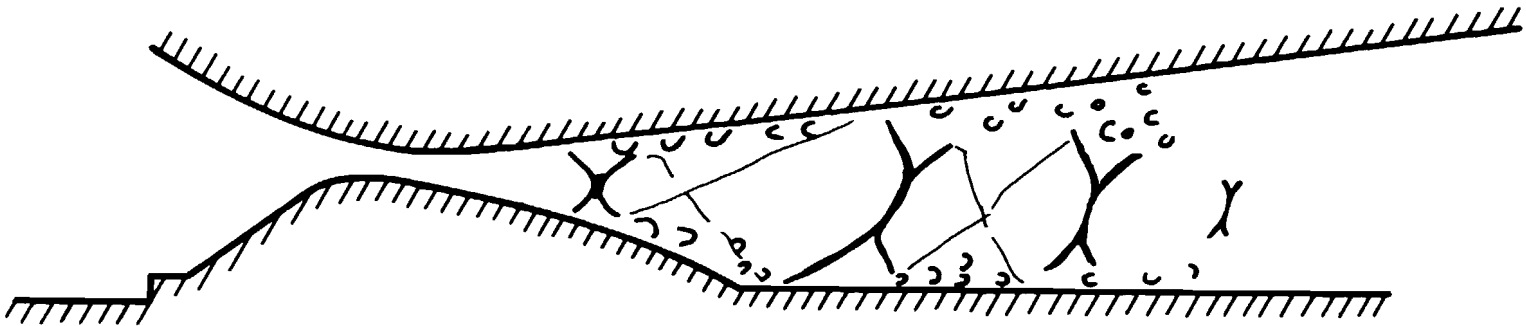


Fig. 16 Venturi Wall Static Pressure Distributions, $A_{on} = 110 \text{ in.}^2$, Open Screen Configuration



a. $W_{ac} = 160 \text{ lb}_m/\text{sec}$



b. $W_{ac} = 180 \text{ lb}_m/\text{sec}$

Fig. 17 Estimated Turbulence Generator Shock-Wave Systems, $A_{on} = 110 \text{ in.}^2$, Open Screen Configuration

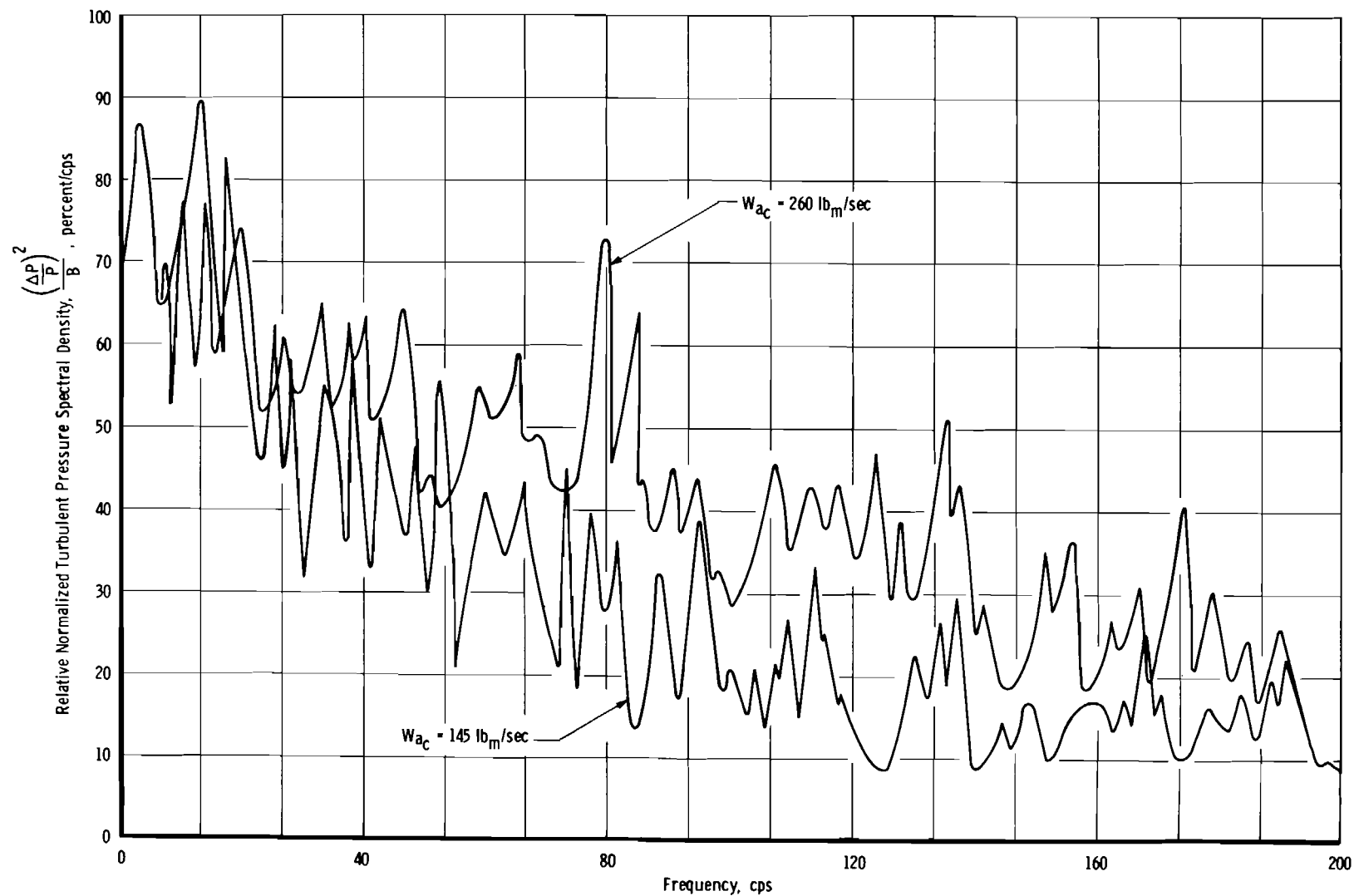


Fig. 18 Variance of the Normalized Turbulent Pressure Spectral Density with Corrected Airflow

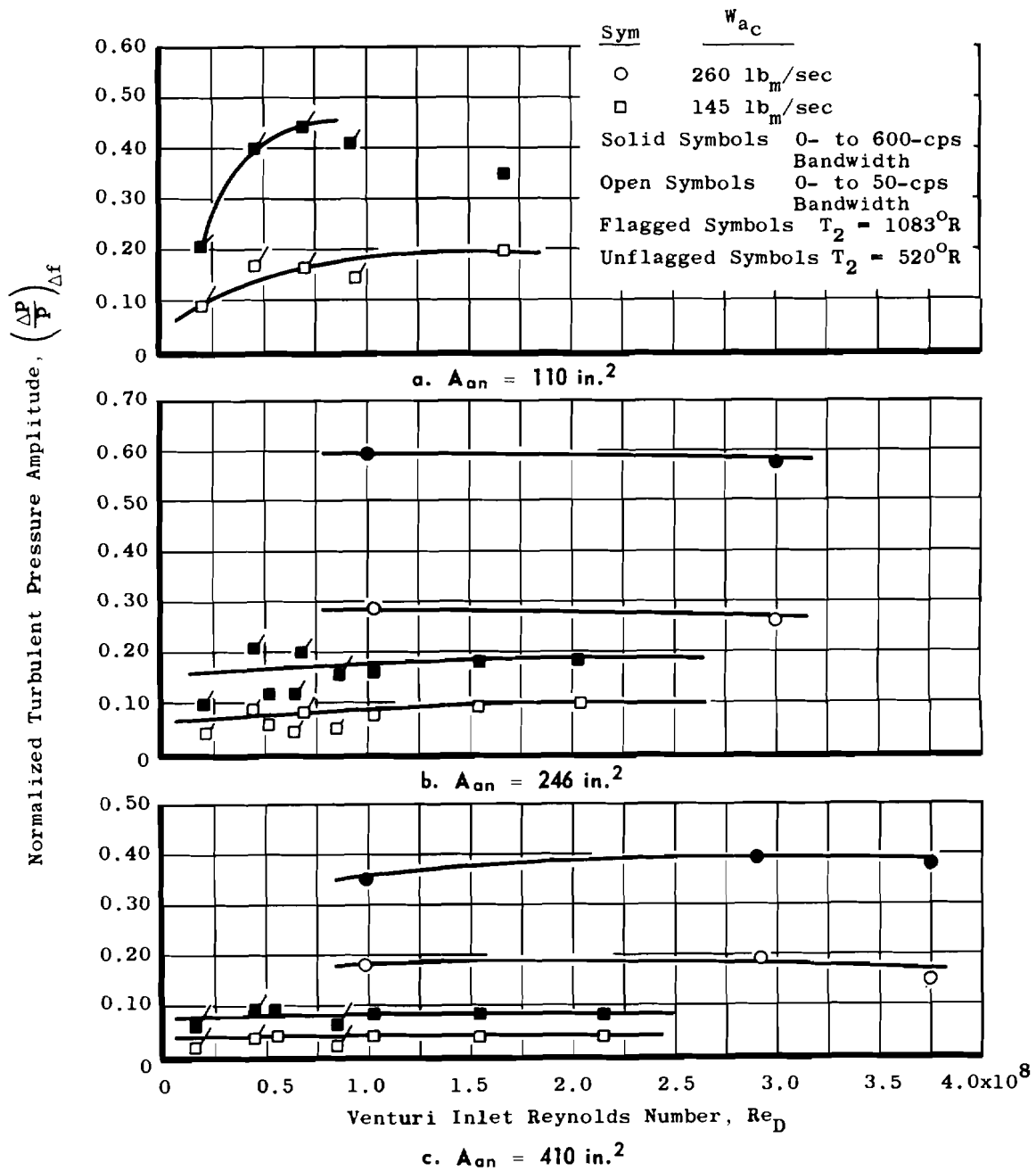
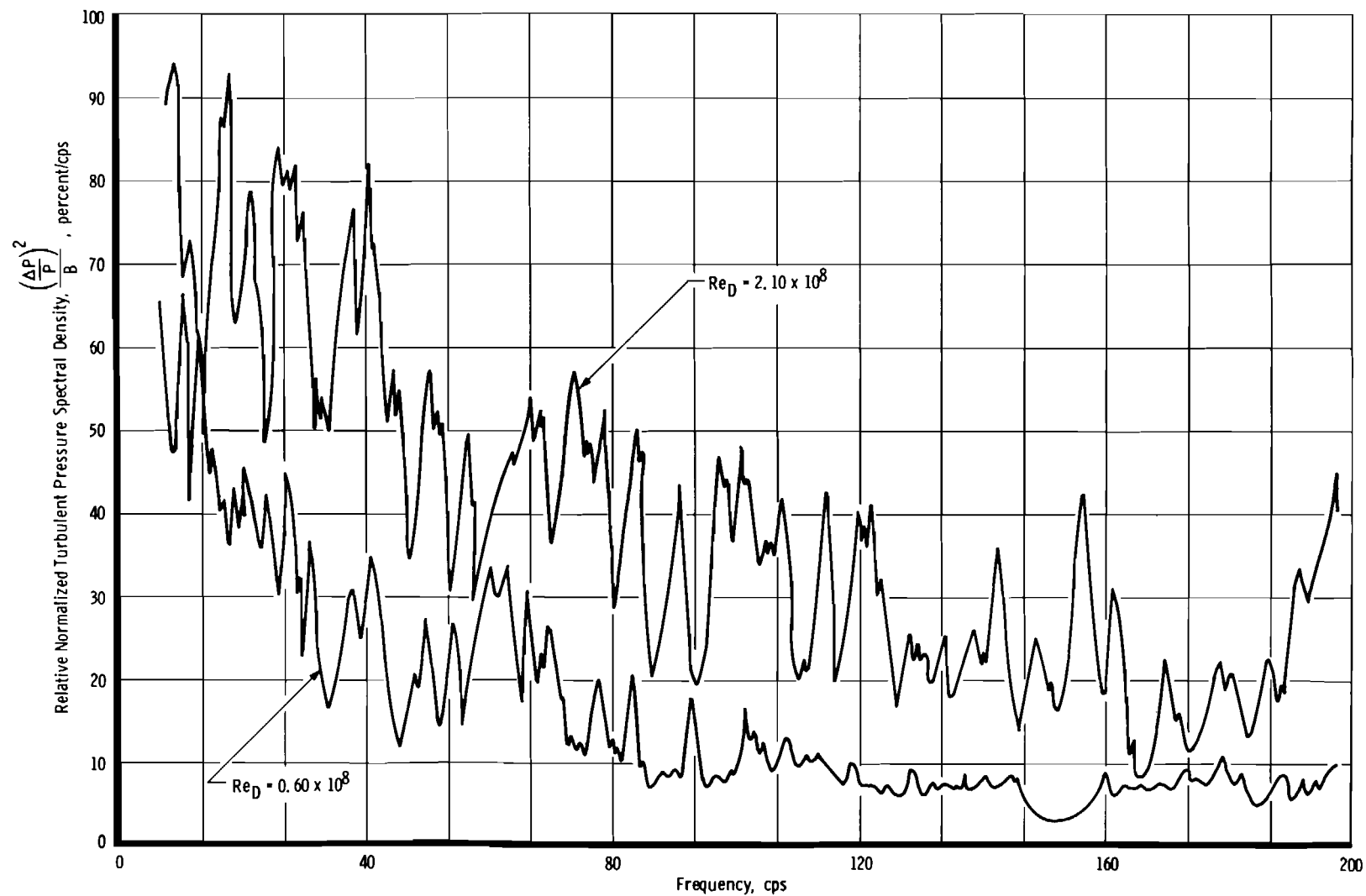
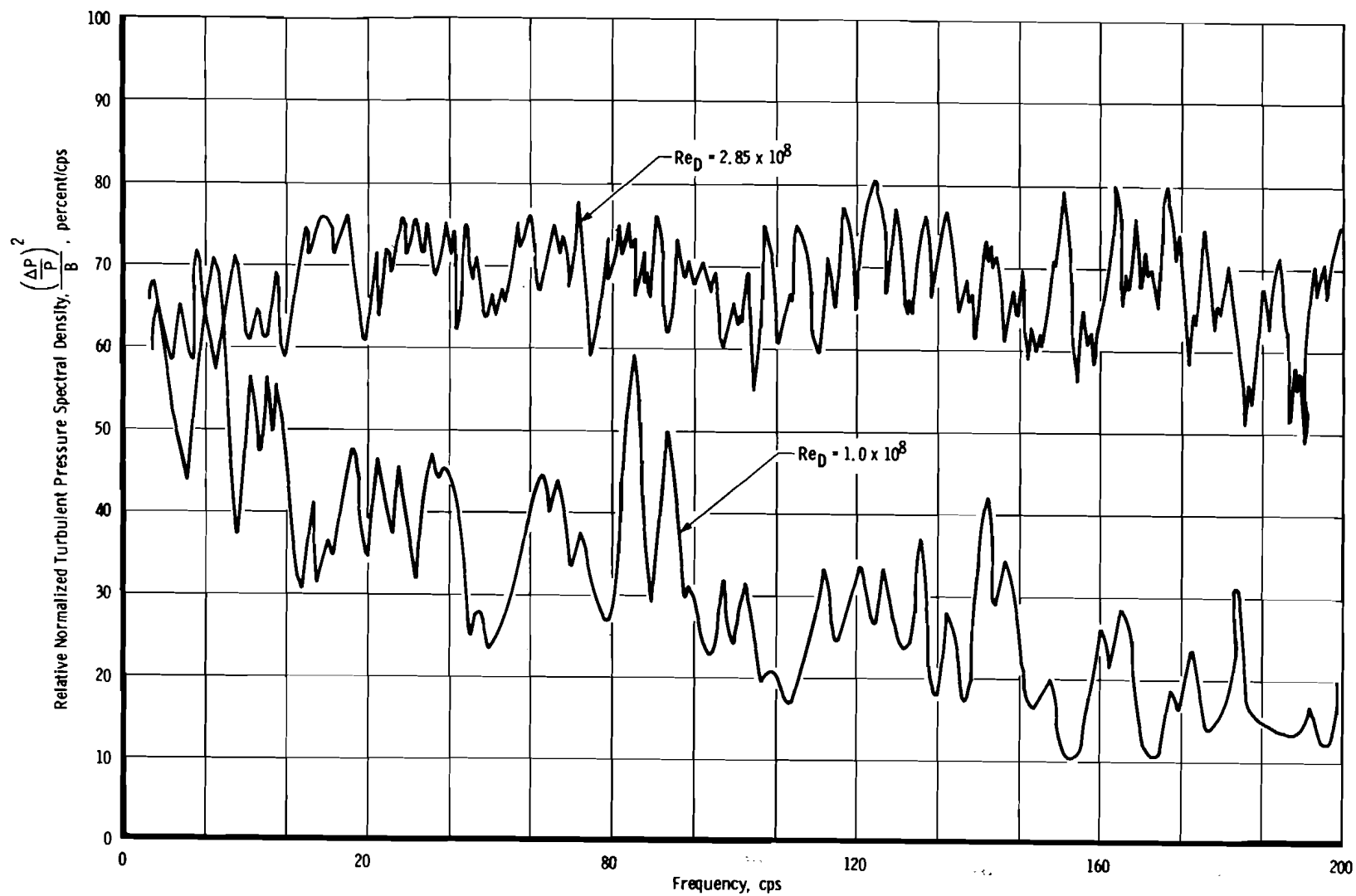


Fig. 19 Effect on Normalized Turbulent Pressure Amplitude of Reynolds Number



a. $W_{a_c} = 145 \text{ lb}_m/\text{sec}$

Fig. 20 Effect of Venturi Inlet Reynolds Number on the Normalized Turbulent Pressure Spectral Density



b. $W_{ac} = 260 \text{ lb}_m/\text{sec}$

Fig. 20 Concluded

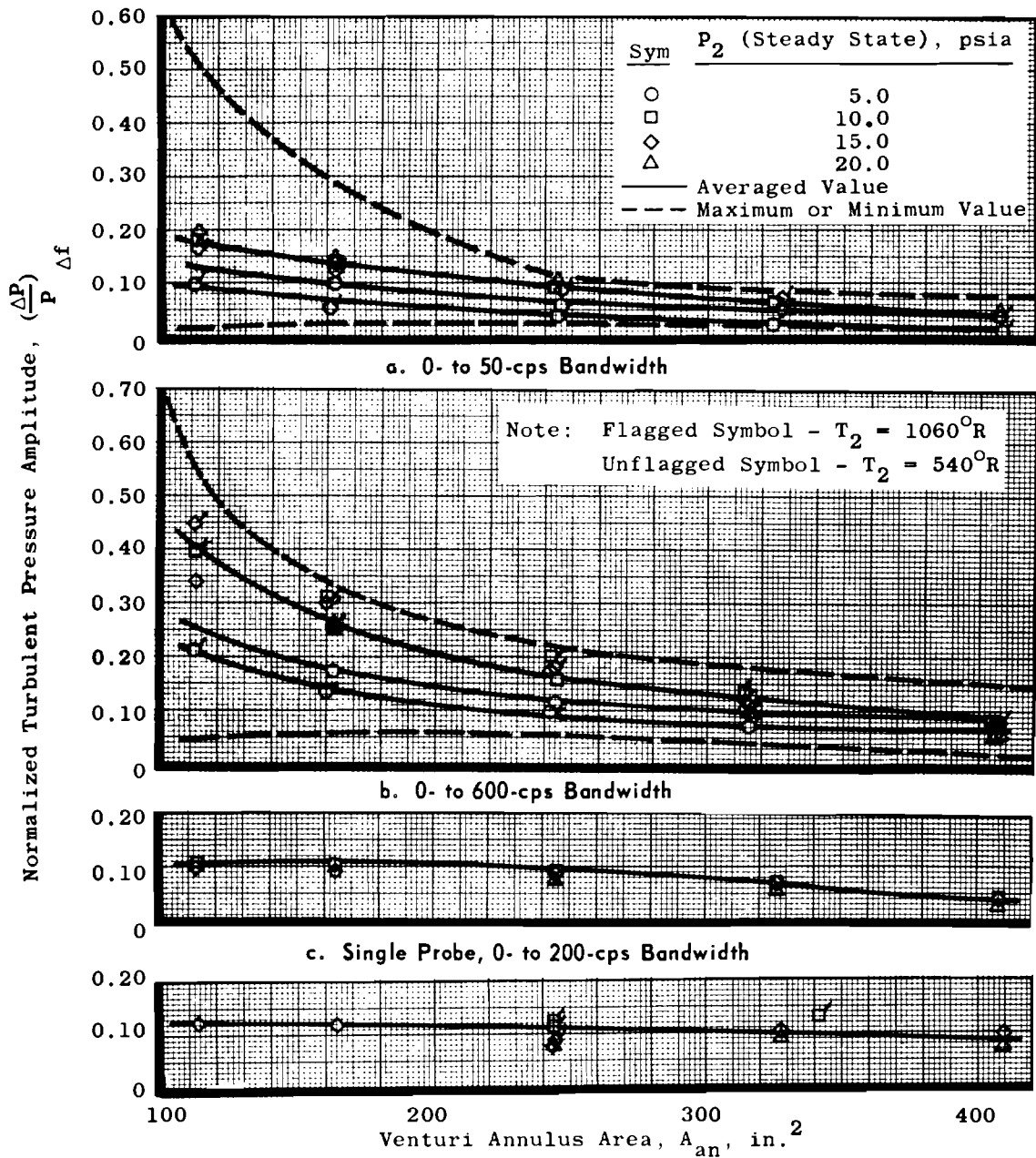


Fig. 21 Variance of Turbulence Amplitude with Annulus Area,
Open Screen Configuration, $W_{ac} = 145 \text{ lb}_m/\text{sec}$

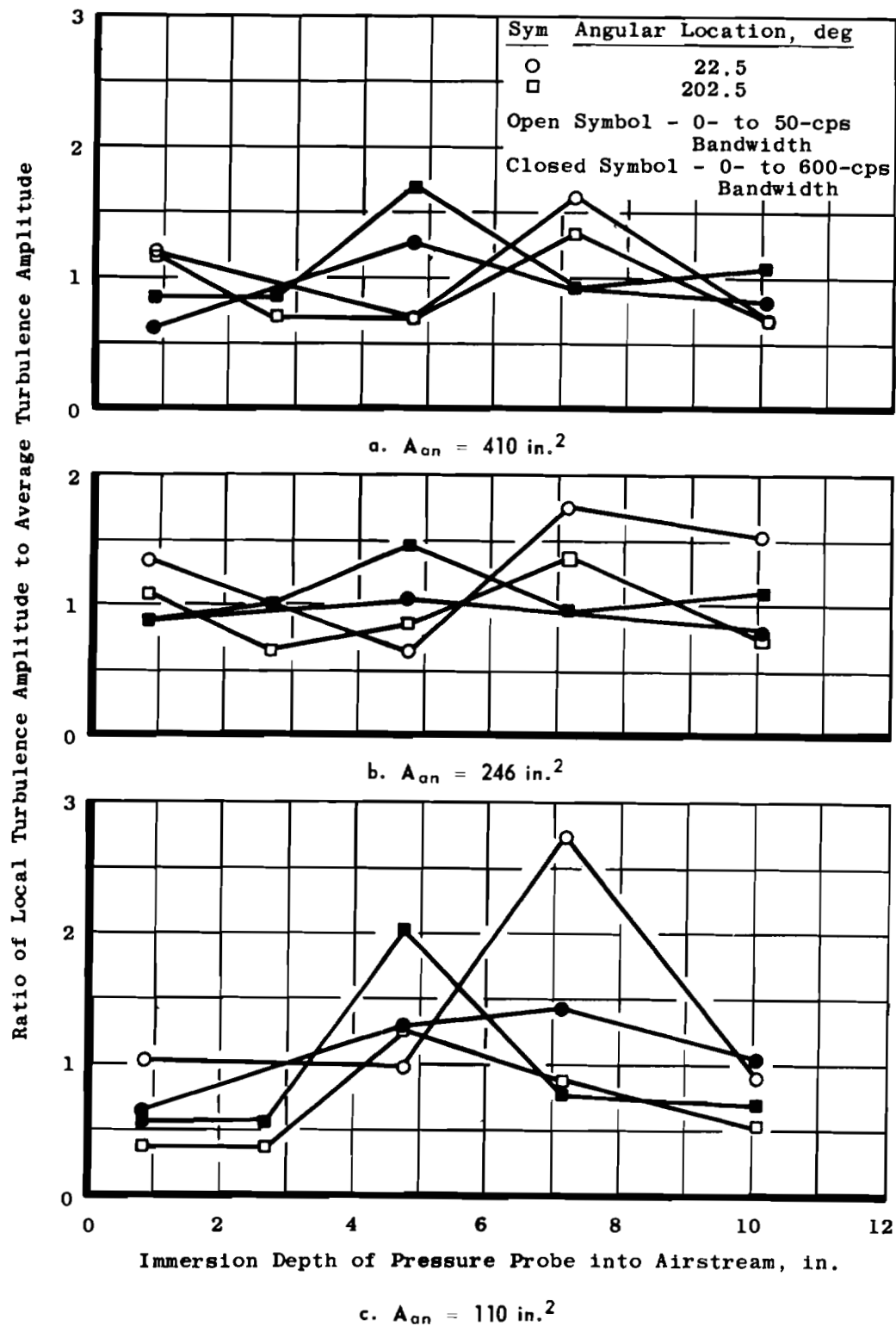


Fig. 22 Relative Turbulence Amplitude Radial Distribution,
 Open Screen Configuration, $W_{ac} = 145 \text{ lb}_m/\text{sec}$

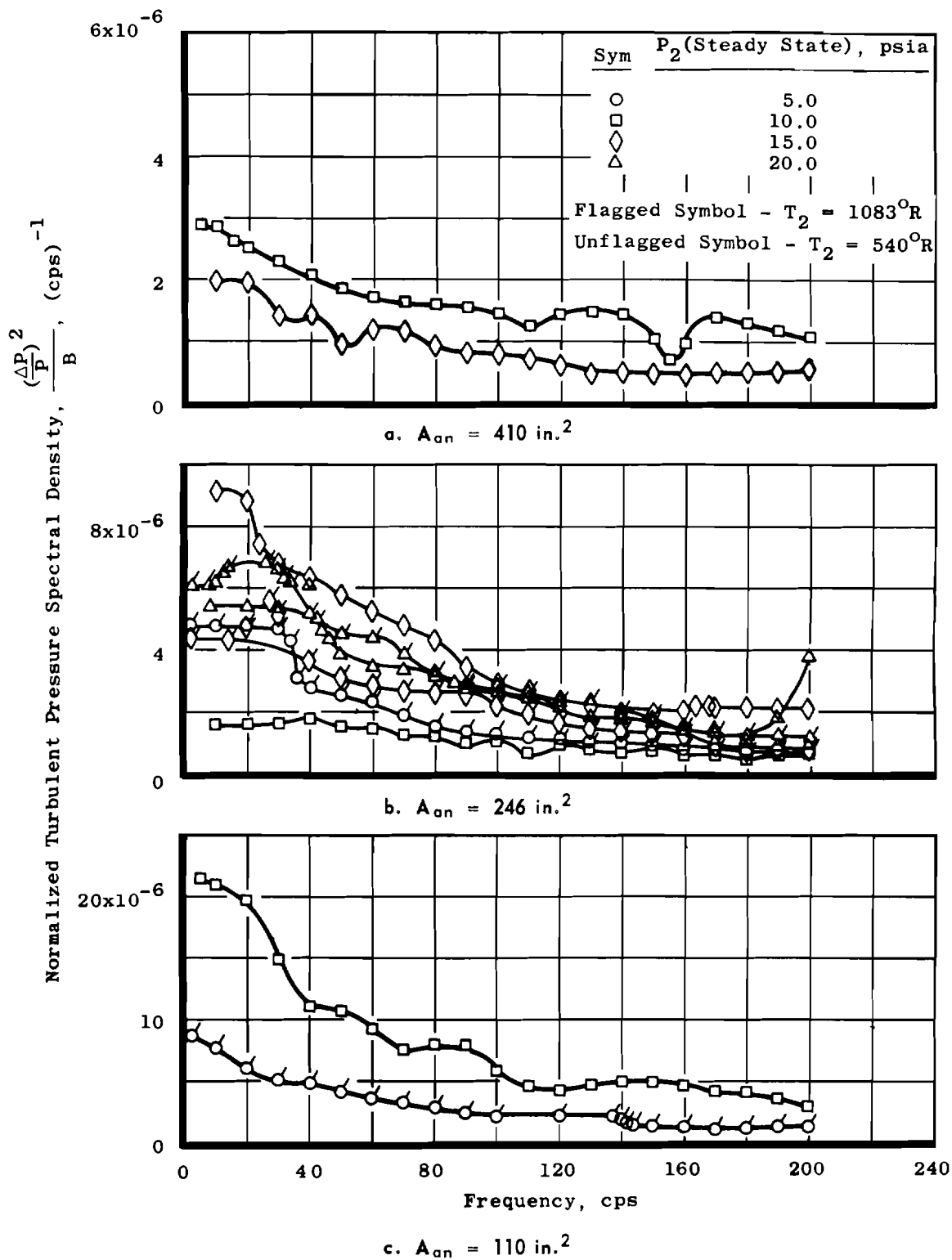
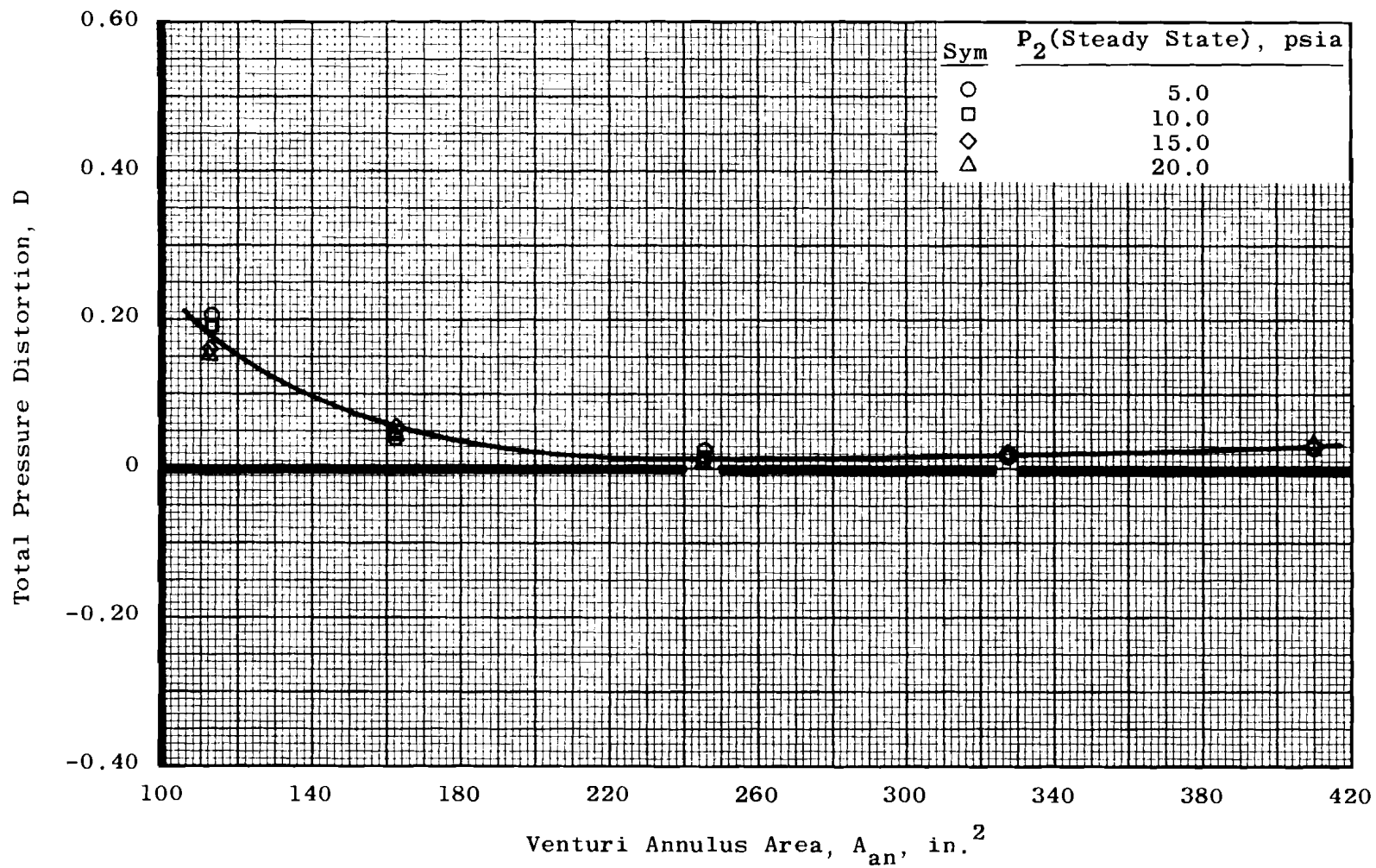
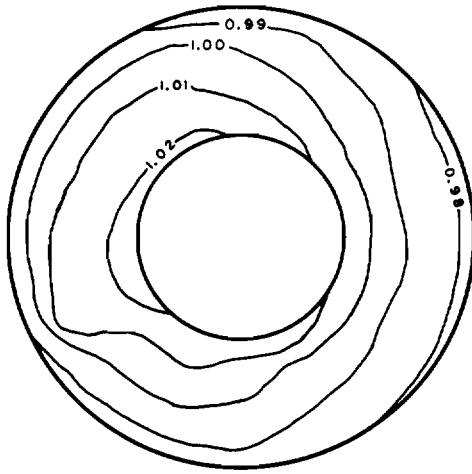


Fig. 23 Normalized Turbulent Pressure Spectral Density,
 Open Screen Configuration, $W_{ac} = 145 \text{ lb}_m/\text{sec}$

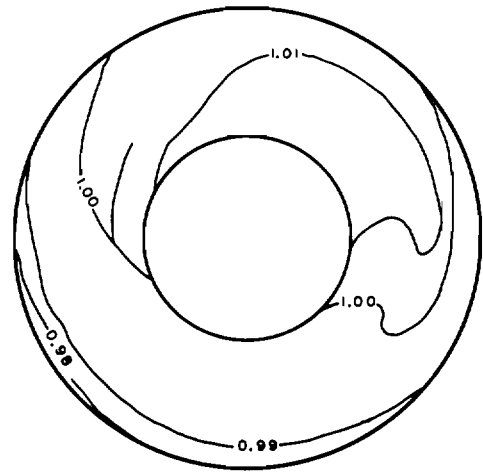


a. Variance with Annulus Area

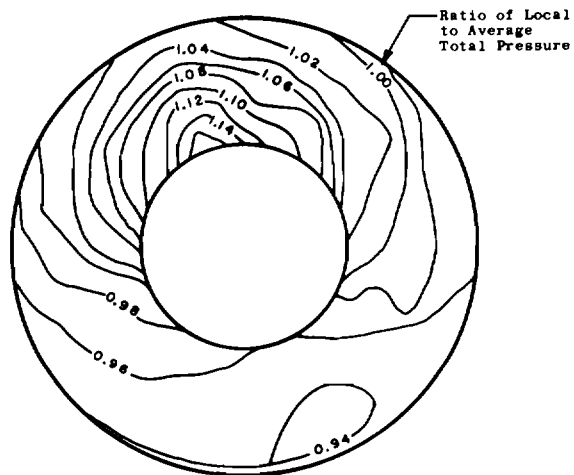
Fig. 24 Total Pressure Distortion Characteristics, Open Screen Configuration, $W_{ac} = 145 \text{ lb}_m/\text{sec}$



b. Distortion Pattern, $A_{an} = 410 \text{ in.}^2$



c. Distortion Pattern, $A_{an} = 246 \text{ in.}^2$



d. Distortion Pattern, $A_{an} = 110 \text{ in.}^2$

Fig. 24 Concluded

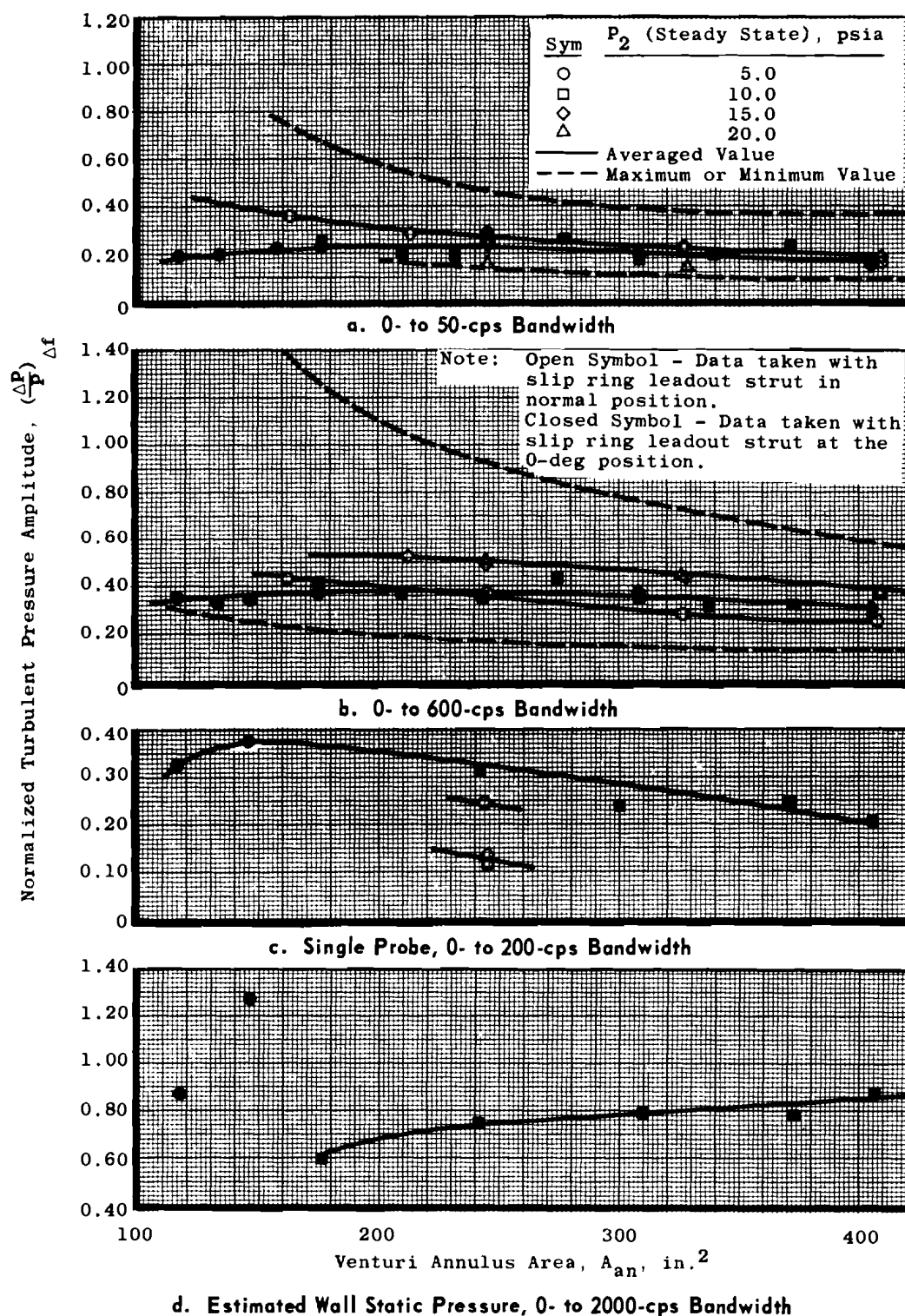


Fig. 25 Variance of Turbulence Amplitude with Annulus Area,
Open Screen Configuration, $W_{ac} = 260 \text{ lb}_m/\text{sec}$

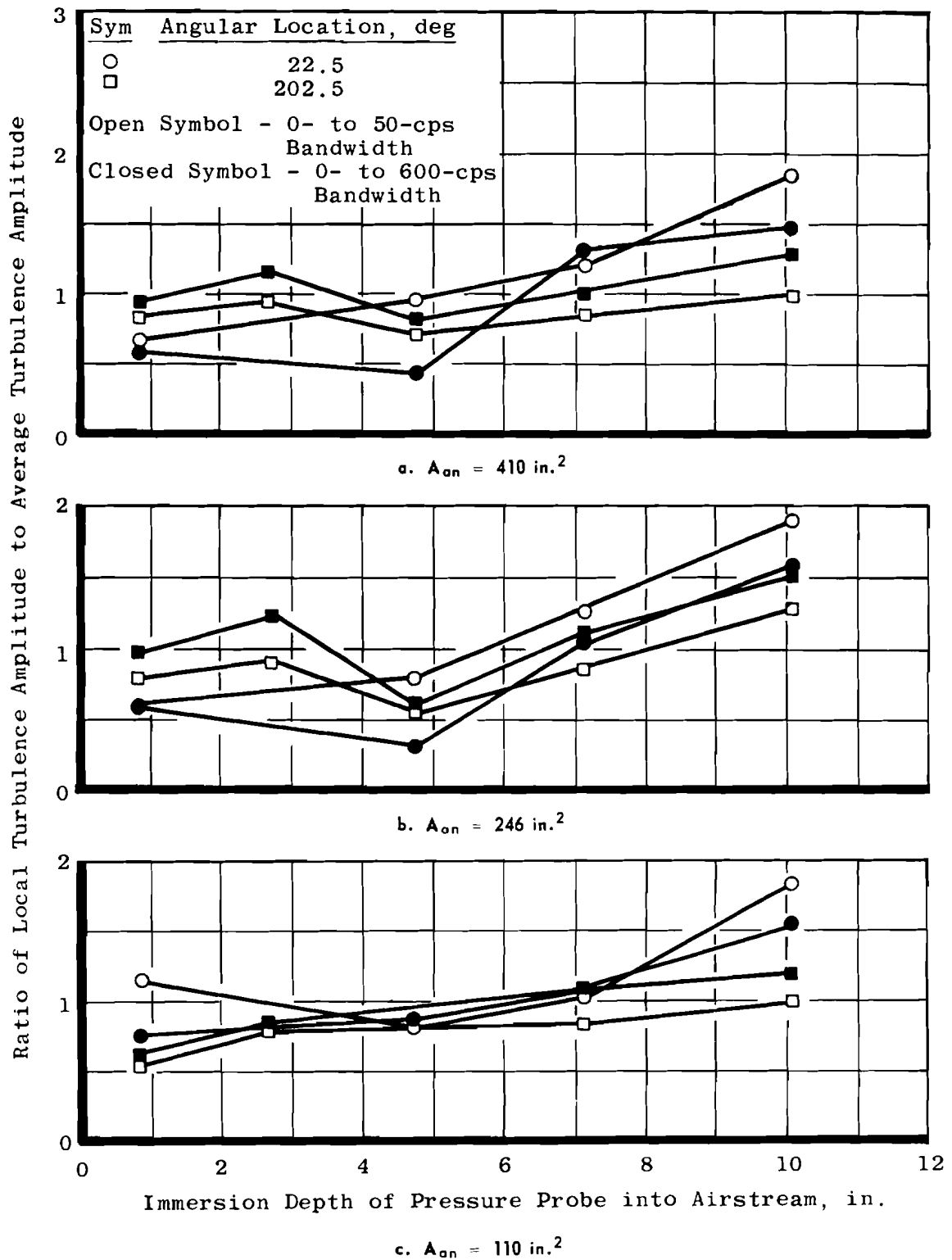


Fig. 26 Relative Turbulence Amplitude Radial Distribution,
Open Screen Configuration, $W_{ac} = 260 \text{ lb}_m/\text{sec}$

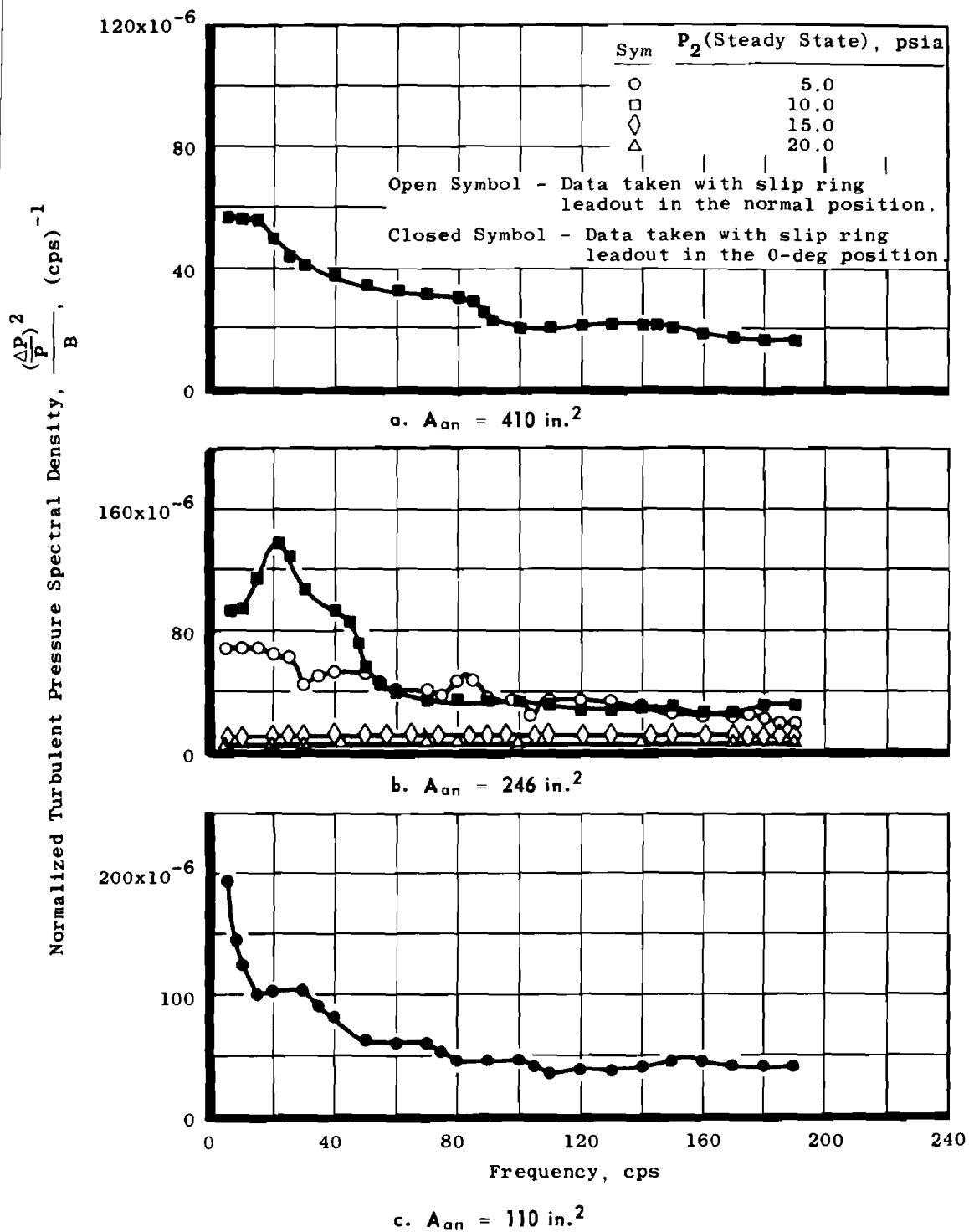
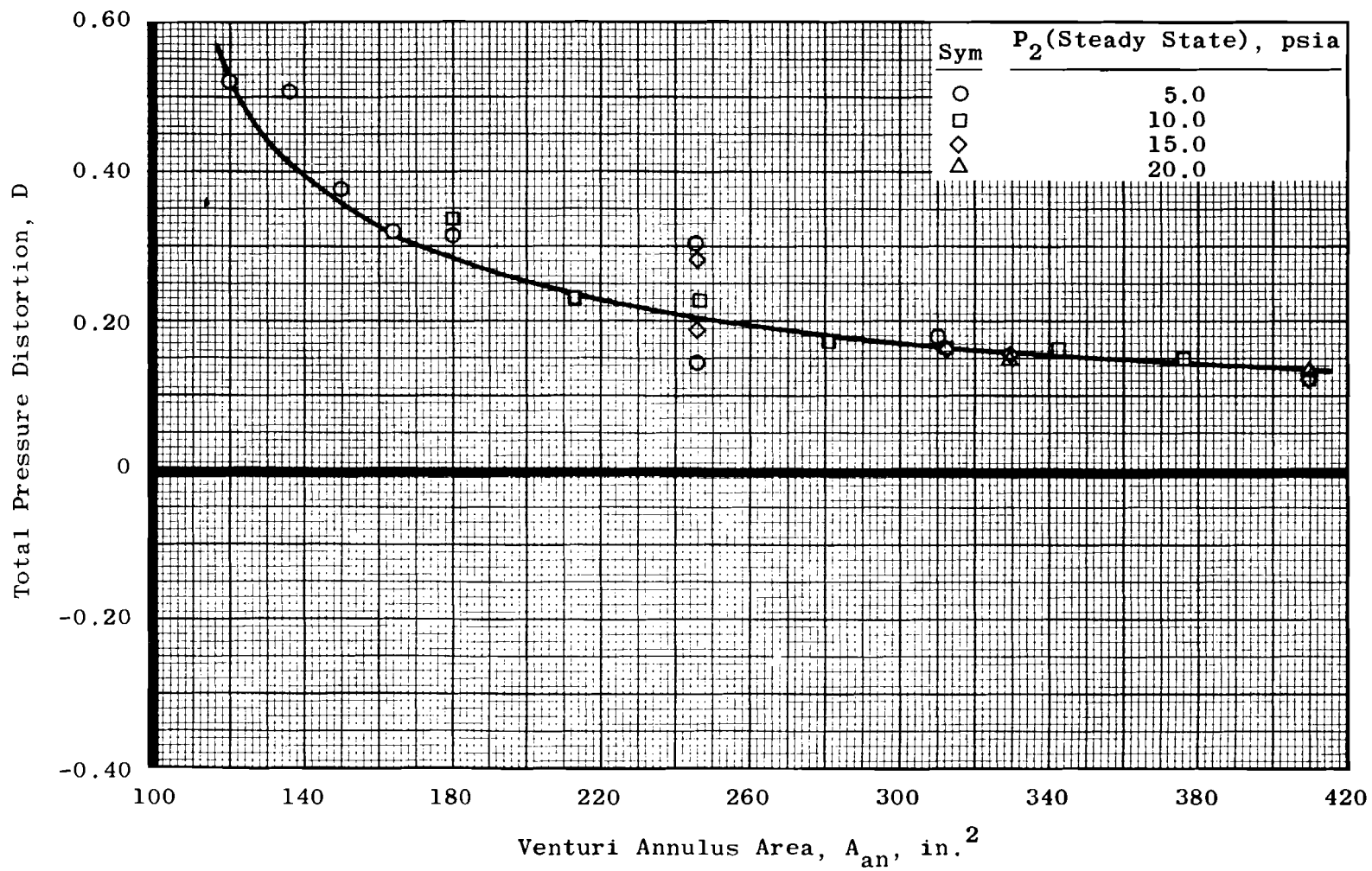
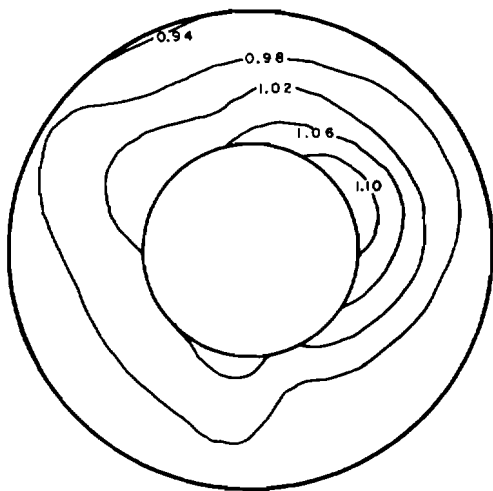


Fig. 27 Normalized Turbulent Pressure Spectral Density,
Open Screen Configuration, W_{ac} = 260 lb_m/sec

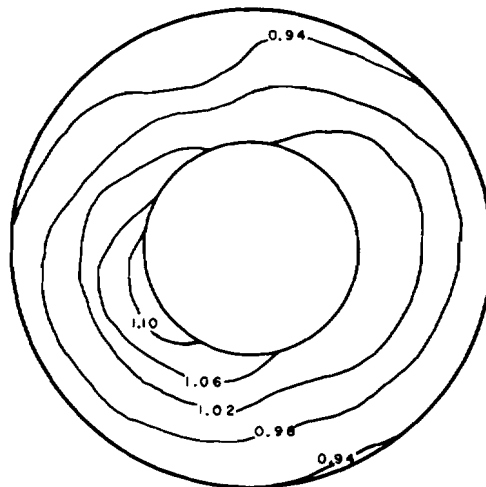


a. Variance with Annulus Area

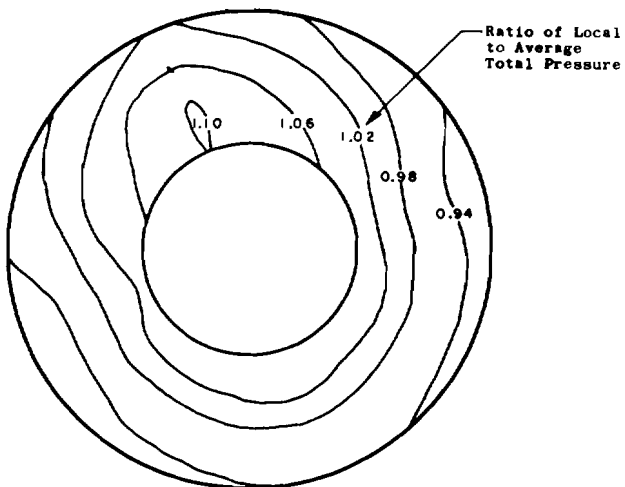
Fig. 28 Total Pressure Distortion Characteristics, Open Screen Configuration, $W_{ac} = 260 \text{ lb}_m/\text{sec}$



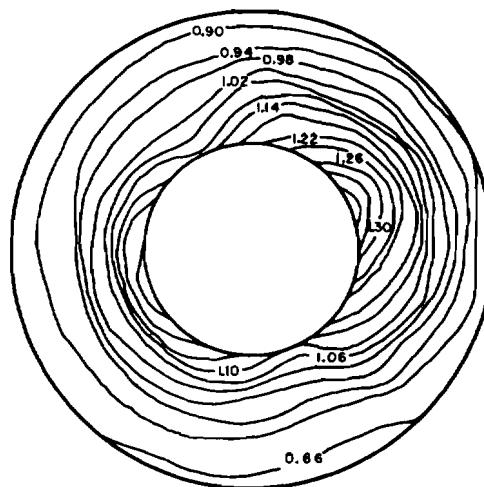
b. Distortion Pattern, $A_{an} = 410 \text{ in.}^2$
(Slip Ring Leadout Strut at Normal
Position)



c. Distortion Pattern, $A_{an} = 246 \text{ in.}^2$
(Slip Ring Leadout Strut at 0-deg
Position)



d. Distortion Pattern, $A_{an} = 246 \text{ in.}^2$
(Slip Ring Leadout Strut at Normal
Position)



e. Distortion Pattern, $A_{an} = 110 \text{ in.}^2$
(Slip Ring Leadout Strut at 0-deg
Position)

Fig. 28 Concluded

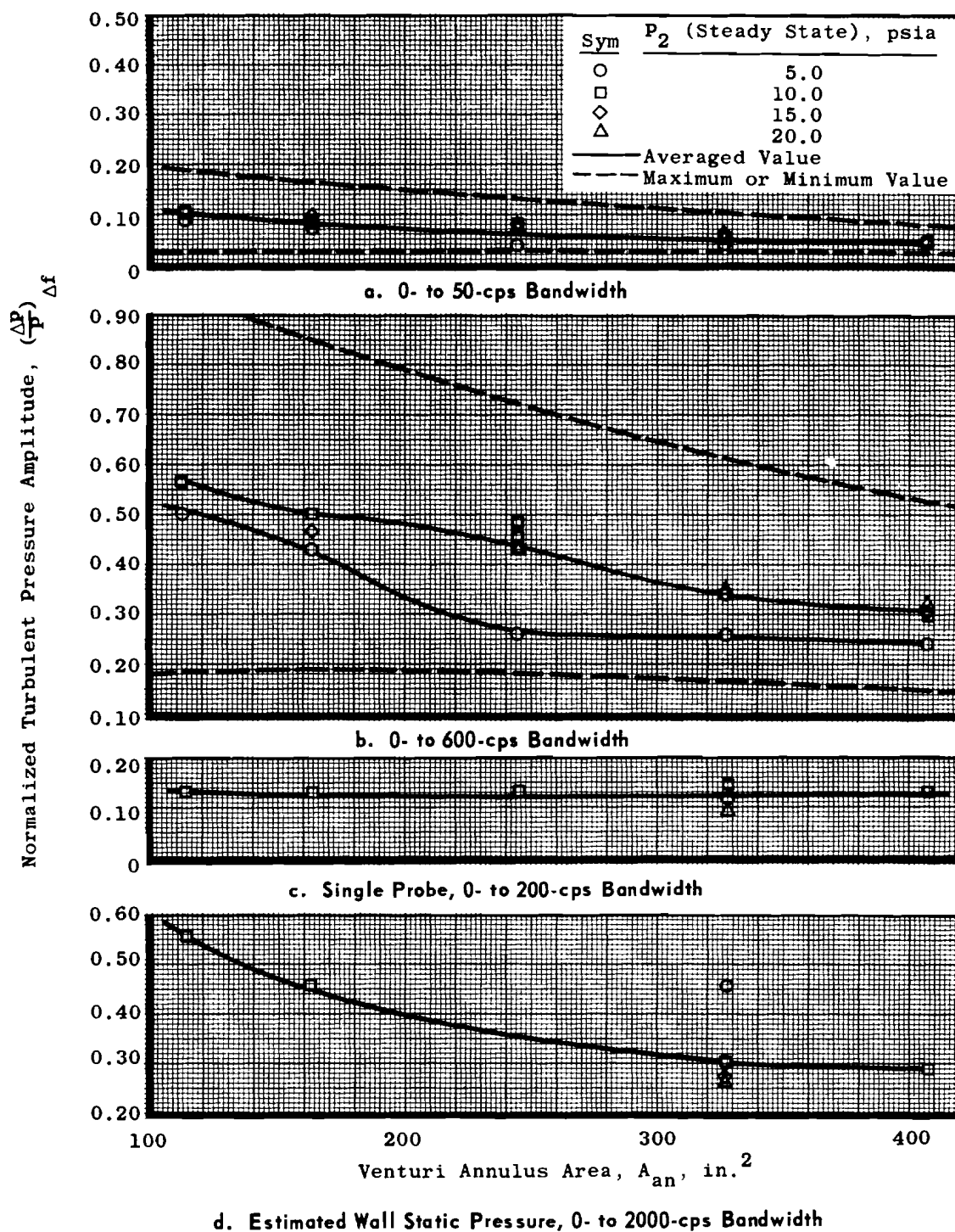


Fig. 29 Variance of Turbulence Amplitude with Annulus Area,
Light Blockage Screen Configuration, $W_{oc} = 260 \text{ lb}_m/\text{sec}$

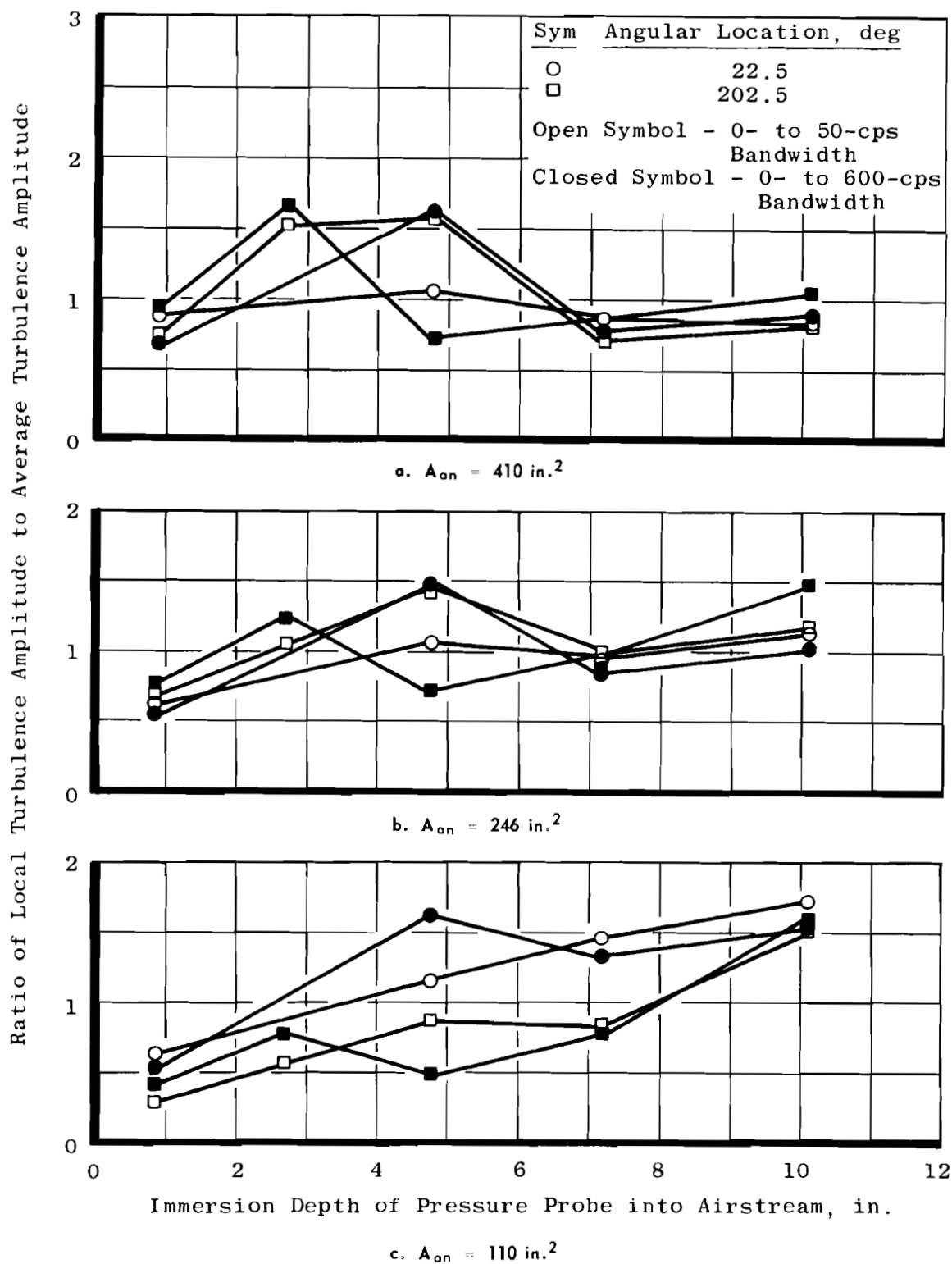


Fig. 30 Relative Turbulence Amplitude Radial Distribution,
Light Blockage Screen Configuration, $W_{ac} = 260 \text{ lb}_m/\text{sec}$

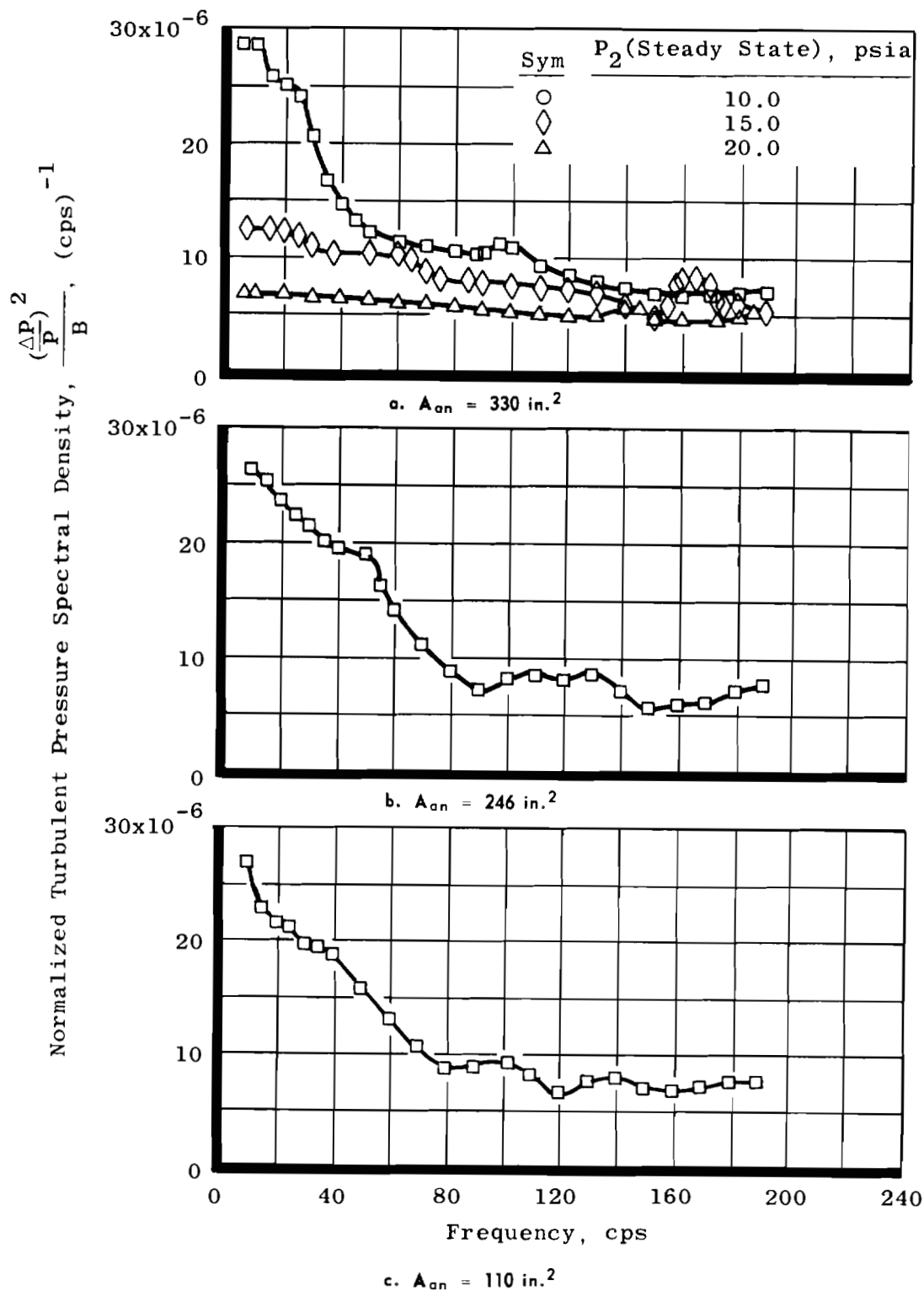
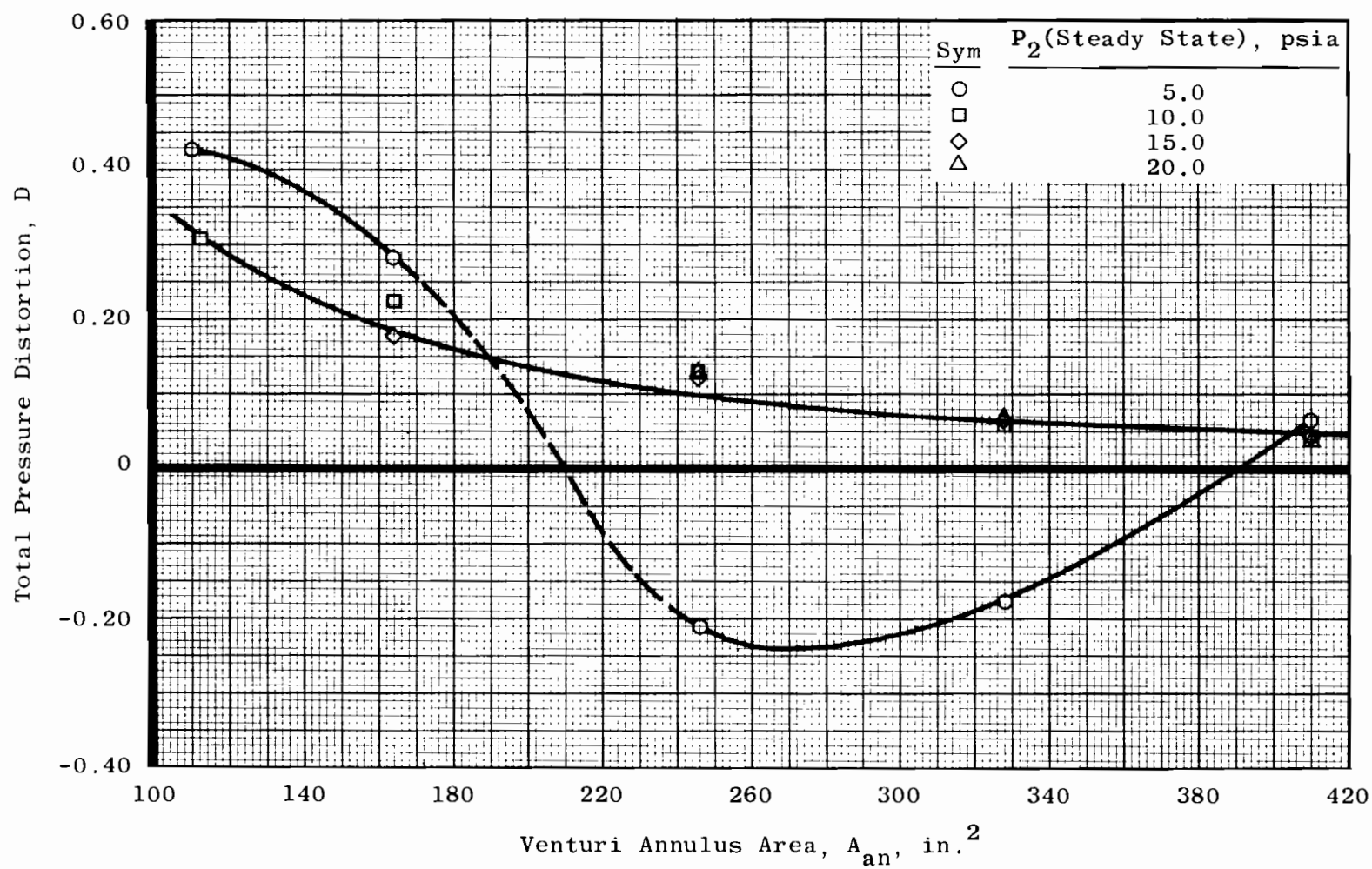
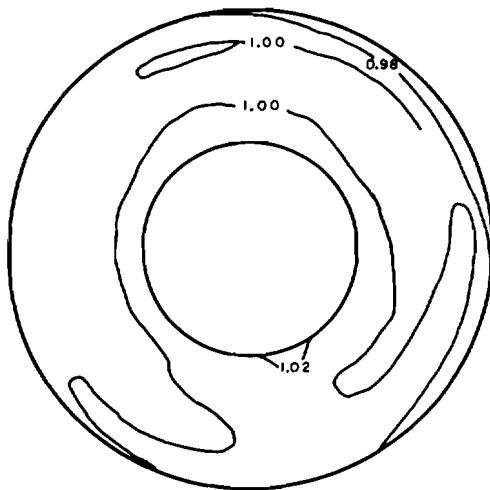


Fig. 31 Normalized Turbulent Pressure, Spectral Density Light Blockage
Screen Configuration, $W_{ac} = 260 \text{ lb}_m/\text{sec}$

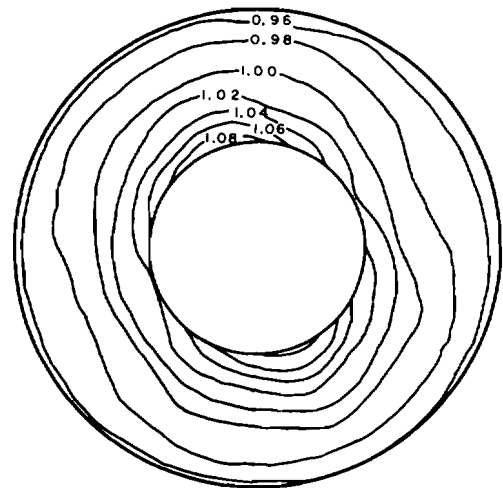


a. Variance with Annulus Area

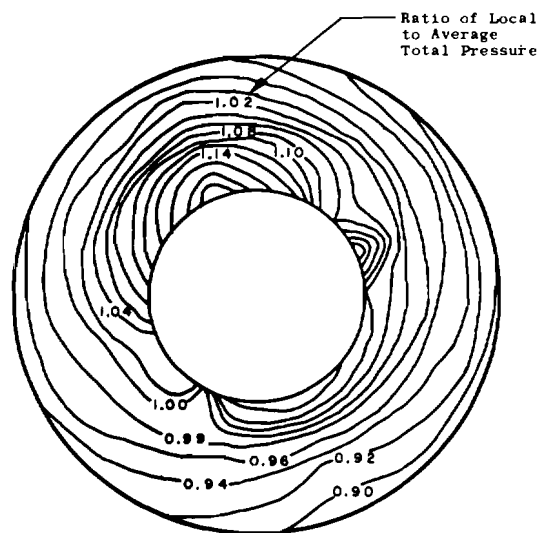
Fig. 32 Total Pressure Distortion Characteristics, Light Blockage Screen Configuration, $W_{ac} = 260 \text{ lb}_m/\text{sec}$



b. Distortion Pattern, $A_{an} = 410 \text{ in.}^2$



c. Distortion Pattern, $A_{an} = 246 \text{ in.}^2$



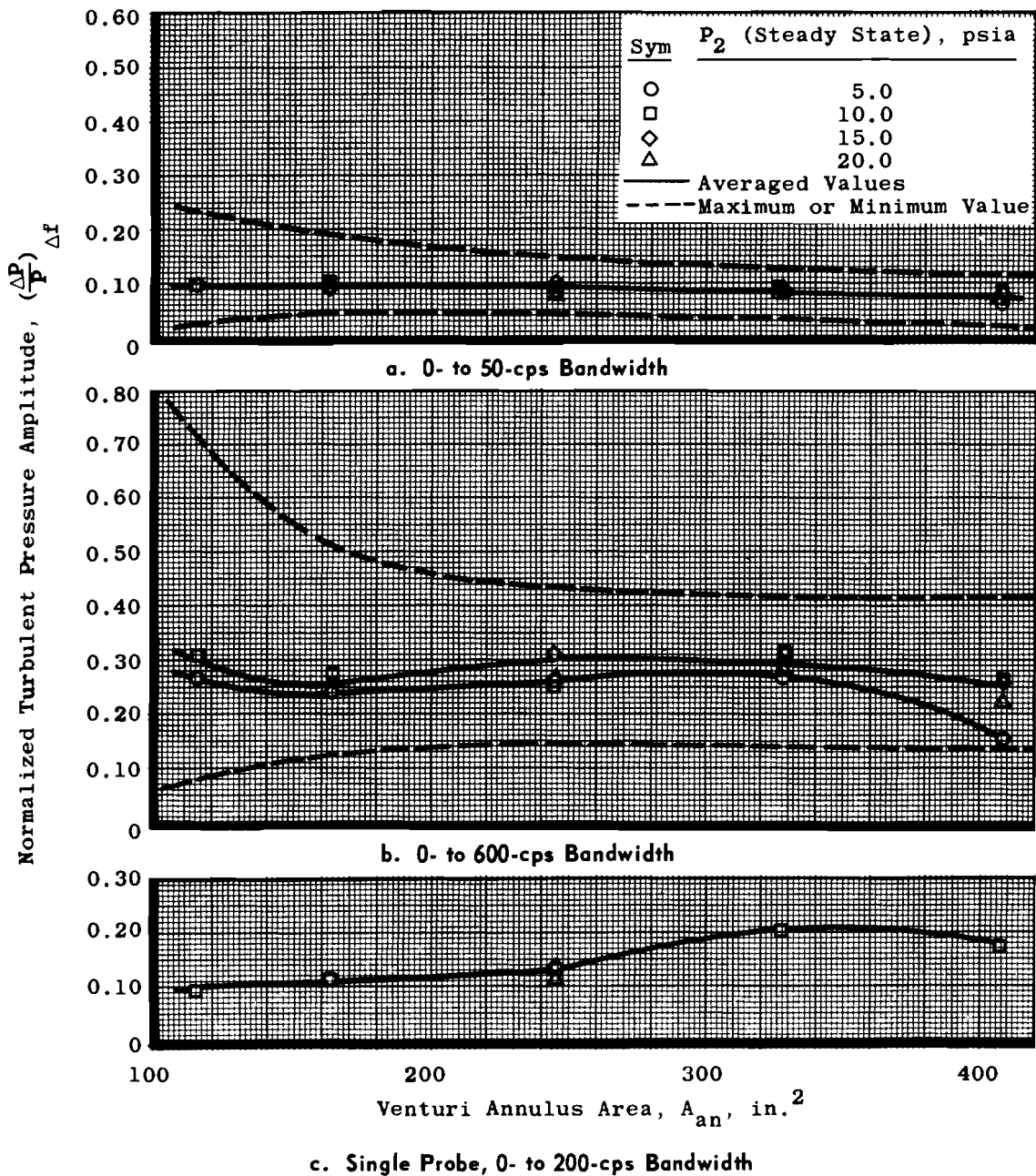


Fig. 33 Variance of Turbulence Amplitude with Annulus Area,
Intermediate Blockage Screen Configuration,
 $W_{ac} = 260 \text{ lb}_m/\text{sec}$

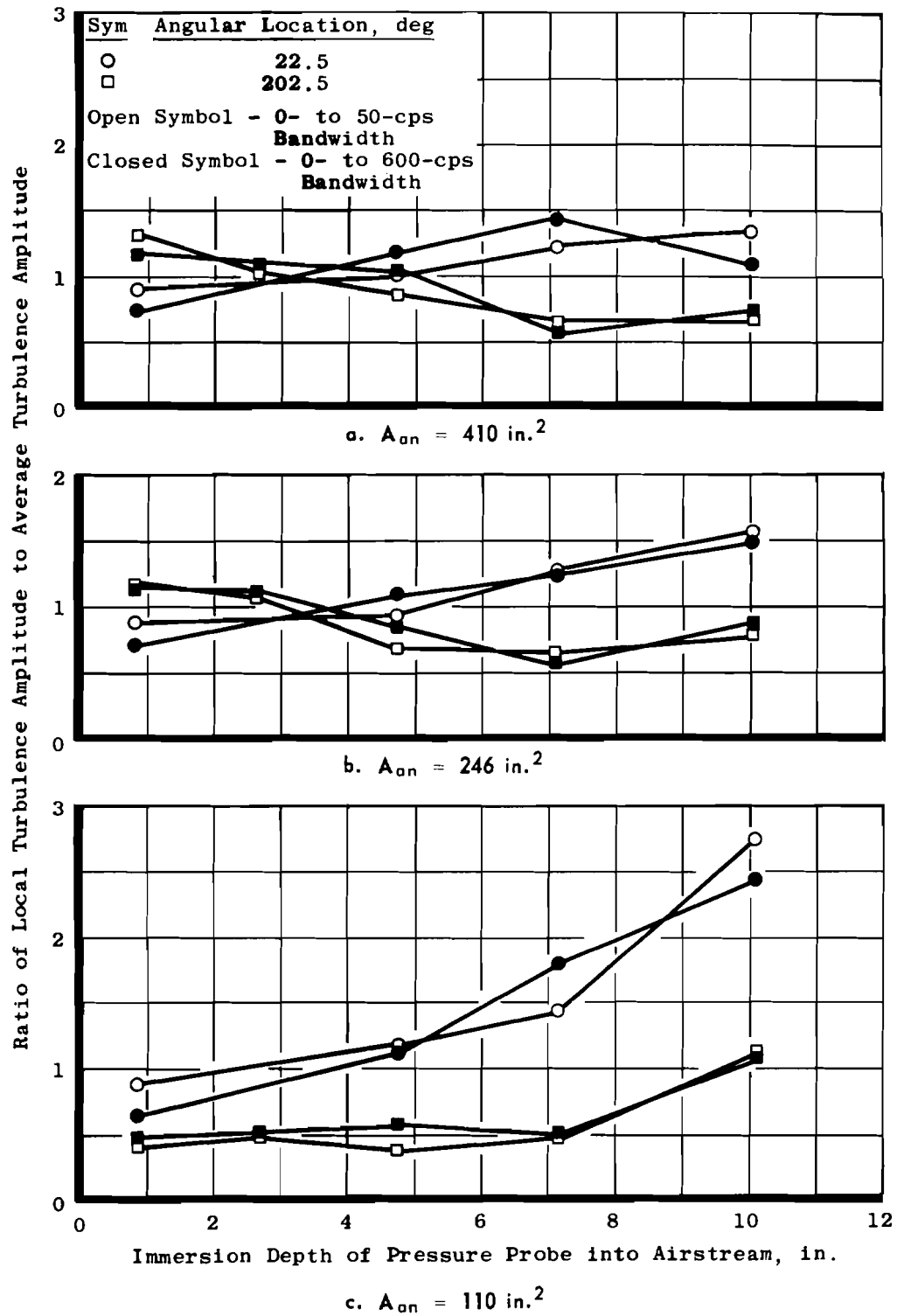


Fig. 34 Relative Turbulence Amplitude Radial Distribution,
Intermediate Blockage Screen Configuration,
 $W_{ac} = 260 \text{ lb}_m/\text{sec}$

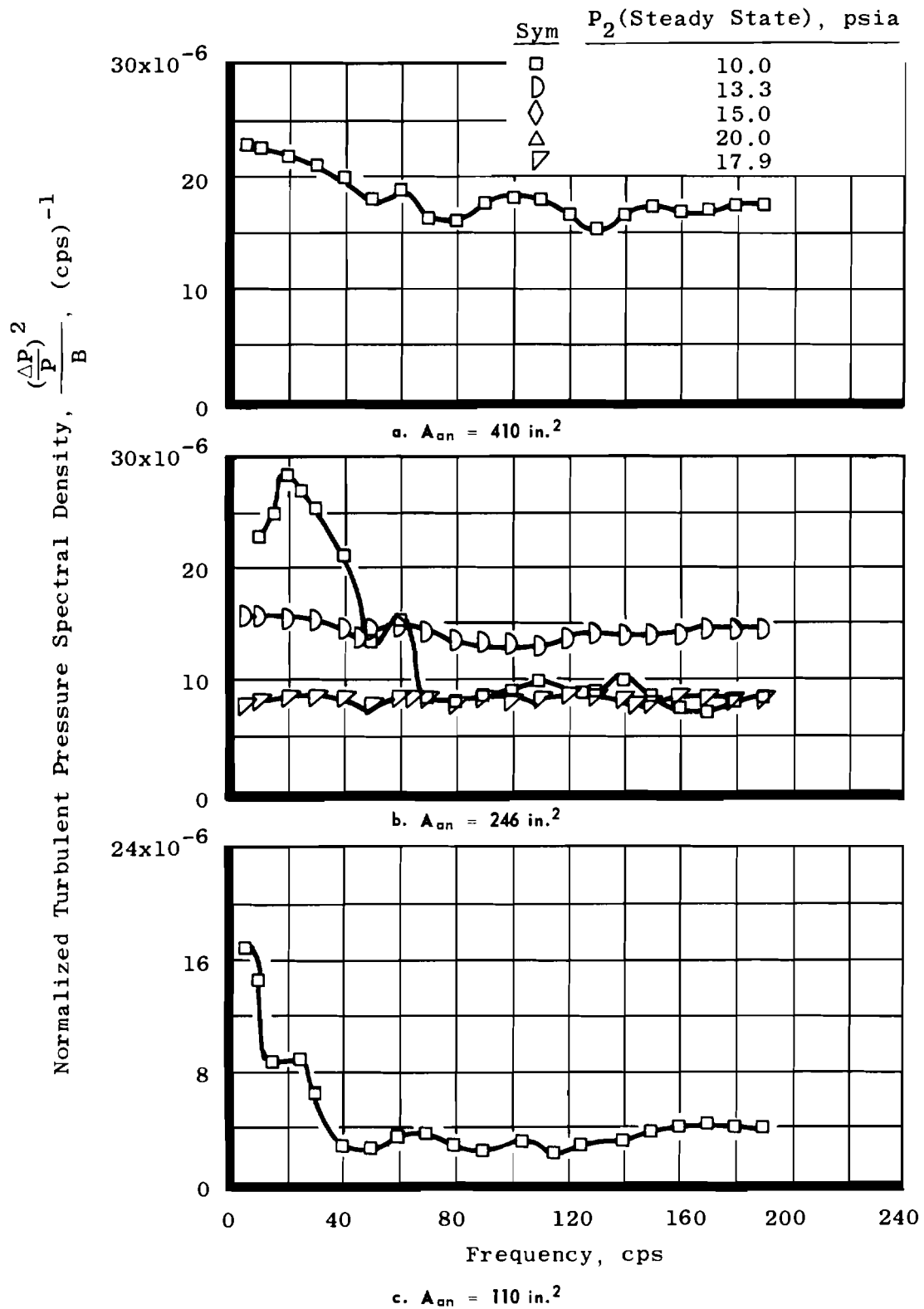
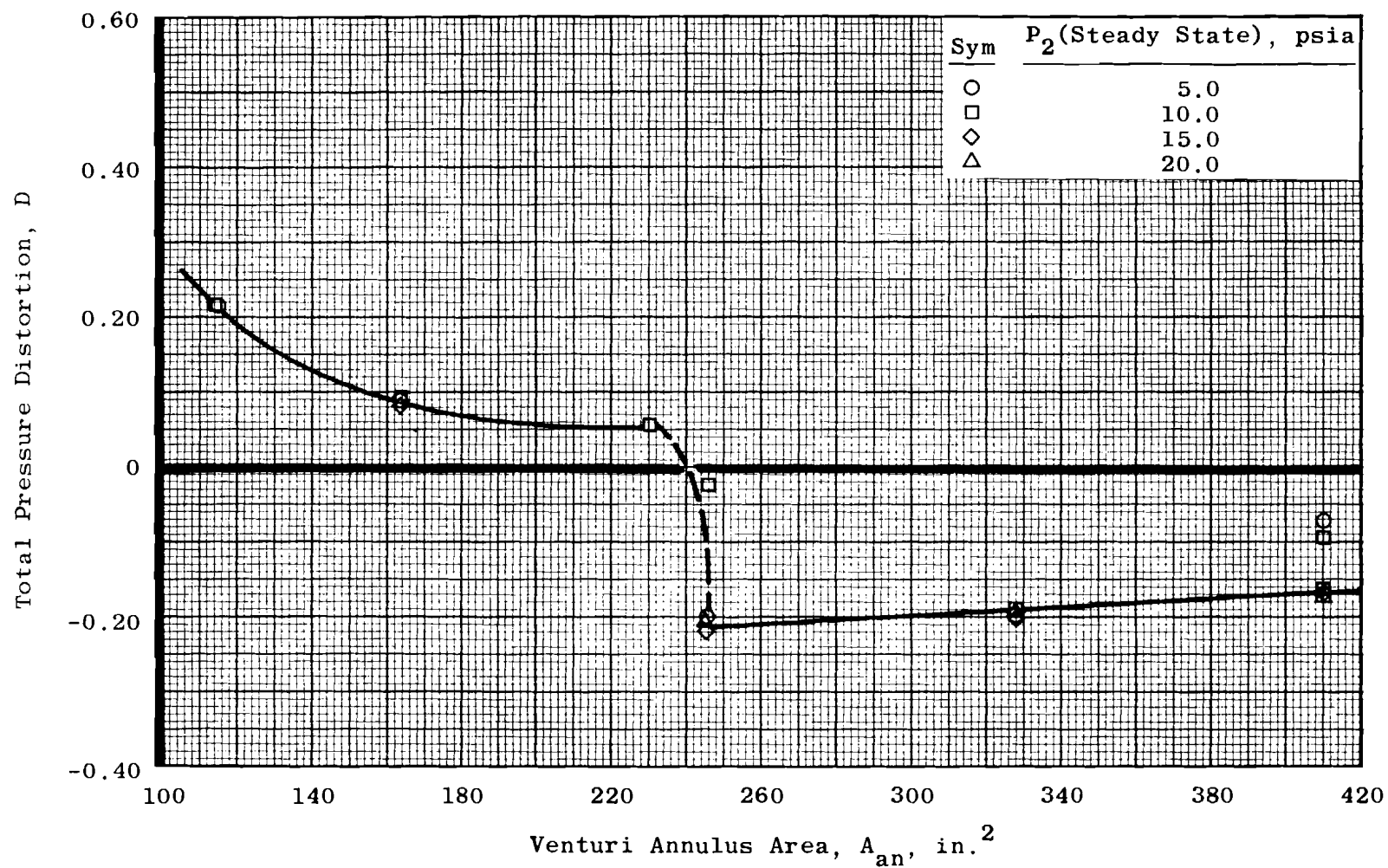
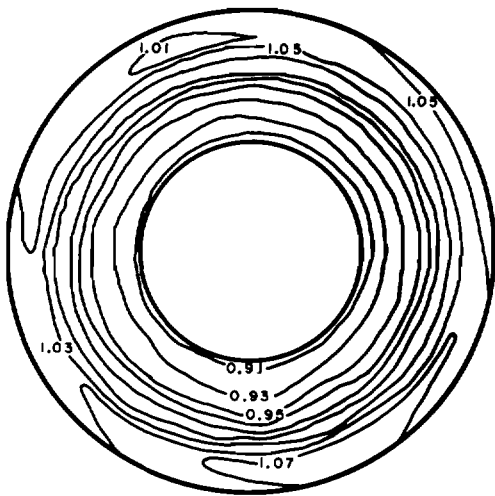


Fig. 35 Normalized Turbulent Pressure Spectral Density,
Intermediate Blockage Screen Configuration,
 $W_{oc} = 260 \text{ lb}_m/\text{sec}$

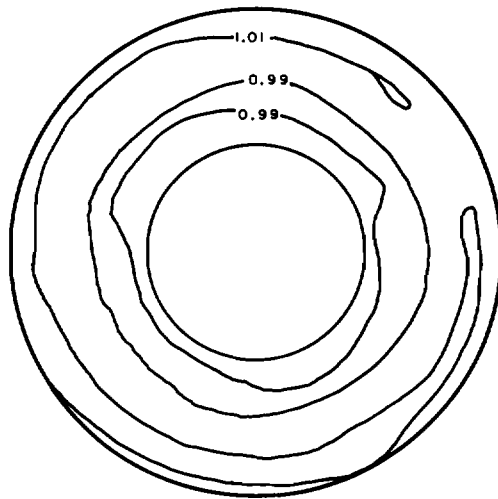


a. Variance with Annulus Area

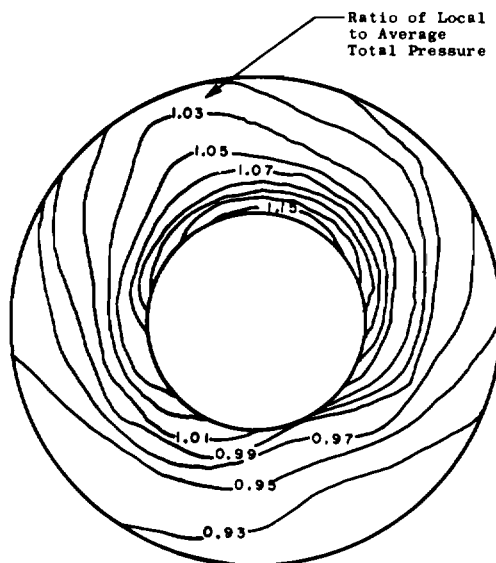
Fig. 36 Total Pressure Distortion Characteristics, Intermediate Blockage Screen Configuration, $W_{ac} = 260 \text{ lb}_m/\text{sec}$



b. Distortion Pattern, $A_{an} = 410 \text{ in.}^2$



c. Distortion Pattern, $A_{an} = 246 \text{ in.}^2$



d. Distortion Pattern, $A_{an} = 110 \text{ in.}^2$

Fig. 36 Concluded

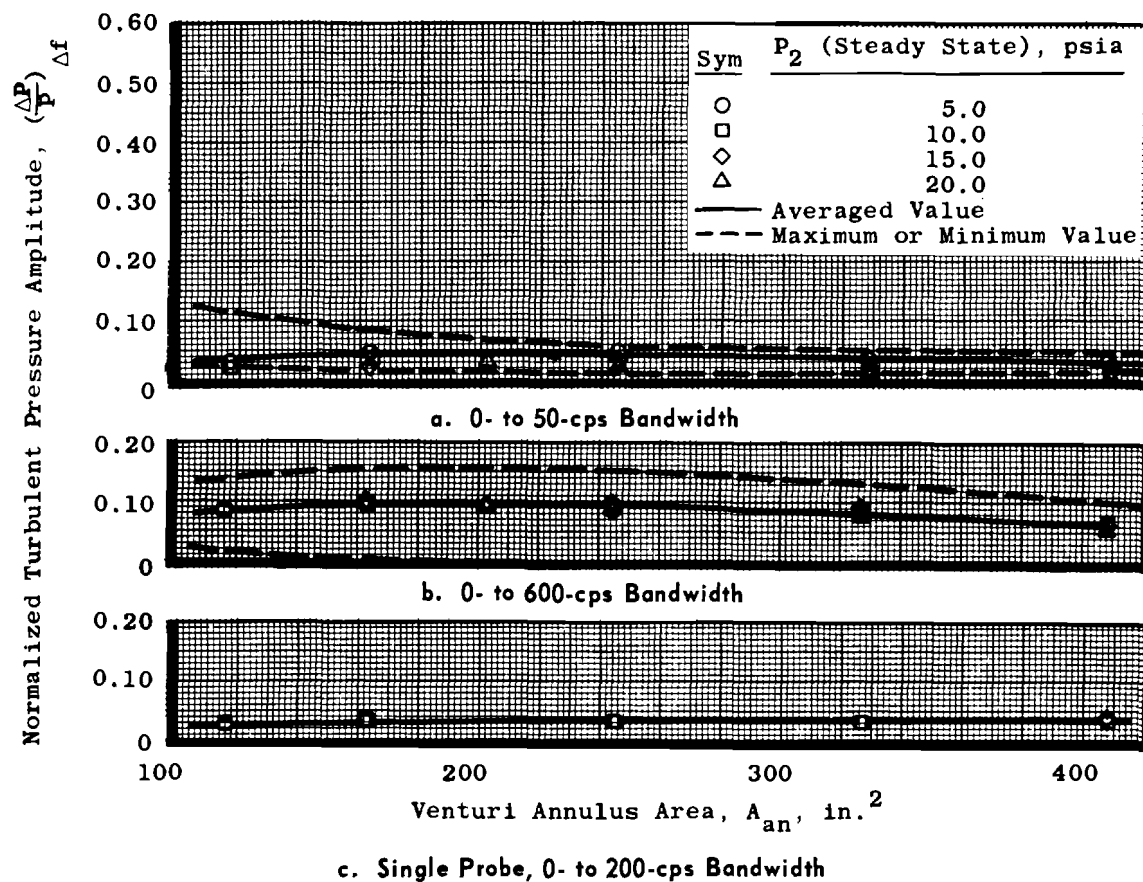


Fig. 37 Variance of Turbulence Amplitude with Annulus Area,
Heavy Blockage Screen Configuration, $W_{ac} = 260 \text{ lb}_m/\text{sec}$

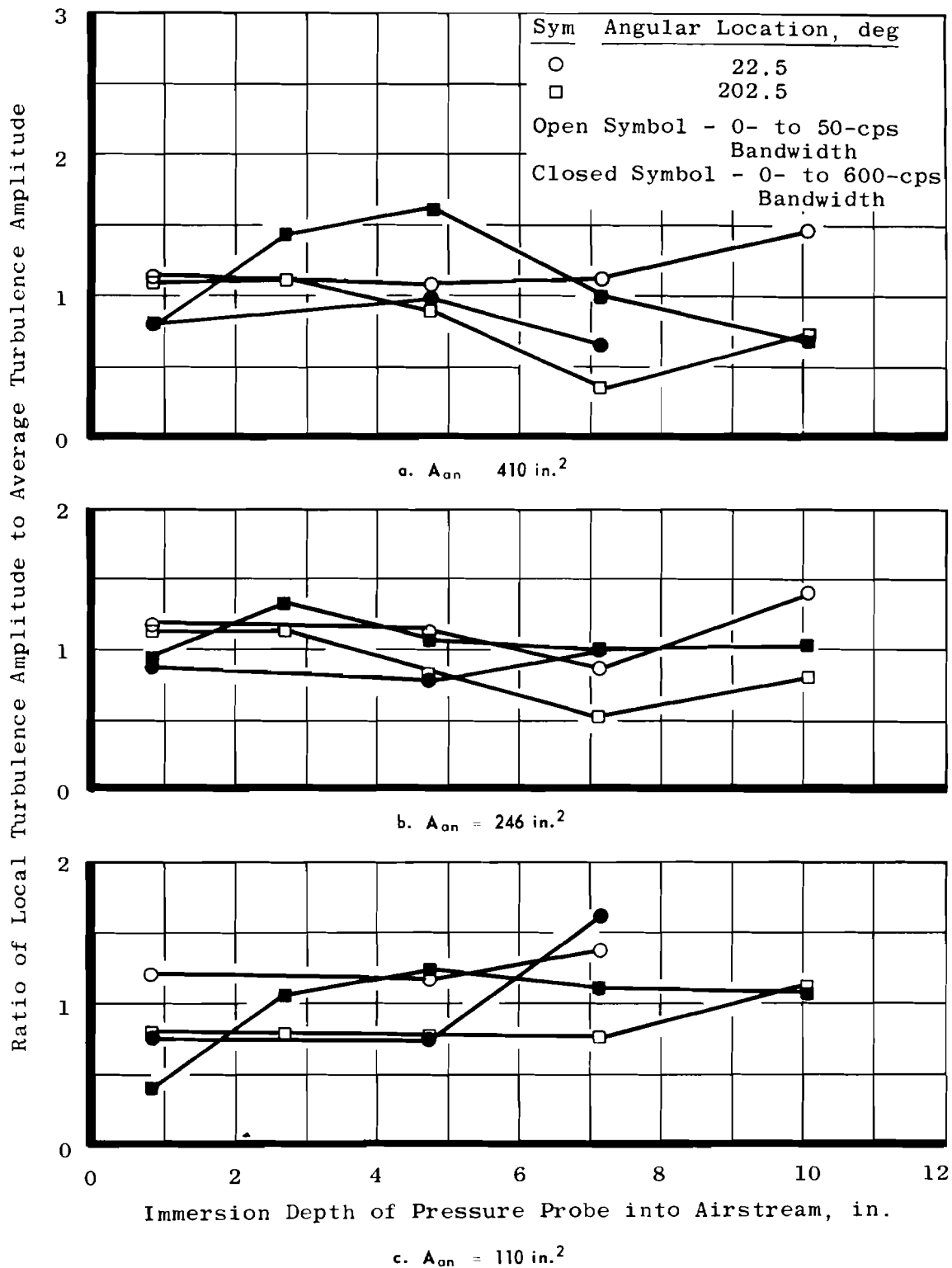


Fig. 38 Relative Turbulence Amplitude Radial Distribution,
Heavy Blockage Screen Configuration, $W_{ac} = 260 \text{ lb}_m/\text{sec}$

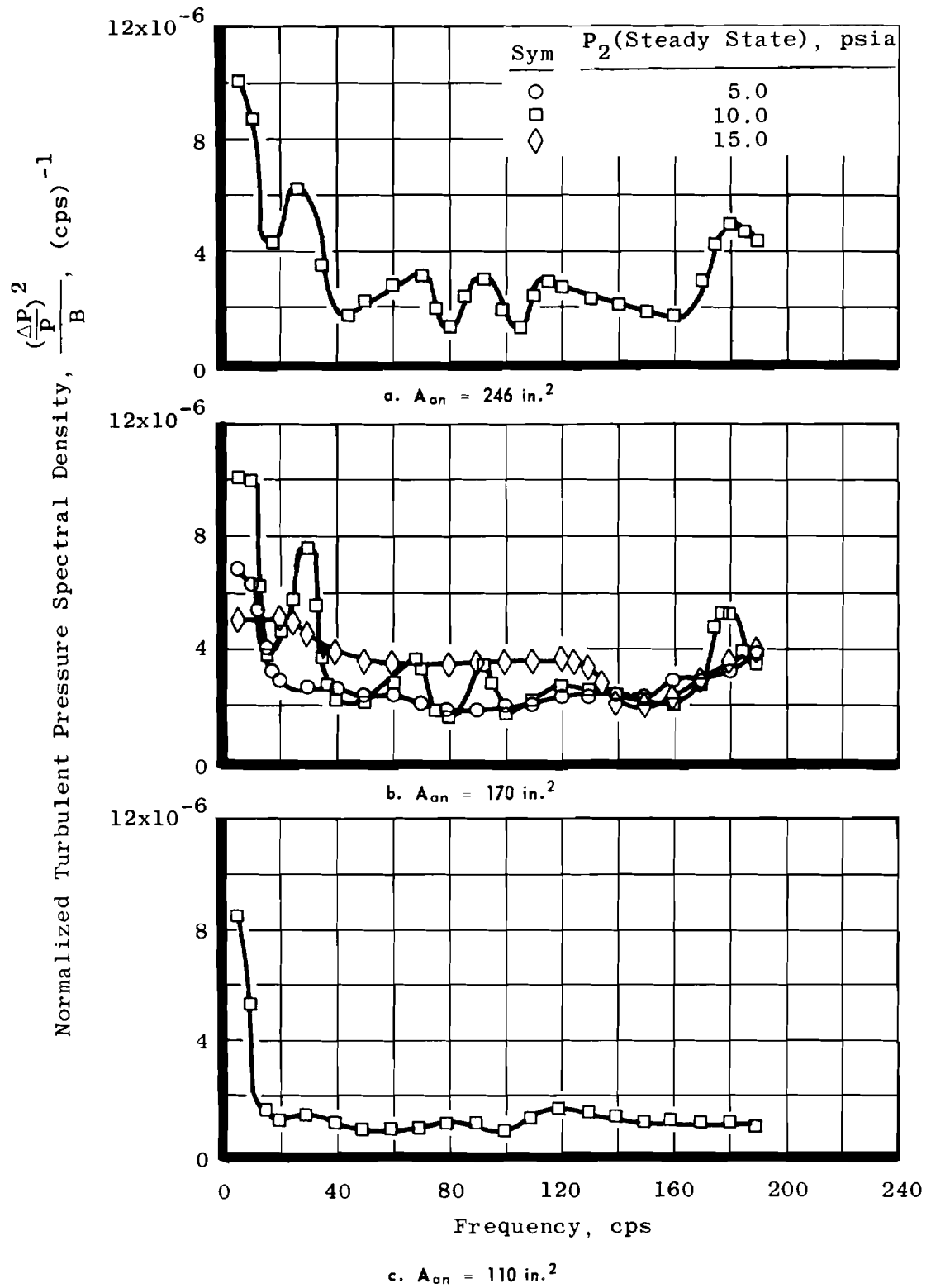
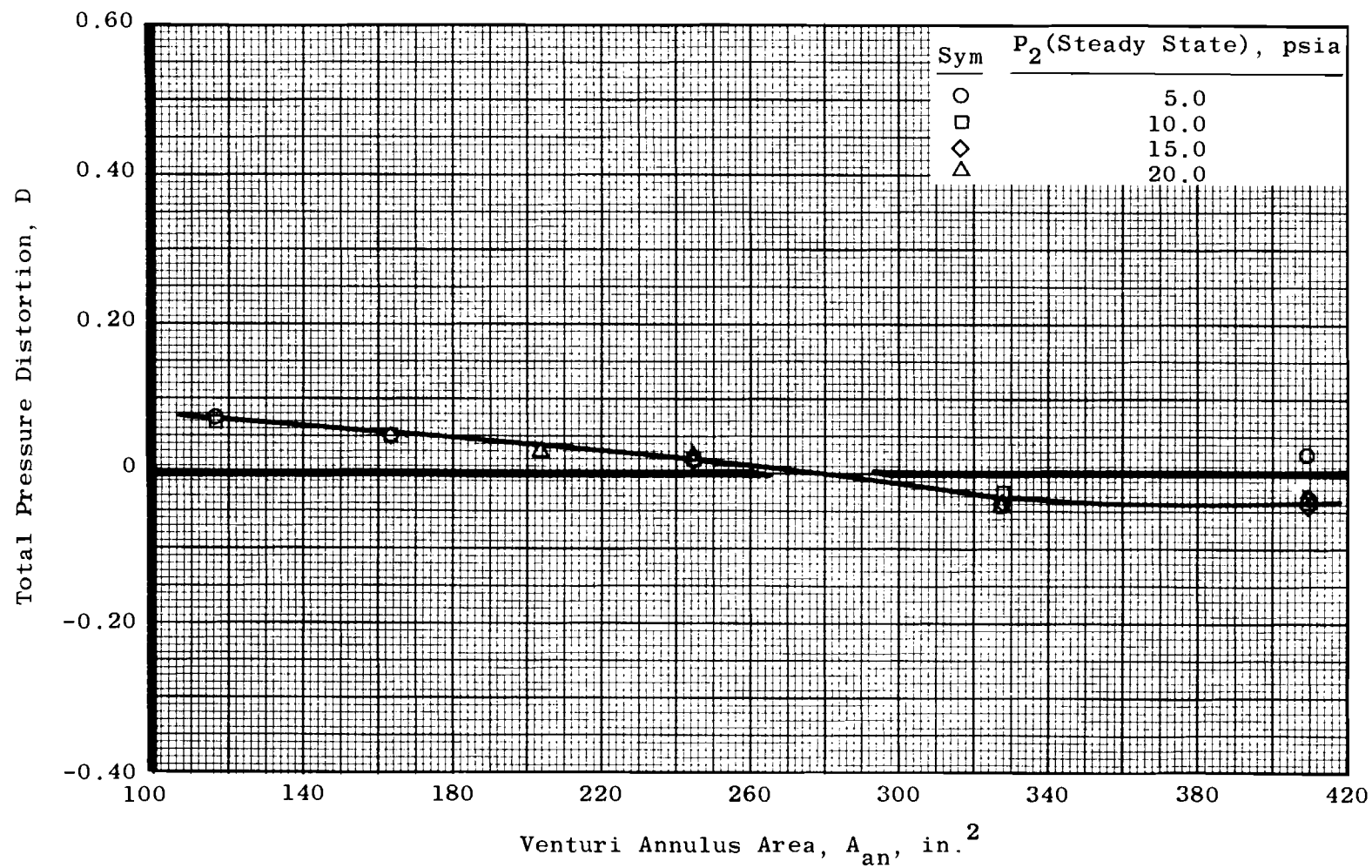
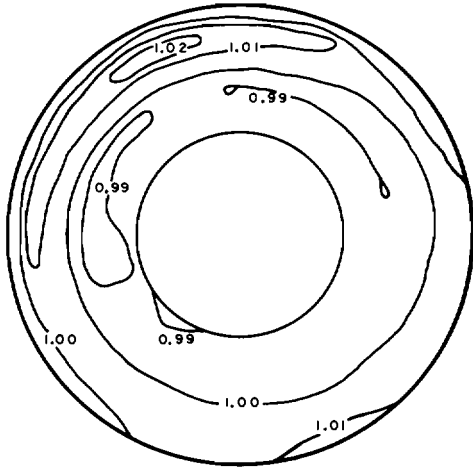


Fig. 39 Normalized Turbulent Pressure Spectral Density,
Heavy Blockage Screen Configuration,
 $W_{ac} = 260 \text{ lb}_m/\text{sec}$

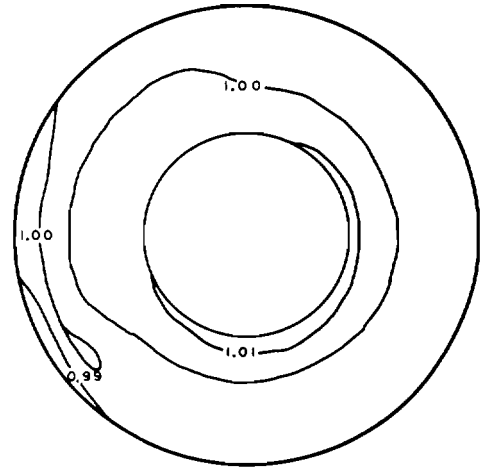


a. Variance with Annulus Area

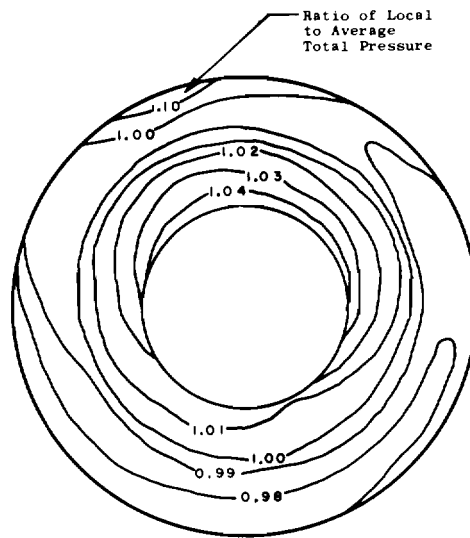
Fig. 40 Total Pressure Distortion Characteristics, Heavy Blockage Screen Configuration, $W_{ac} = 260$ lb_m/sec



b. Distortion Pattern, $A_{an} = 410 \text{ in.}^2$



c. Distortion Pattern, $A_{an} = 246 \text{ in.}^2$



d. Distortion Pattern, $A_{an} = 110 \text{ in.}^2$

Fig. 40 Concluded

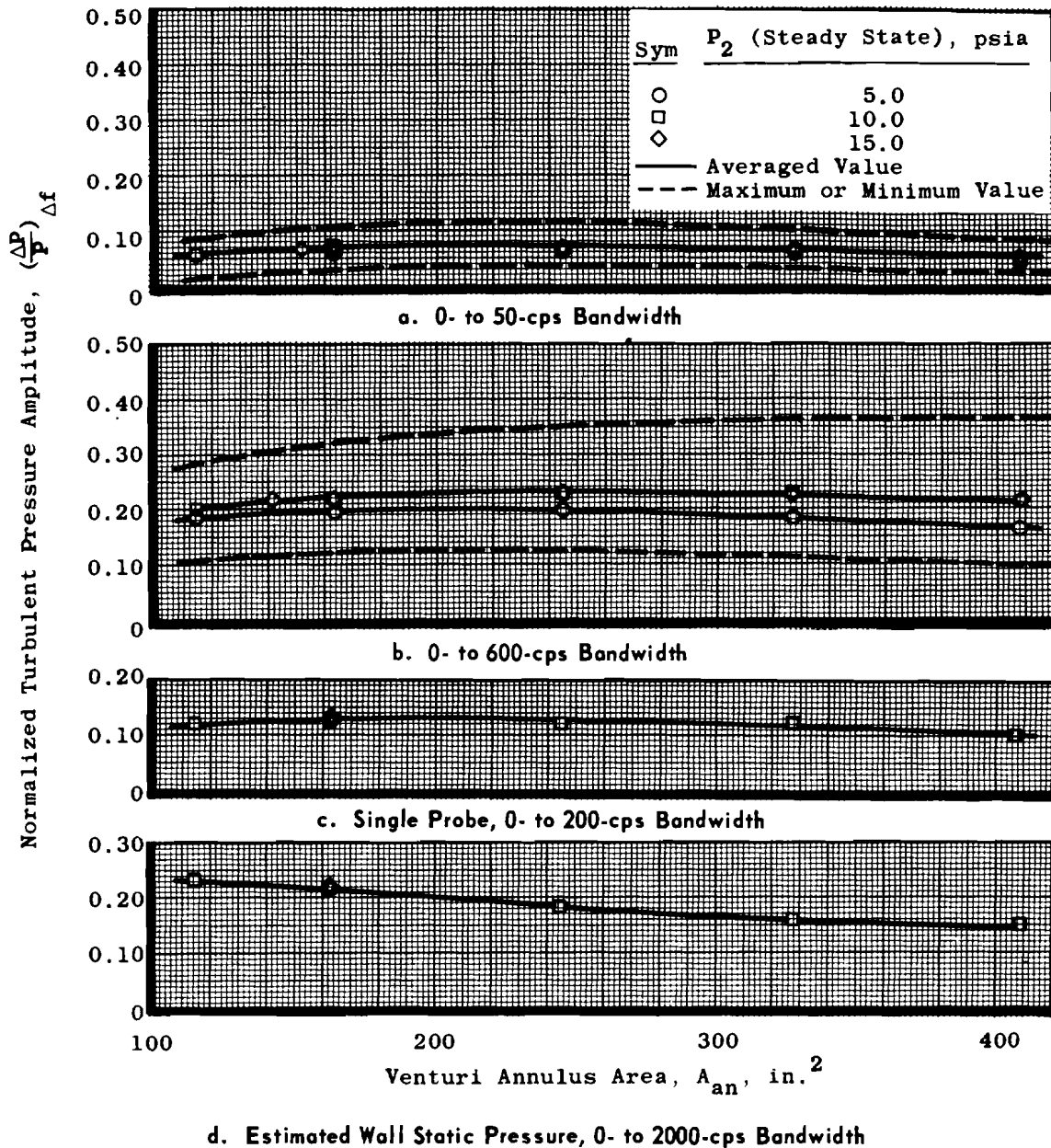


Fig. 41 Variance of Turbulence Amplitude with Annulus Area,
Vortex Generator Screen Configurations, $W_{ac} = 260 \text{ lb}_m/\text{sec}$

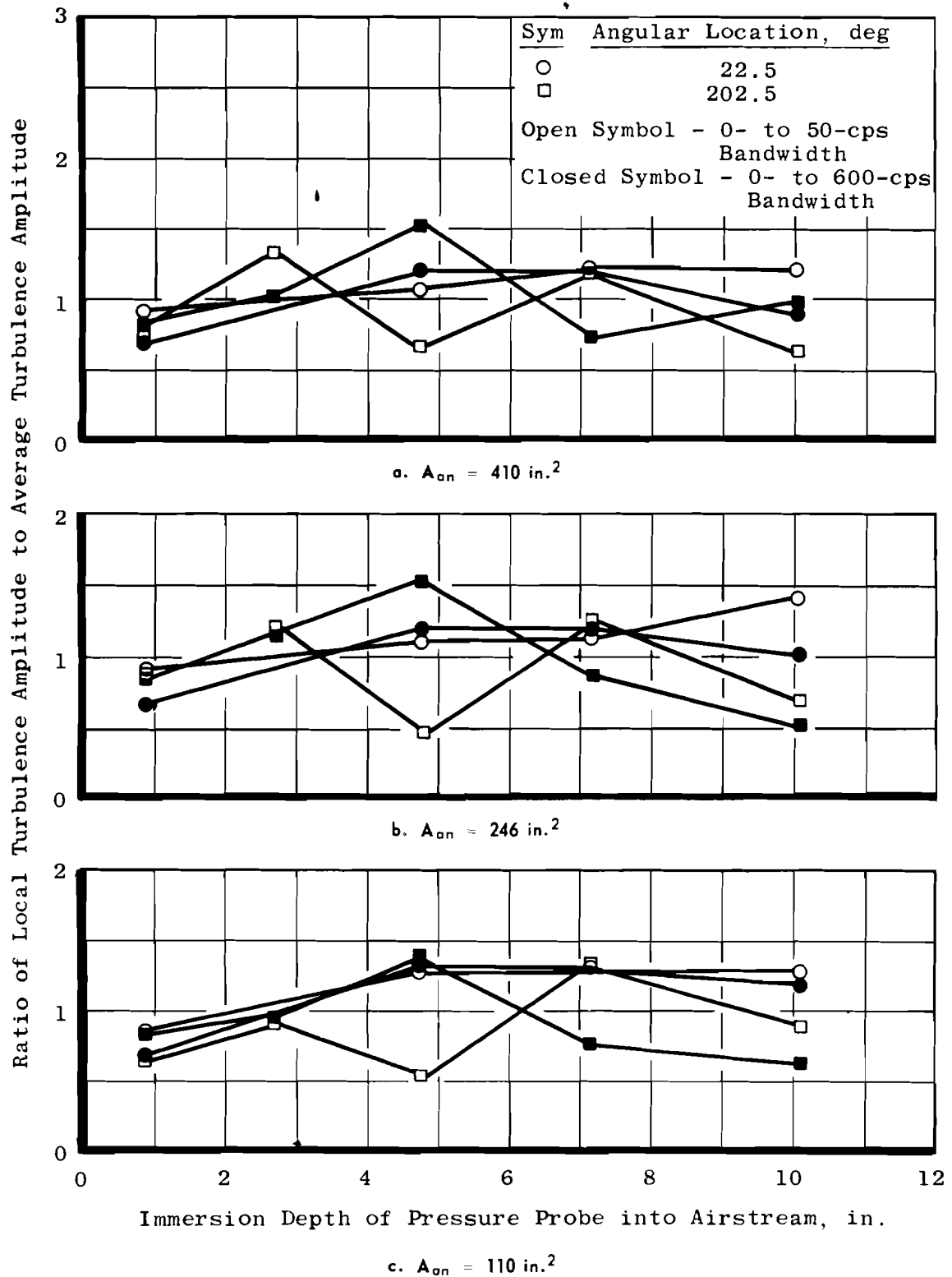


Fig. 42 Relative Turbulence Amplitude Radial Distribution,
Vortex Generator Screen Configuration, $W_{a_c} = 260 \text{ lb}_m/\text{sec}$

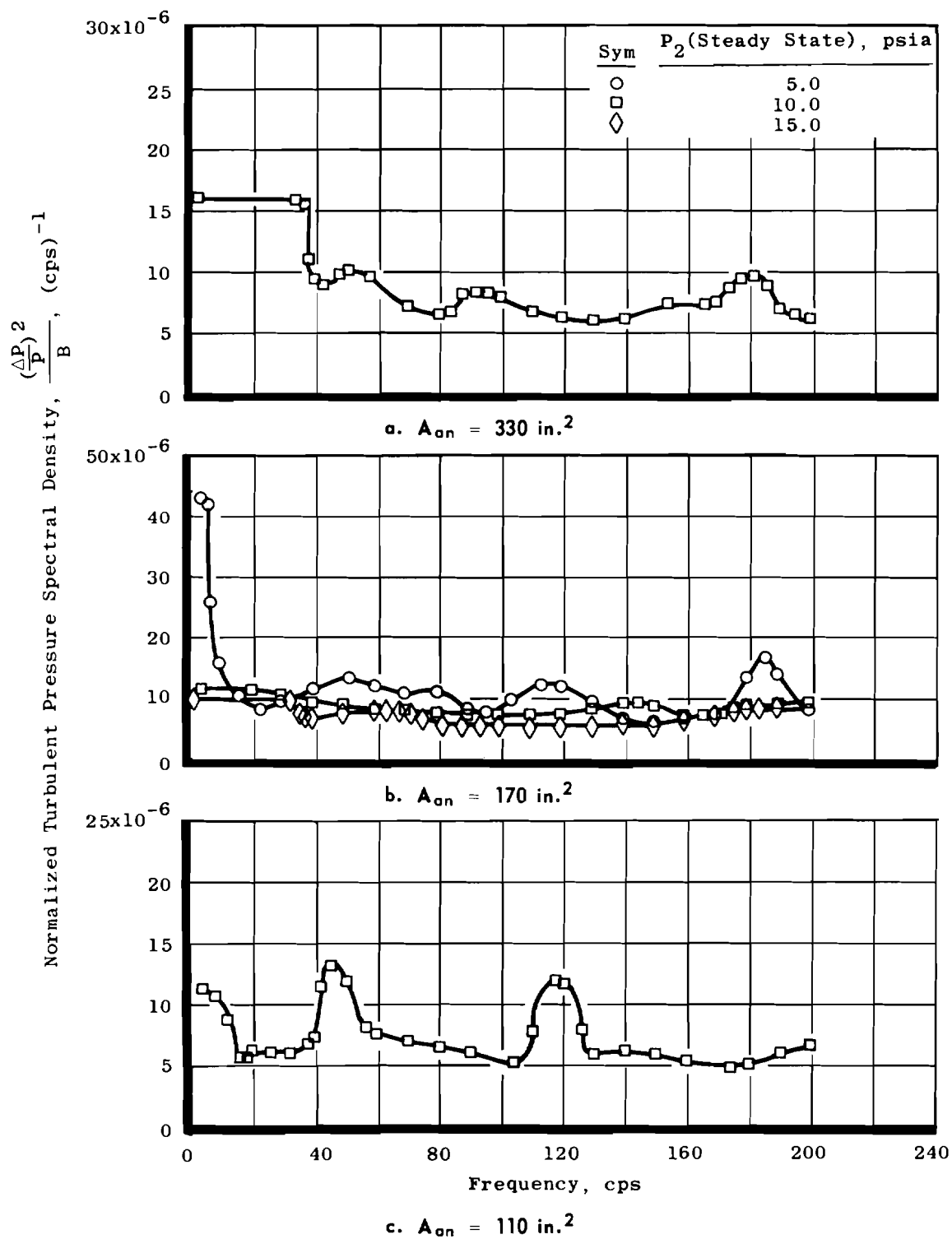
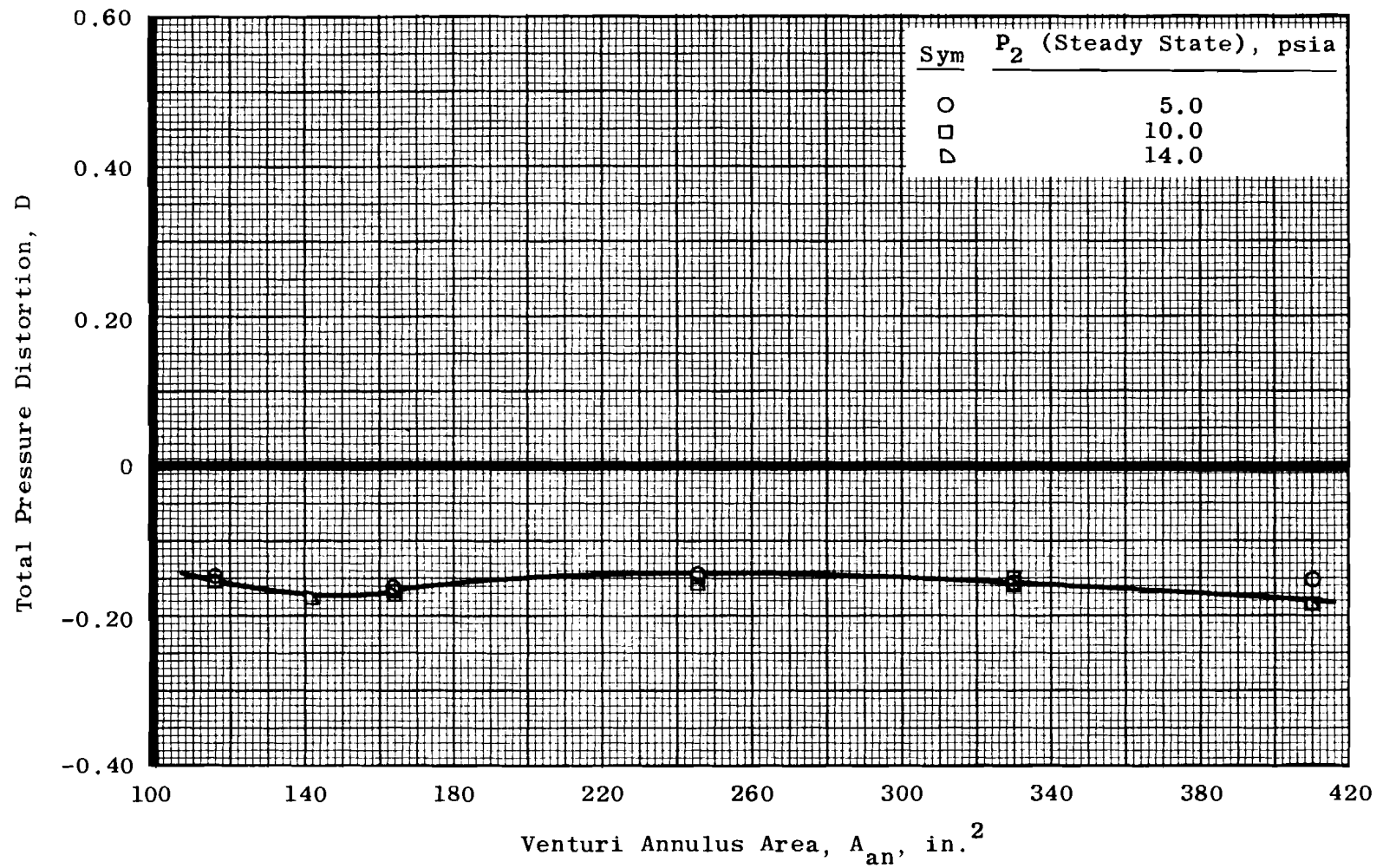
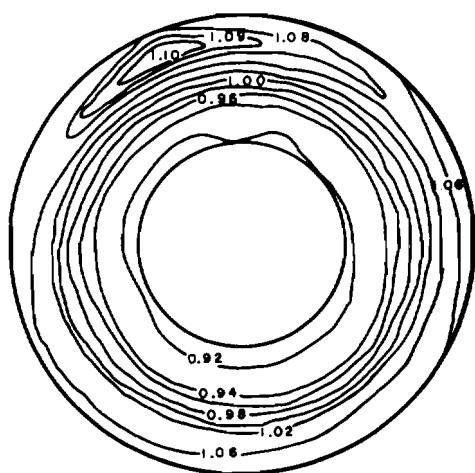


Fig. 43 Normalized Turbulent Pressure Spectral Density,
Vortex Generator Screen Configuration,
 $W_{ac} = 260 \text{ lb}_m/\text{sec}$

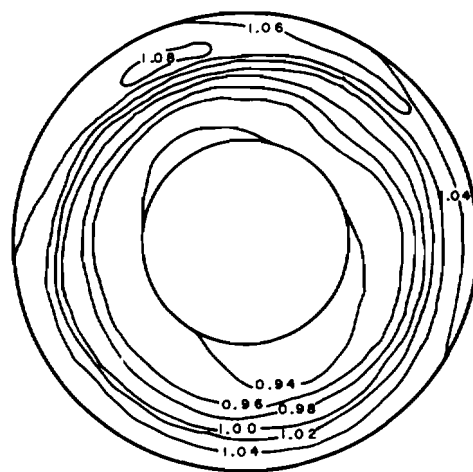


a. Variance with Annulus Area

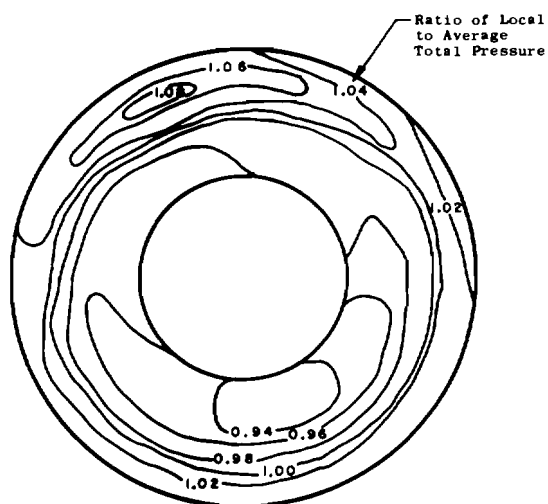
Fig. 44 Total Pressure Distortion Characteristics, Vortex Generator Screen Configuration, $W_{ac} = 260 \text{ lb}_m/\text{sec}$



b. Distortion Pattern, $A_{an} = 410 \text{ in.}^2$

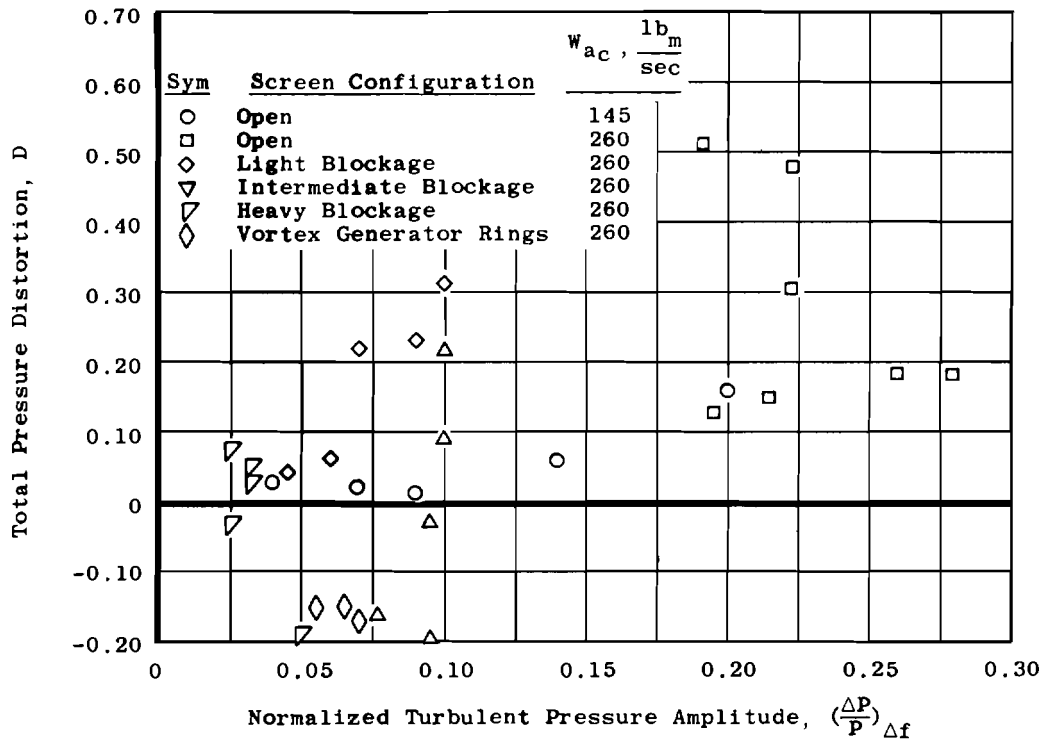


c. Distortion Pattern, $A_{an} = 246 \text{ in.}^2$

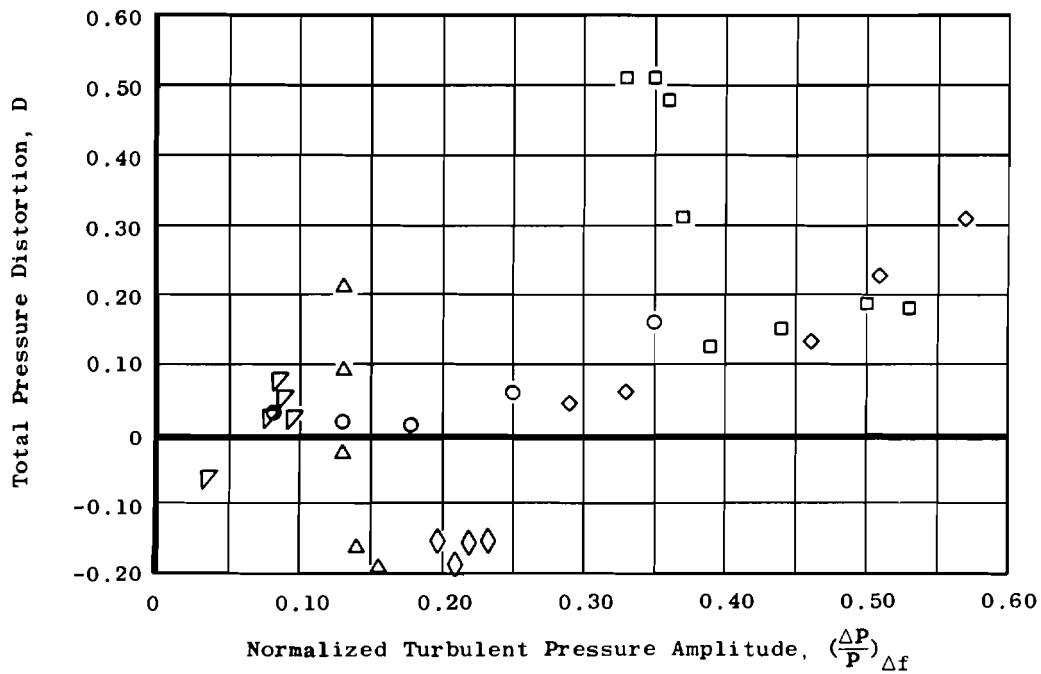


d. Distortion Pattern, $A_{an} = 110 \text{ in.}^2$

Fig. 44 Concluded



a. 0- to 50-cps Bandwidth



b. 0- to 600-cps Bandwidth

Fig. 45 Turbulence Generator Performance Map

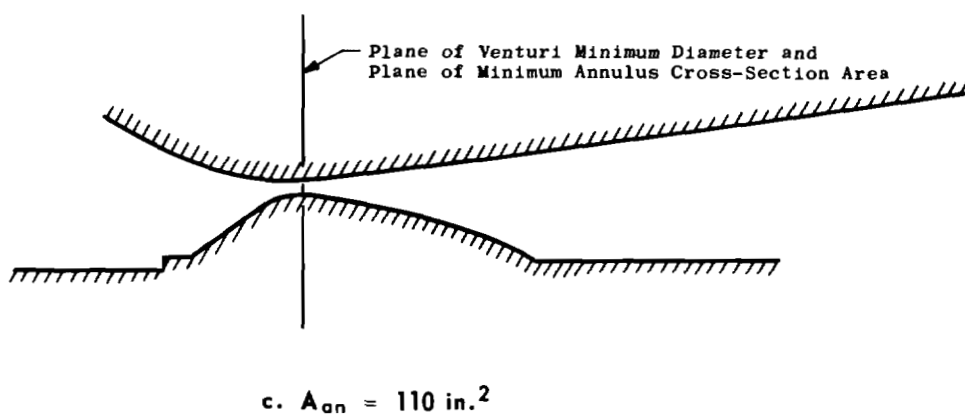
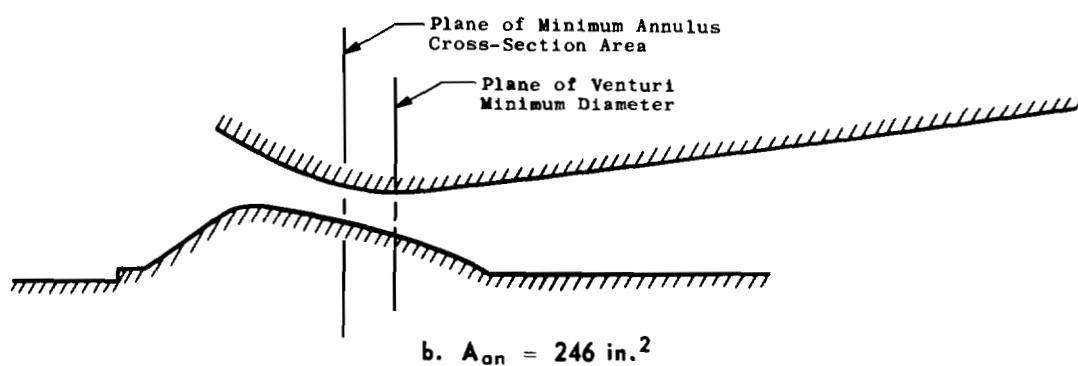
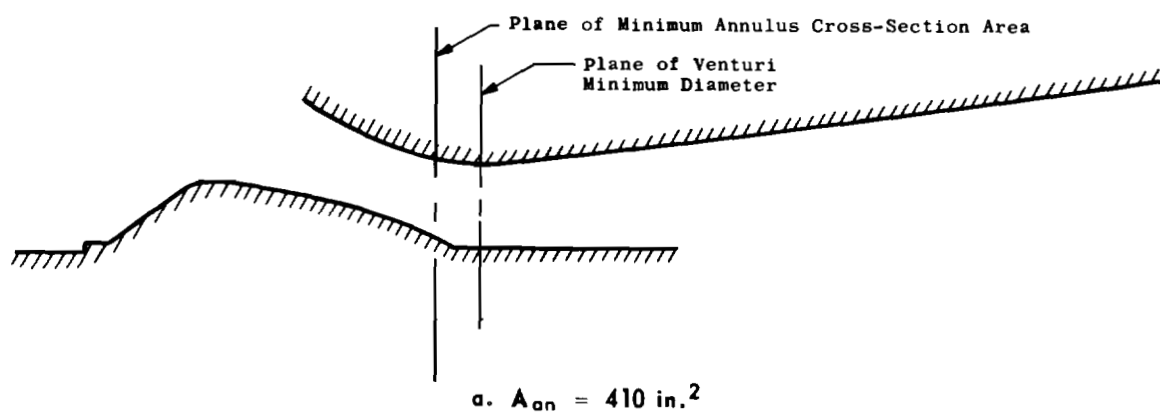


Fig. 46 Schematic of Venturi Flow Passages

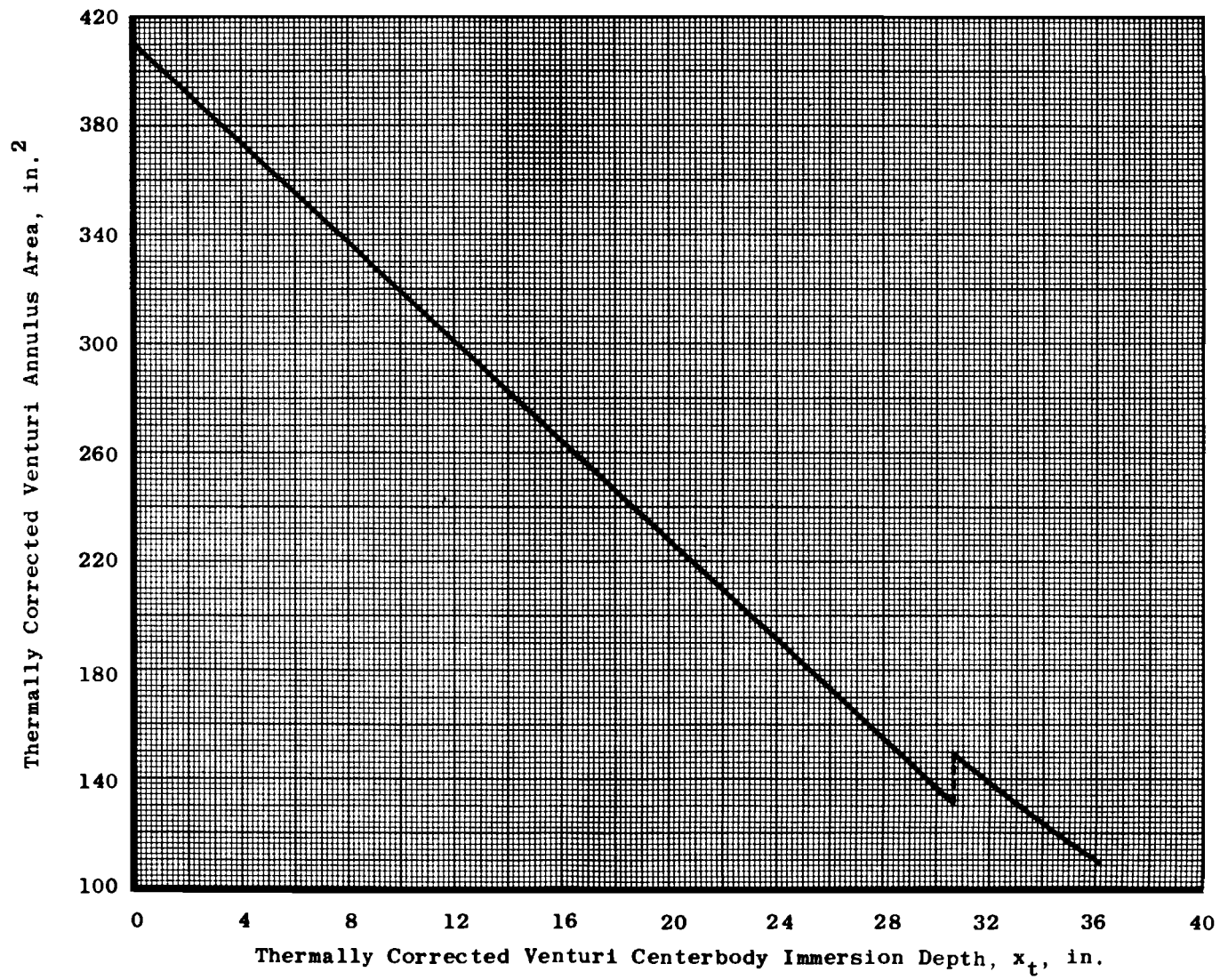


Fig. 47 Variance of Venturi Annulus Airflow Measurement Plane Area with Centerbody Position

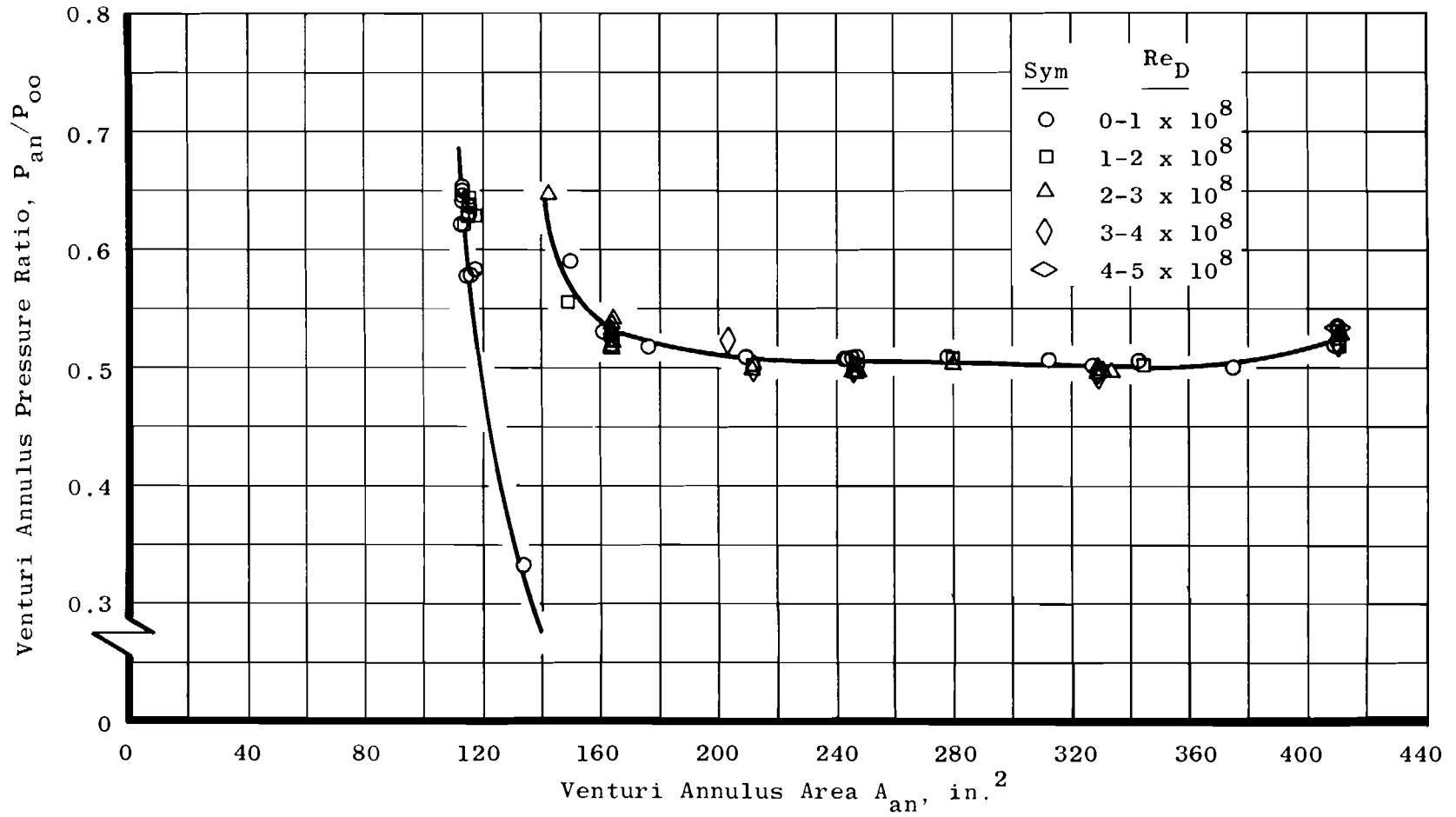


Fig. 48 Effect of Annulus Area Change on Venturi Annulus Pressure Ratio

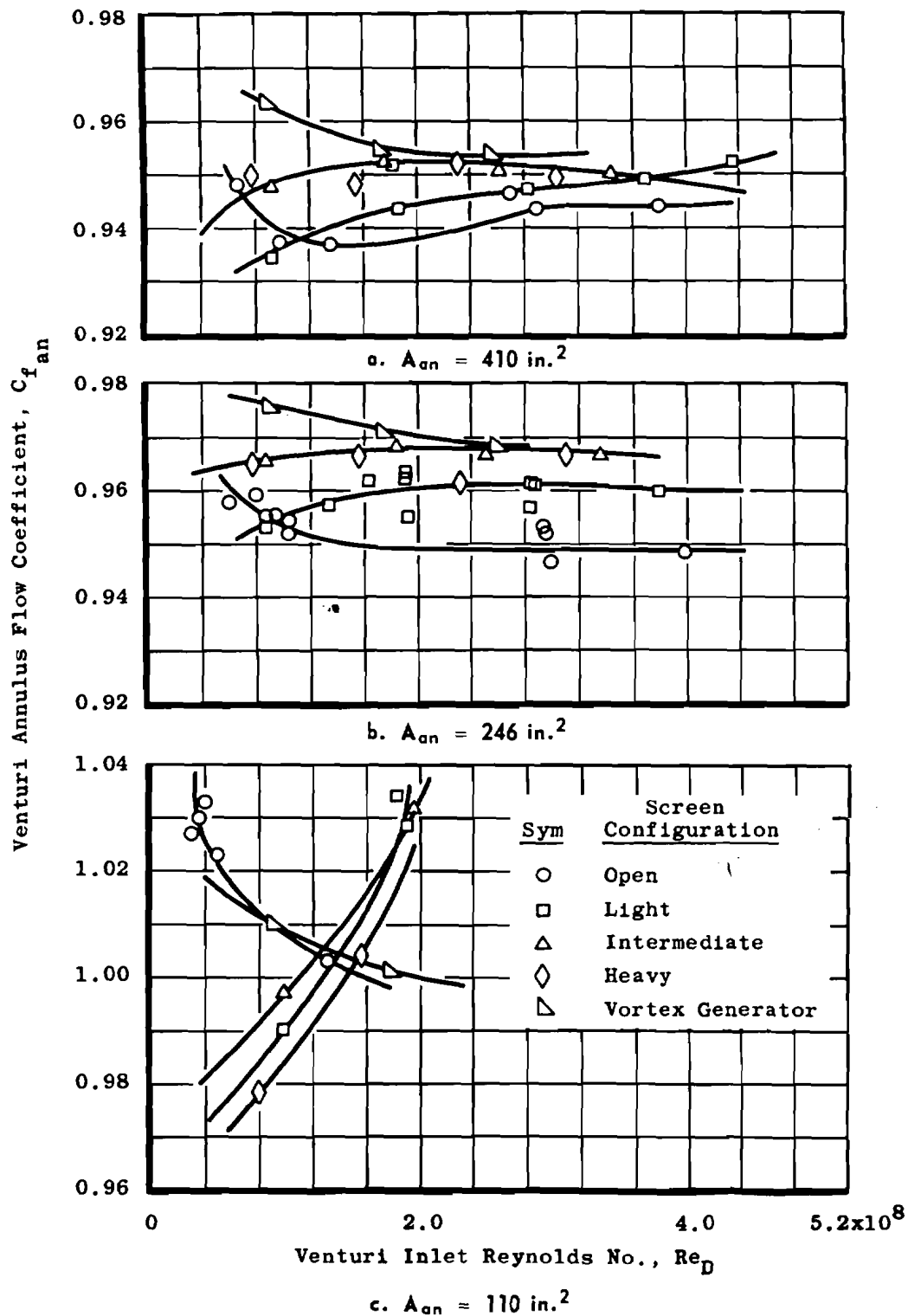
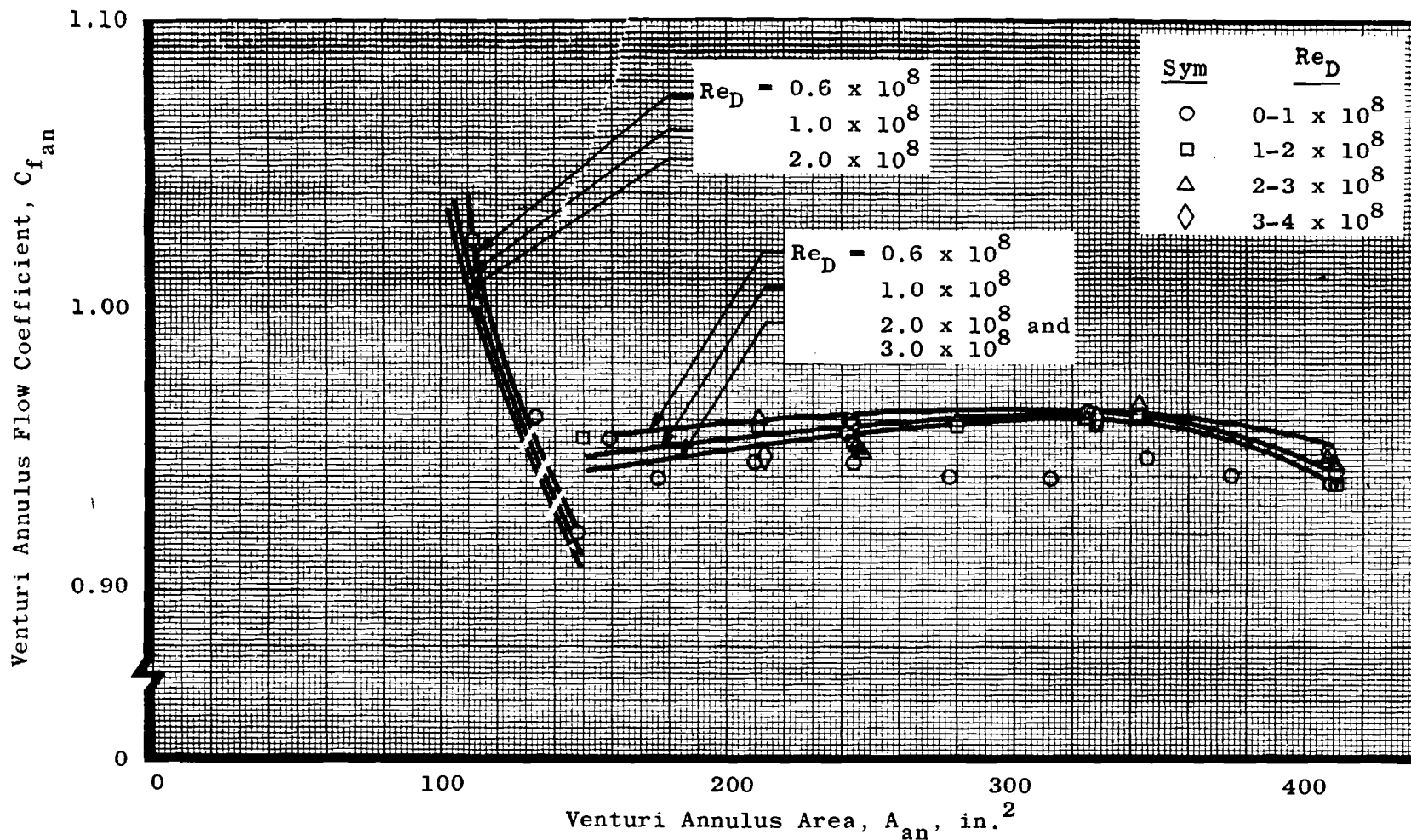
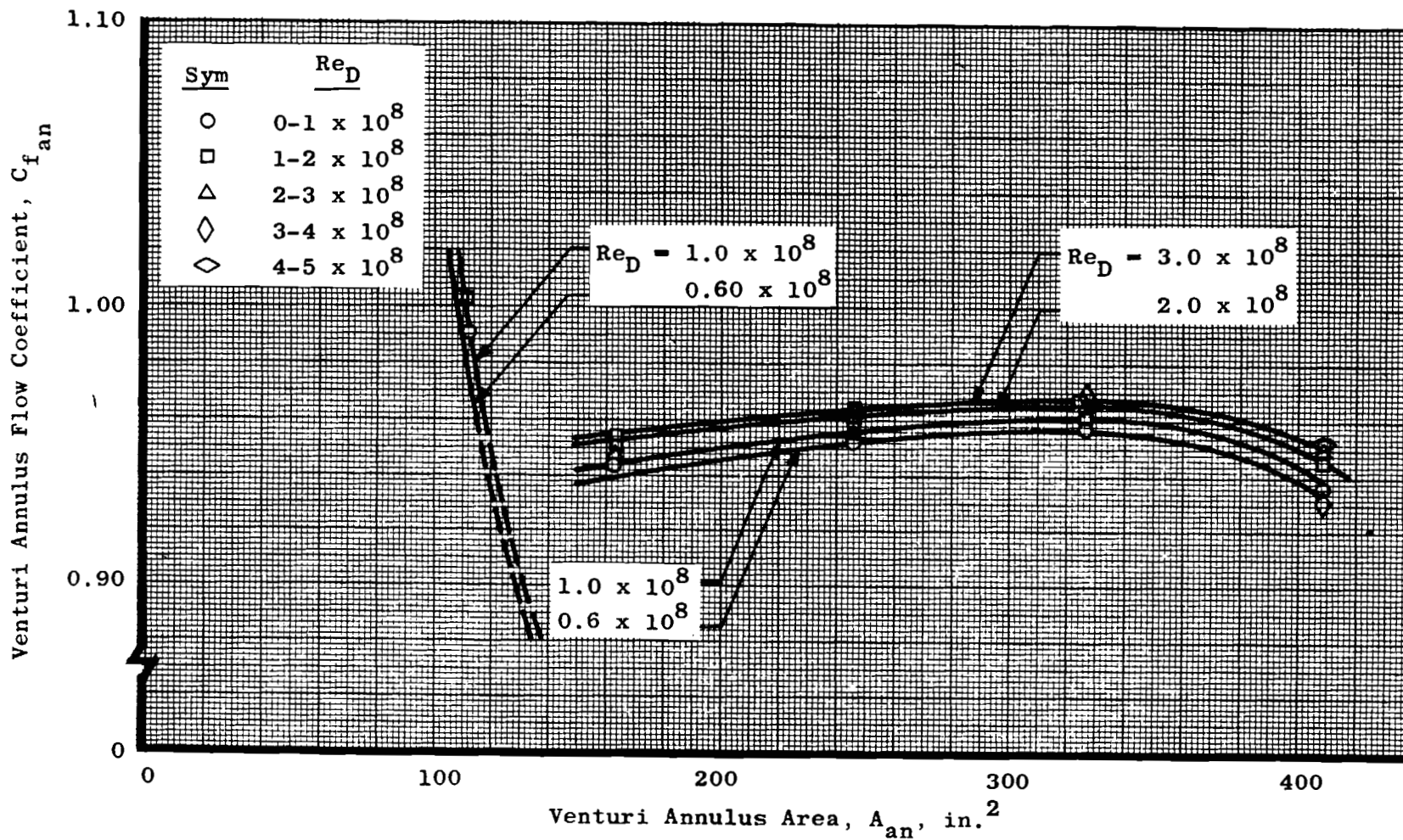


Fig. 49 Reynolds Number Effect on Venturi Annulus Flow Coefficient



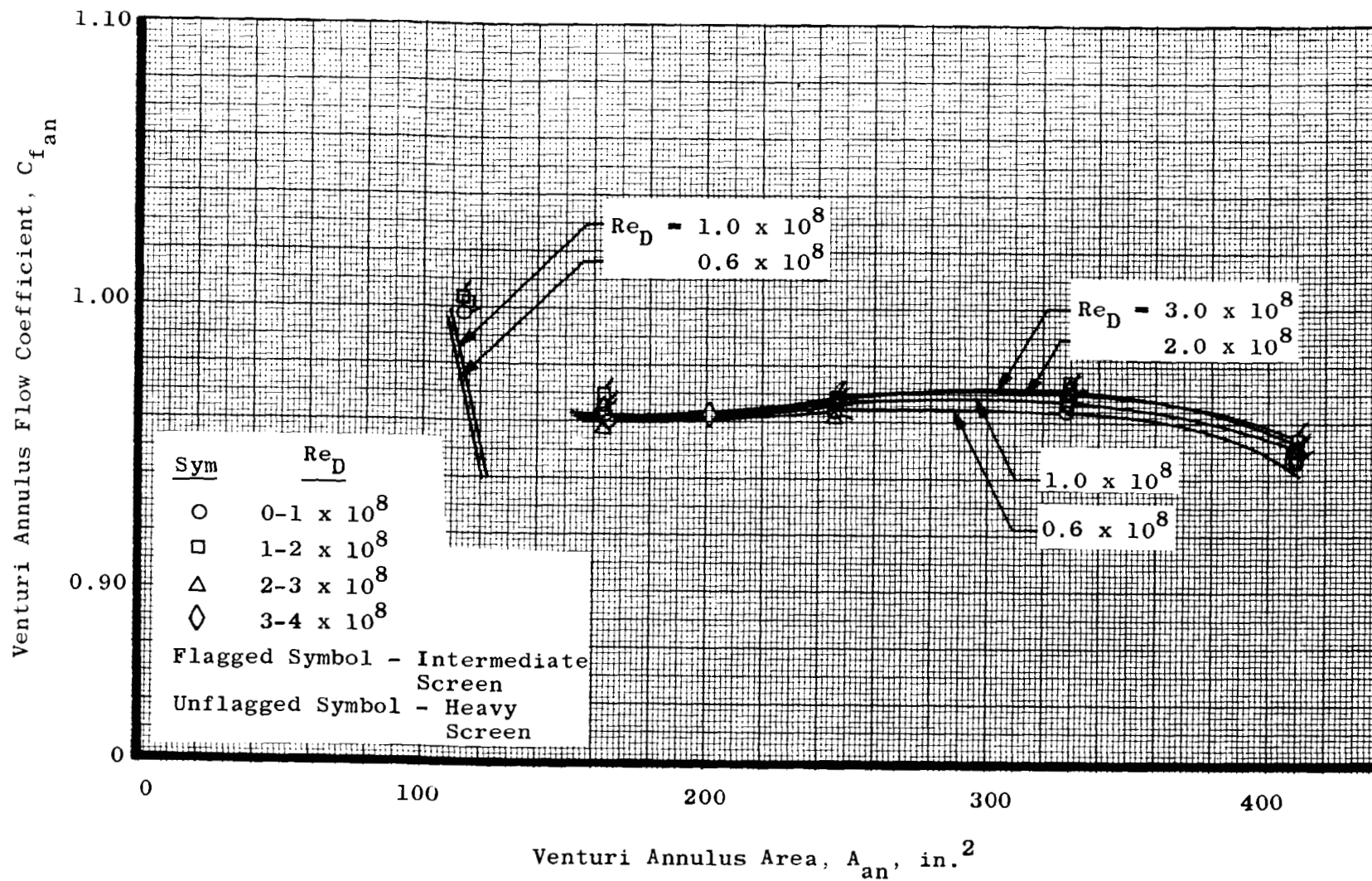
a. Open Screen Configuration

Fig. 50 Combined Flow Coefficient Curves



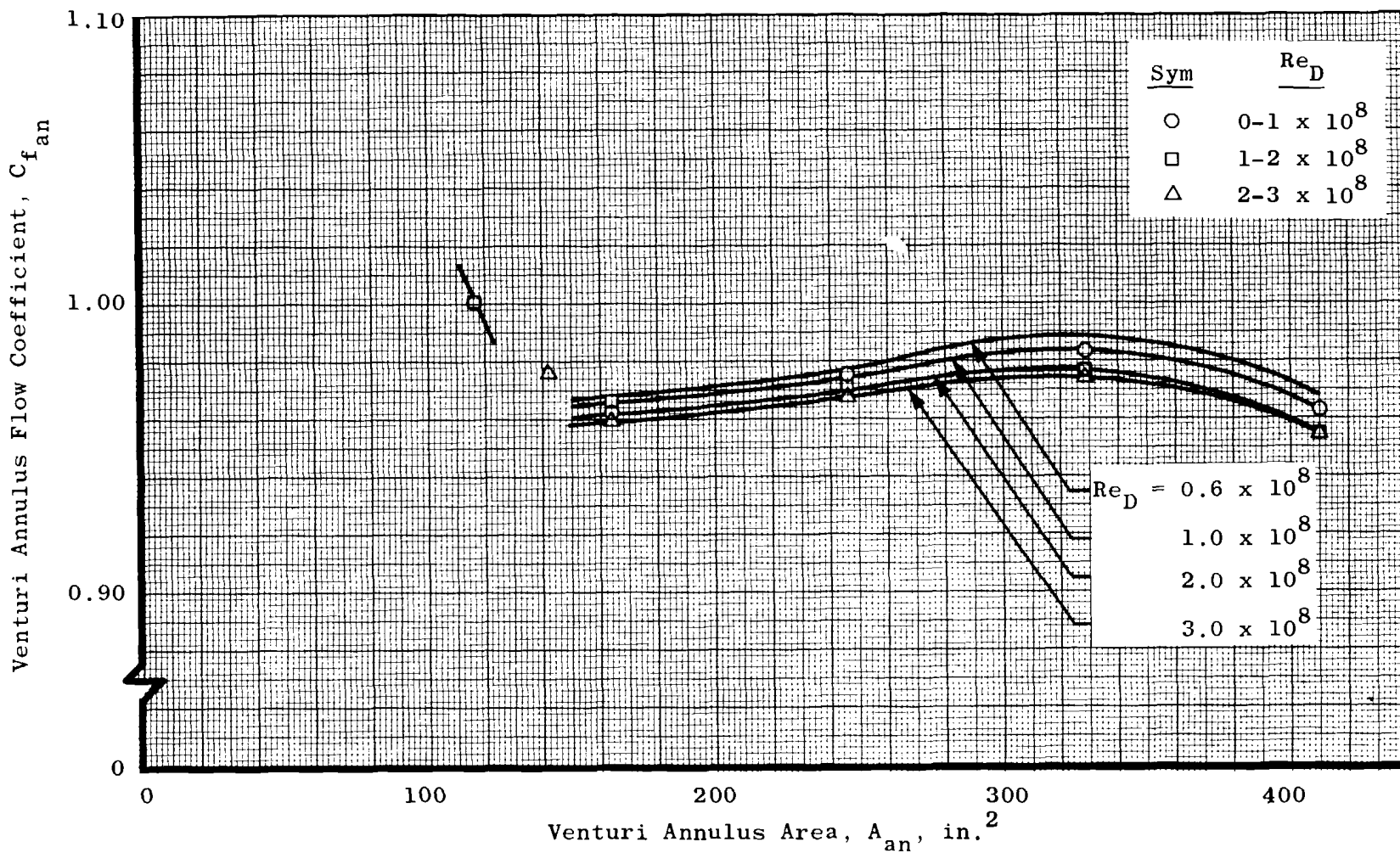
b. Light Blockage Screen Configuration

Fig. 50 Continued



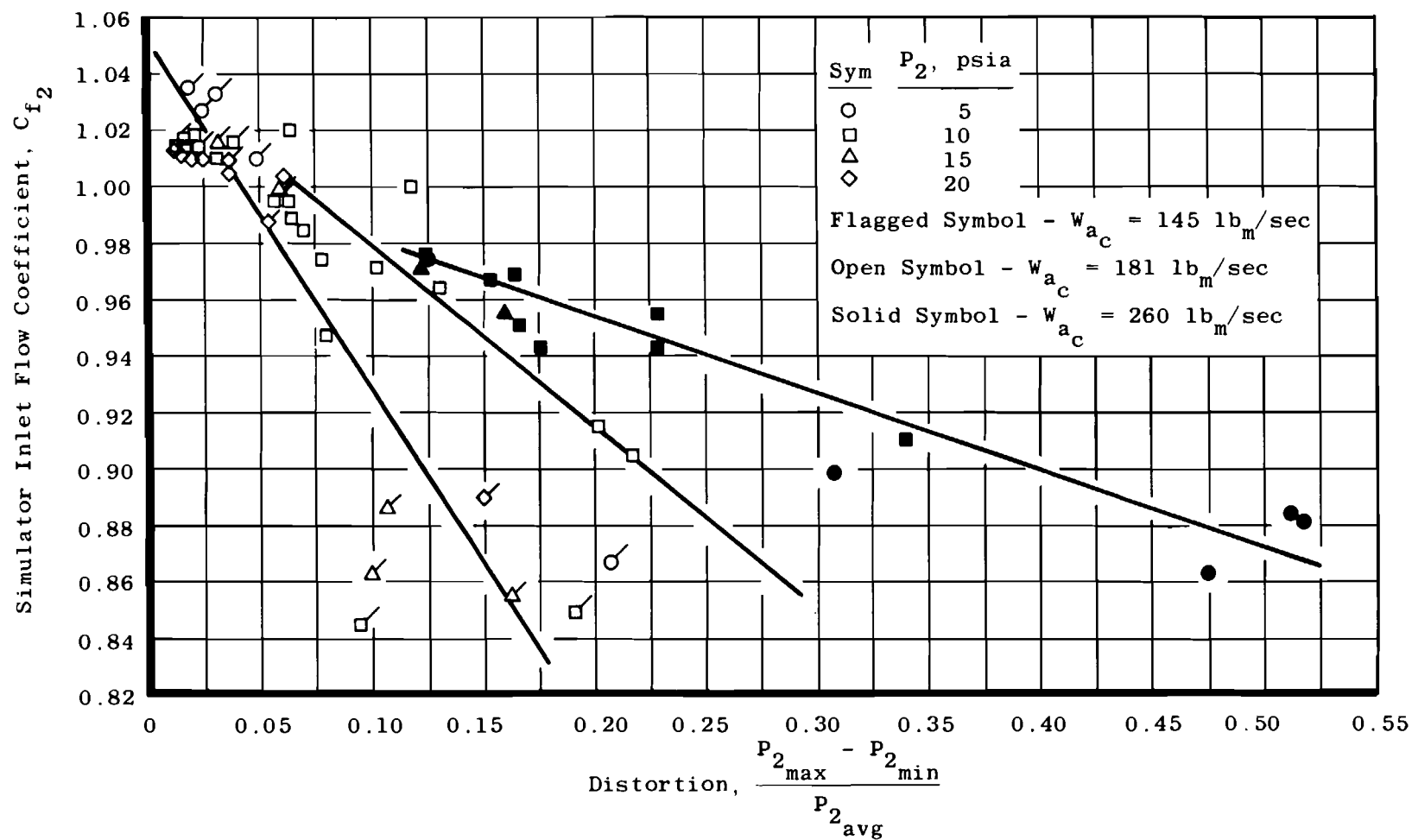
c. Intermediate and Heavy Blockage Screen Configuration

Fig. 50 Continued



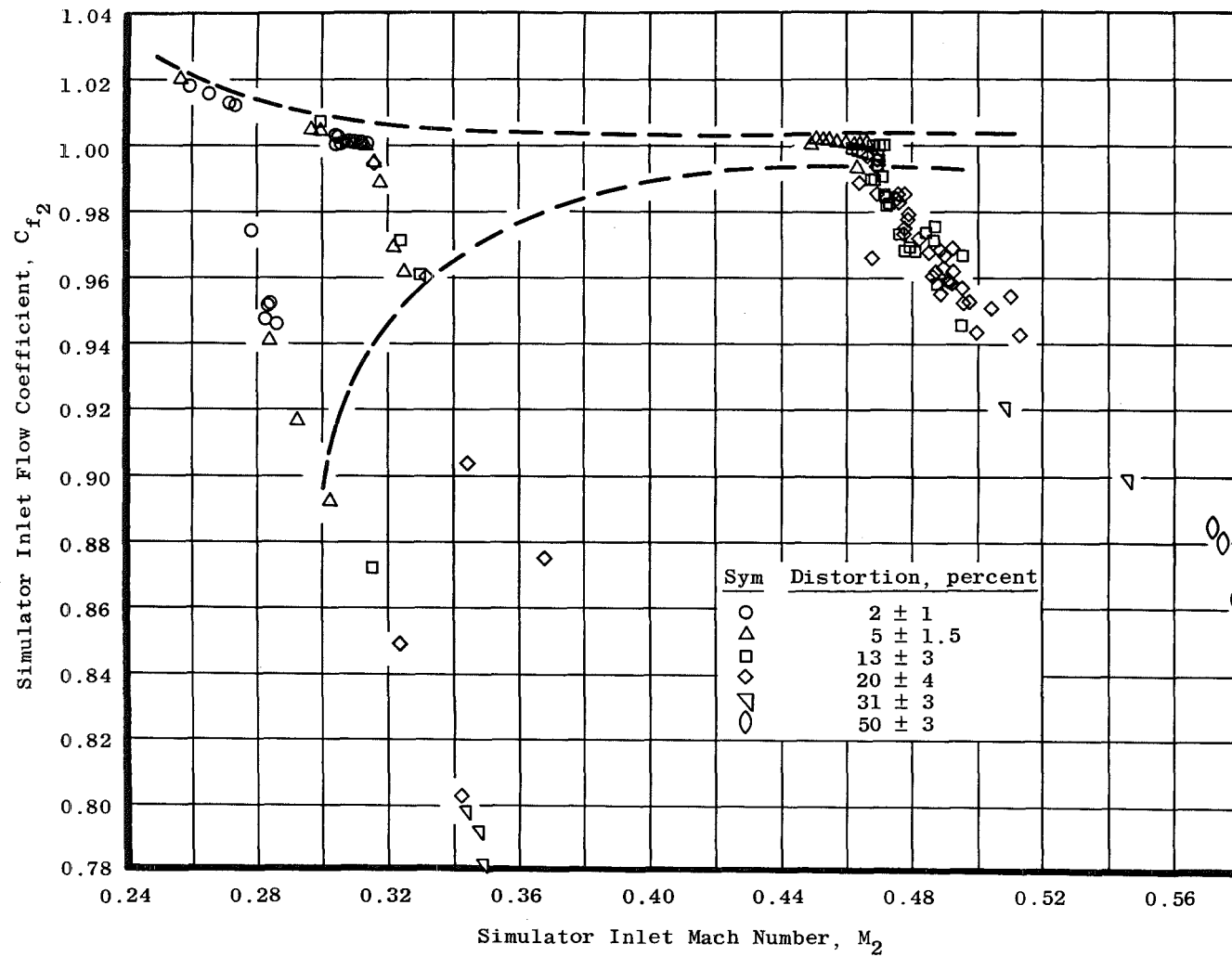
d. Vortex Generator Screen Configuration

Fig. 50 Concluded



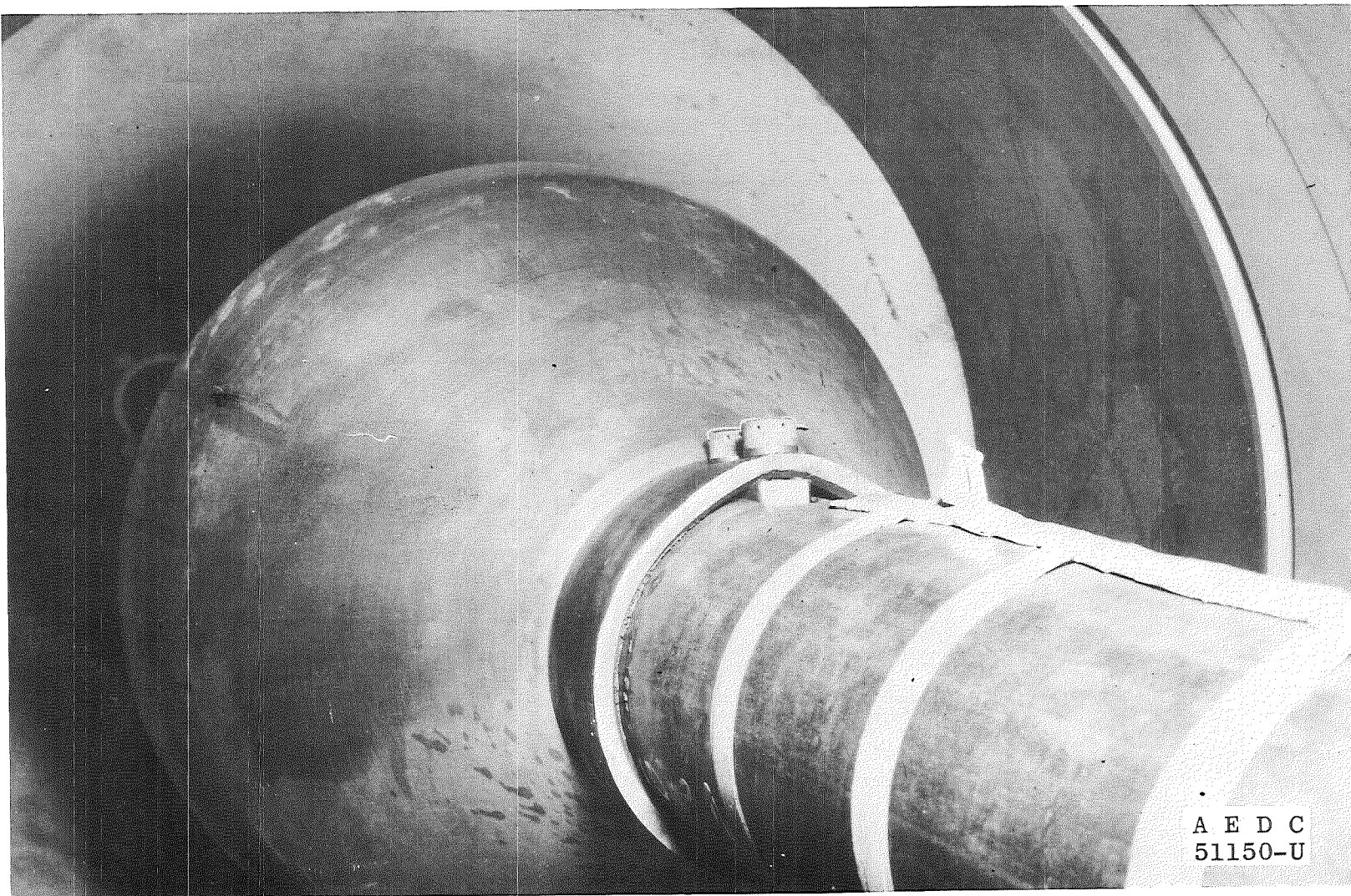
a. Variance with Distortion

Fig. 51 Simulator Inlet Flow Coefficient



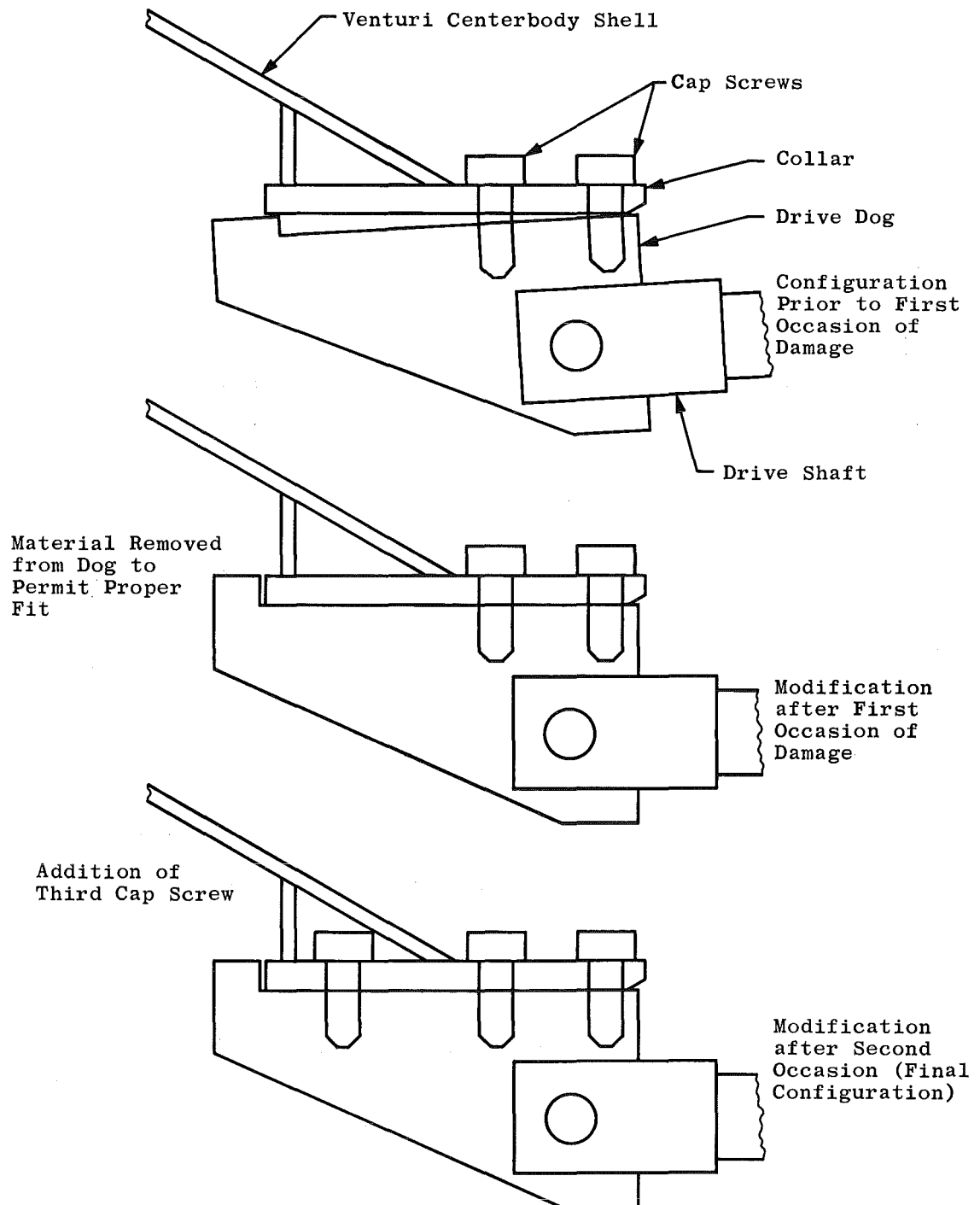
b. Variance with Mach Number

Fig. 51 Concluded



a. Photograph

Fig. 52 Venturi Centerbody Deformation and Modifications



b. Schematics

Fig. 52 Concluded

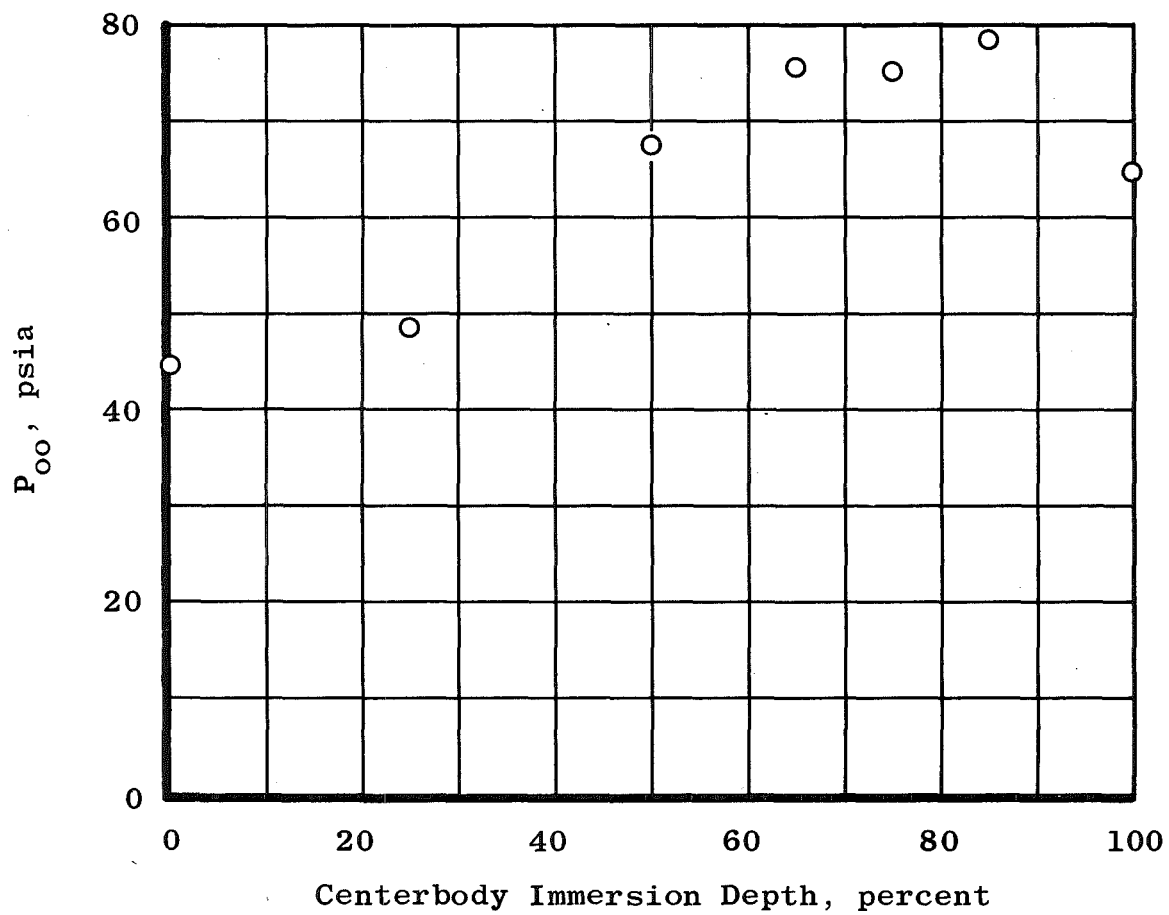


Fig. 53 Venturi Centerbody Loading

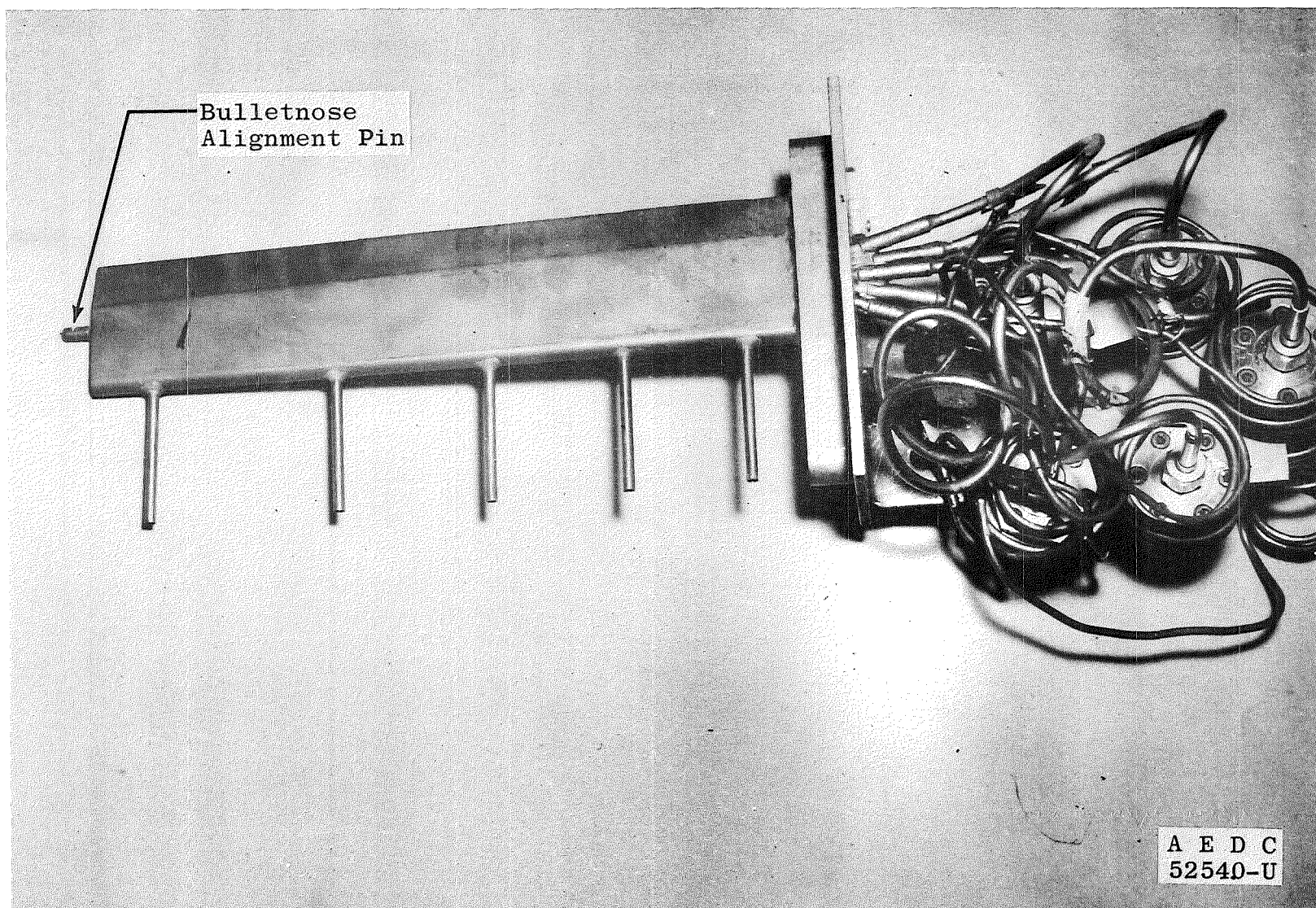


Fig. 54 Turbulence Total Pressure Rake

TABLE I

SCREEN CONFIGURATIONS

Configuration* Number	Blockage Description	Blockage, percent	Forward	Screens** Aft
4000 or 4100	Open	0	None	None
4007	Light	34.9	None	32 in. - 4 x 4 x 0.047
4003	Intermediate	53.0	30 in. diam*** 8 x 8 x 0.047 on a 32 in. diam 4 x 4 x 0.047	None
4004	Heavy	78.7	30 in. diam 8 x 8 x 0.47 on a 32 in. diam 4 x 4 x 0.047	Full - 8 x 8 x 0.032
4008	Vortex Generator Rings	60.4	Full - 1 x 1 x 0.063	Three 2-1/4-in.-wide concentric rings with inside radius of 5, 9, and 13 in.

*4000 indicates 777.7-in.² nozzle installed on simulator.

4100 indicates 549.8-in.² nozzle installed on simulator.

**All screen overlays are listed in the order in which they were attached to the grid support.

***Interpretation of screen wire specifications

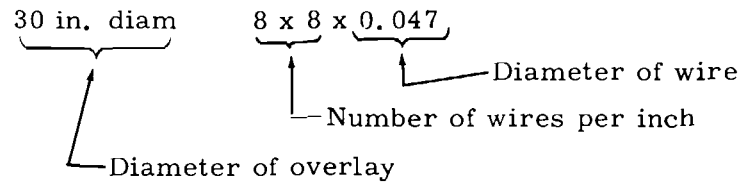


TABLE II
INDEX TO TABULATED DATA

<u>Test Number</u>	<u>Screen Configuration Number</u>	<u>Page Number (Data Package)</u>
60	4000	21
61	4000	37
62	4001*	52
63	4002*	72
64	4003 and 4004	85
65	4005*	103
66	4003 and 4006*	118
67	4000	138
68	4007	177
69	4008	189
70	4004	222
71	4003 and 4000	250
72	4007	303
73	4100	345
74**	4100	463
75**	4100	496

*Screen configurations which were found unsuitable or redundant and are therefore not covered by this report. Details of these screens are included in the Data Package.

**Test run at simulator inlet total temperature of 1083°R.

TABLE III
TABULATED DATA HEADINGS

Figure 1 illustrates the flow of air through a gas turbine engine, divided into four main sections: Compressor, Combustor, Turbine, and Nozzle. Each section is associated with a 'Run No.' and 'Setting Conditions'.

- Compressor Section:**
 - Run No. 1
 - Setting Conditions: P_2 (psia), T_2 ($^{\circ}R$), P_0 (psia), A_{an} (in^2), A_8 (in^2)
- Combustor Section:**
 - Run No. 2
 - Setting Conditions: x_p , P_{00} (psia), P_{in-su} (psia), P_{in} (psia), $\frac{P_{an}}{P_{00}}$, C_{fan} , C_{fL} , C_{fin} , $A_{an,eff}$ (in^2), T_{win} ($^{\circ}R$), $T_{wan,ad}$ ($^{\circ}R$), W_{an} (lb/sec), W_8 (lb/sec), $\frac{P_{00}-P_2}{P_{00}}$, T_2 ($^{\circ}R$), P_2 (psia), p_2 (psia)
- Turbine Section:**
 - Run No. 3
 - Setting Conditions: C_{t2} , $T_{w2,ad}$ ($^{\circ}R$), W_{a2} (lb/sec), M_2 , R_{8I} , C_{t2} , $\frac{P_2-P_7}{P_2}$ (psia), P_7 (psia), $\frac{P_7}{P_0}$, C_{d8} , C_{t8} , T_{w8} ($^{\circ}R$), $T_{w8,ad}$ ($^{\circ}R$), $\frac{W_{a8}\sqrt{\delta_2}}{\delta_2}$ (lb/sec), $W_{a8,eq}$ (lb/sec), p_0 (psia), C_{tx}
- Nozzle Section:**
 - Run No. 4
 - Setting Conditions: x (in), x_{tc} (in), R_{PL} , A_{an} (in^2), γ_2 , $\sqrt{\delta_2}$, δ_2 , $P_{2,max}$ (psia), $P_{2,min}$ (psia)

TABLE III (Concluded)

TYPICAL COMBINED TEMPERATURE AND PRESSURE REFERENCE PRINTOUT

T ₂		T _{WIn}	T _{WVPS}	T _{W8}	P _{In}	P ₂	P ₇
T ₂₋₆₋₁	T ₂₋₁₆₋₁	T _{WIn-2-1}	T _{WVPS-1}	T _{W8-1-1}	P _{In-5-4}	P ₂₋₁₁₋₁	P ₇₋₁₋₁₃
-6-2	-16-2	-5-1	-2	-2-1	-5-4	-11-3-1	-1-13
-6-3	-16-3	-9-1		16-1-2	-5-4	-11-3-2	-1-13
-6-4	-16-4			-3-2			
-6-5	-16-5						

TYPICAL PRESSURE PRINTOUT

P ₀₀	P _{In-xu}		P _{In}		P _{In-xd}				P ₂		P ₂		P ₂		P ₇				P ₀
P ₀₀₋₁₋₁	P _{In-6}	P _{In-4}	P _{In-1-1}	P _{In-7-1}	P _{In-1}	P _{In-5}	P _{In-9}	P _{In-13}	P ₂₋₃₋₁	P ₂₋₇₋₁	P ₂₋₁₁₋₁	P ₂₋₁₇₋₁	P ₂₋₇₋₂	P ₂₋₁₇₋₂	P ₇₋₁₋₁	P ₇₋₁₋₆	P ₇₋₁₋₁₁	P ₇₋₁₋₁₆	P ₀₋₁₋₁
-2-1	-5-4	-3	-3-1	-8-1	-2	-6	-10	-14	-3-3	-7-3	-11-3	-17-3	-7-4	-17-4	-1-2	-1-7	-1-12	-1-17	-2-1
	-5-3	-2	-4-1	-10-1	-3	-7	-11	-15	-3-5	-7-5	-11-5	-17-5	-7-6	-17-6	-1-3	-1-8	-1-13	-1-18	-3-1
	-5-2	-1	-6-1	-11-1	-4	-8	-12	-16	-3-7	-7-7	-11-7	-17-7	-7-8	-17-8	-1-4	-1-9	-1-14	-1-19	-4-1
	-5-1								-3-9	-7-9	-11-9	-17-9	-7-10	-17-10	-1-5	-1-10	-1-15	-1-20	

APPENDIX I METHODS OF CALCULATION

The general methods and equations used to compute the parameters presented in this report are given below. Where applicable, the arithmetic average of pressures and indicated temperatures was used.

SPECIFIC HEAT

The specific heat at constant pressure was calculated from the empirical equation:

$$c_p = 0.2318 + 0.104 \times 10^{-4} T + 0.7166 \times 10^{-8} T^2$$

The ratio of specific heats was determined from:

$$\gamma = \frac{c_p}{c_v}$$

where

$$c_v = c_p - \frac{R}{J}$$

TEMPERATURES

The total temperature was obtained by applying a recovery factor to the indicated temperature according to the following equation:

$$T = \frac{T_i}{\left(\frac{p}{P}\right)^{\frac{\gamma-1}{\gamma}} + R F \left[1 - \left(\frac{p}{P}\right)^{\frac{\gamma-1}{\gamma}}\right]}$$

where

$$R F = 0.890 \text{ (station 2)}$$

Adiabatic wall temperatures were calculated from the expression:

$$T_{w_{ad}} = T \left\{ \left(\frac{p}{P}\right)^{\frac{\gamma-1}{\gamma}} + R F_{ad} \left[1 - \left(\frac{p}{P}\right)^{\frac{\gamma-1}{\gamma}}\right] \right\}$$

where

$$R F_{ad} = (\text{Prandtl number})^{1/3} = 0.90$$

VENTURI-VENTURI CENTERBODY ANNULUS PHYSICAL AREA

The physical area of the plane at which airflow was measured was calculated by

$$A_{an} = C_{t_v} \times A_v - C_{t_c} \times A_c$$

where

$$C_t = \frac{A(at\ T)}{A(at\ 540^{\circ}R)} = 1 + 2\alpha(\Delta T) + \alpha^2(\Delta T)^2$$

where

$$\Delta T = T_w - 540$$

The subscript w indicates wall temperature, v indicates venturi wall, and c centerbody wall.

The plane of minimum area of the venturi-venturi centerbody combination for the purposes of airflow measurement was assumed to exist at either of the following locations:

<u>Range</u>	<u>Throat Position</u>
$0 \leq x' \leq 31.00$	Throat at position 5 in. upstream of the plane of minimum venturi diameter. $A_v = \text{constant} = 499.716 \text{ in.}^2$
$31.00 < x'$	Throat at the plane of minimum venturi diameter. $A_v = \text{constant} = 425.412 \text{ in.}^2$

where

$$x' = x - \ell + \Delta x_t$$

$$x = \text{measured centerbody immersion depth}$$

and

$$\Delta x_t = (57.38 - \ell) T_{w_c} + 78.91 T_{w_v}$$

ℓ is a constant which is measured and will adjust for the fact that at x equal to zero, the minimum centerbody diameter does not lie exactly in the plane 5 in. upstream of the venturi minimum diameter plane.

The area of the centerbody is given by

$$A_c = \pi R_c^2$$

where for $0 \leq x' \leq 31.0$

$$R_c = a + b x' + c x'^2 + d x'^3 + e x'^4$$

and for $31.0 < x'$

$$R_c = a + b (x' - 5) + c (x' - 5)^2 + d (x' - 5)^3 + e (x' - 5)^4$$

where

$$a = 0.340123 \times 10^1$$

$$b = 0.42102$$

$$c = -0.17456 \times 10^{-1}$$

$$d = 0.60570 \times 10^{-3}$$

$$e = -0.83810 \times 10^{-5}$$

The above expression for R_c is an empirical curve fit for the contour of the centerbody over its range of motion in the planes of airflow measurement.

AIRFLOW

Venturi-Venturi Centerbody Annulus

Airflow at the venturi-venturi centerbody annulus was calculated from the equation:

$$W_a = \sqrt{\frac{2 \gamma_2 g}{R (\gamma_2 - 1)}} \times \frac{P_{an} A_{an} \sqrt{1 - \left(\frac{P_{an}}{P_{00}}\right)^{\frac{\gamma_2 - 1}{\gamma_2}}}}{\sqrt{T_2} \left(\frac{P_{an}}{P_{00}}\right)^{\frac{\gamma_2 - 1}{\gamma_2}}}$$

Simulator-Inlet

Airflow at station 2 (simulator inlet) was calculated by

$$W_a = \sqrt{\frac{2 \gamma_2 g}{R (\gamma_2 - 1)}} \times \frac{P_2 A_2 C_{t2} \sqrt{1 - \left(\frac{P_2}{P_2}\right)^{\frac{\gamma_2 - 1}{\gamma_2}}}}{\sqrt{T_2} \left(\frac{P_2}{P_2}\right)^{\frac{\gamma_2 - 1}{\gamma_2}}}$$

Conic Nozzle

Airflow at the exit of the conic nozzle was calculated by the following equations:

Nozzle Unchoked:

$$W_a = \sqrt{\frac{2 \gamma_2 g}{R (\gamma_2 - 1)}} \times \frac{P_0 A_s C_{t_s} C_{d_s} \sqrt{1 - \left(\frac{P_0}{P_7}\right)^{\frac{\gamma_2 - 1}{\gamma_2}}}}{\sqrt{T_2} \left(\frac{P_0}{P_7}\right)^{\frac{\gamma_2 - 1}{\gamma_2}}}$$

where

C_{d_s} , the nozzle discharge coefficient is given by

$$C_{d_s} = a_s + b_s \left(\frac{P_7}{P_0} \right) + c_s \left(\frac{P_7}{P_0} \right)^2 + d_s \left(\frac{P_7}{P_0} \right)^3$$

and the constants in this equation are:

A_s , in. ²	a_s	b_s	c_s	d_s
549.8	0.83923	$- 0.79751 \times 10^{-2}$	$+ 0.69680 \times 10^{-1}$	$- 0.17815 \times 10^{-1}$
777.7	0.88492	$- 0.87970 \times 10^{-1}$	0.11382	$- 0.25740 \times 10^{-1}$

The expression for the nozzle discharge coefficient is an empirical curve fit taken from experimental data.

Nozzle choked:

$$W_a = P_7 C_{d_s} A_s C_{t_s} \sqrt{\frac{\gamma_2 g}{R T_2}} \left(\frac{2}{\gamma_2 + 1} \right)^{\frac{\gamma_2 + 1}{2(\gamma_2 - 1)}}$$

where, in this case, the nozzle discharge coefficient is a constant:

for $A_s = 549.8$, $C_{d_s} = 0.9760$

and $A_s = 777.7$, $C_{d_s} = 0.9741$

AIRFLOW COEFFICIENT

Venturi-Venturi Centerbody Annulus

The flow coefficient at the annulus was calculated by

$$C_{f_{an}} = \frac{W_{a_s}}{W_{a_{an}}}$$

and the effective flow area was calculated by

$$A_{an_{eff}} = C_{f_{an}} \times A_{an}$$

Simulator Inlet

The flow coefficient at the inlet of the simulator was calculated by

$$C_{f_2} = \frac{W_{a_s}}{W_{a_2}}$$

MACH NUMBER

The Mach number at the simulator inlet was calculated by

$$M_2 = \sqrt{\frac{2}{(\gamma - 1)} \left[\left(\frac{P_2}{P_2} \right)^{\frac{\gamma-1}{\gamma}} - 1 \right]}$$

REYNOLDS NUMBER INDEX

The Reynolds number index at station 2 was calculated from

$$Re_{I_2} = \frac{\delta_2}{\phi_2 \sqrt{\theta_2}} = \frac{\delta_2 (T_2 + 199.5)}{718.2 \theta_2^2}$$

PRESSURE DISTORTION

Total pressure distortion was calculated at the simulator inlet (station 2) by

$$D = \frac{P_{2max} - P_{2min}}{P_{2avg}}$$

where the maximum and minimum pressures are chosen without regard for radial or circumferential location.

CORRECTED AIRFLOW

Corrected airflow through the simulator was calculated at the conic nozzle exit plane and corrected to conditions at sea level by the equation

$$W_{ac} = \frac{W_{a_s} \sqrt{\theta_2}}{\delta_2}$$

VENTURI INLET REYNOLDS NUMBER

The Reynolds number at the venturi inlet was calculated from the equation:

$$Re_D = \frac{\rho V D}{\mu} = \frac{W_a}{\mu} \frac{4}{\pi D} = 0.4129 \frac{W_a}{\mu}$$

where

ρ is the air density

V is the velocity

D is the diameter of the venturi inlet (37.0 in.)

μ is the viscosity of air and is calculated from Sutherland's formula

$$\mu = 2.270 \frac{T^{3/2}}{T + 198.6} \times 10^{-8}$$

NORMALIZED TURBULENT PRESSURE SPECTRAL DENSITY

The normalized turbulent pressure spectral density function was calculated by normalizing the power spectral density function by the equation

$$\frac{\left(\frac{\Delta P}{P}\right)^2}{B} = \frac{P S D}{P_2^2}$$

where P_2 is the steady-state total pressure at the simulator inlet and PSD is the power spectral density function which is computed by an electronic analog wave analyzer. The power spectral density function is presented graphically and represents a statistical estimation of the equation

$$P S D = \lim_{\substack{T \rightarrow \infty \\ B \rightarrow 0}} \frac{1}{TB} \int_0^T [f(t)]^2 dt$$

where T is the time length of the data sample considered, B is the bandwidth of the electrical filter used, and $f(t)$ is the instantaneous amplitude of the data waveform at time t . A value of B of 1.0 cps was used to obtain detailed frequency resolution of the data, and a value of 10.0 cps was used to obtain more general amplitude distribution with frequency. The time length of the data samples generally used was 4.0 sec.

NORMALIZED TURBULENT PRESSURE AMPLITUDE

The normalized turbulent pressure amplitude was calculated by

$$\left(\frac{\Delta P}{P}\right)_{\Delta f} = \frac{\Delta P_{\Delta f}}{P_2}$$

where $\Delta P_{\Delta f}$ is the average value of the peak-to-peak amplitude of the pressure waveform within the relatively broad frequency band, Δf .

Values of $\left(\frac{\Delta P}{P}\right)_{\Delta f}$ were also obtained by determination of the mean square value of the waveform amplitude between two given frequencies f_1 and f_2 by the expression

$$\left[\left(\frac{\Delta P}{P}\right)_{\Delta f}\right]_{\text{mean sq}} = A_{\Delta f}$$

where

$$\Delta f = f_2 - f_1$$

and $A_{\Delta f}$ is the area bounded by the normalized turbulent spectral density curve, the ordinate of the graph and two vertical lines, one drawn at frequency f_1 and the other at f_2 .

The mean square amplitude was then converted to a "psuedo" average peak-to-peak value by the expression

$$\left(\frac{\Delta P}{P}\right)_{\Delta f} \approx 2.828 \sqrt{\left[\left(\frac{\Delta P}{P}\right)_{\Delta f}\right]_{\text{mean sq}}}$$

The term "psuedo" is used because this expression is exact only if the waveform is purely sinusoidal.

AUTO-CORRELATION FUNCTION

The auto-correlation function, $R(\tau)$, was calculated by a digital computer and graphically presented as a statistical estimate of the function

$$R(\tau) = \lim_{T \rightarrow \infty} \frac{1}{T} \int_0^T f(t) f(t + \tau) dt$$

where τ is an induced time lag and $f(t)$ and $f(t + \tau)$ are the instantaneous amplitudes of the data waveform at time t , and at $(t + \tau)$, respectively. The auto-correlation function was used to determine the extent of the periodic content present in the data waveform.

STATISTICAL AMPLITUDE DISTRIBUTION PARAMETERS

As a quantitative measure of the nearness of the amplitude distribution to a Gaussian distribution, the skewness and kurtosis (sometimes called the "flatness") functions were calculated using a digital computer.

The computer program and statistical operations used to determine these functions are given in detail in Ref. 4. For a Gaussian distribution, the skewness and kurtosis functions have values of 0 and 3.0, respectively. The criteria used to determine the nearness of the amplitude distributions to a Gaussian or normal distribution were taken then to be

- (1) Skewness function near 0
- (2) Kurtosis function near 3.0
- (3) Little or no periodic content in the wave (determined from the auto-correlation and power spectral density functions).

Reference 5 uses the same criteria (with the exception of step (3), since no periodics appear to have existed in the Ref. 5 data) as given above to quantitatively describe the amplitude distribution of turbulent velocity data.

CORRECTION OF DYNAMIC DATA

Correction of dynamic pressure data was required for some parameters because of nonlinear frequency response characteristics of the pressure rake, or pressure rake-transducer combination. Figure I-1a shows the frequency response characteristics of a 27-in. tube and strain-gage transducer combination. The amplitude values for the tube-transducer combination were corrected by the equation

$$(\Delta P_{\text{actual}})_{\Delta f} = K_{\Delta f} \times (\Delta P_{\text{indicated}})_{\Delta f}$$

where

$(\Delta P_{\text{actual}})_{\Delta f}$ is the true amplitude of the wave within the bandwidth, Δf ,

$(\Delta P_{\text{indicated}})_{\Delta f}$ is the indicated amplitude of the wave within the bandwidth, Δf , and $K_{\Delta f}$ is given by the equation

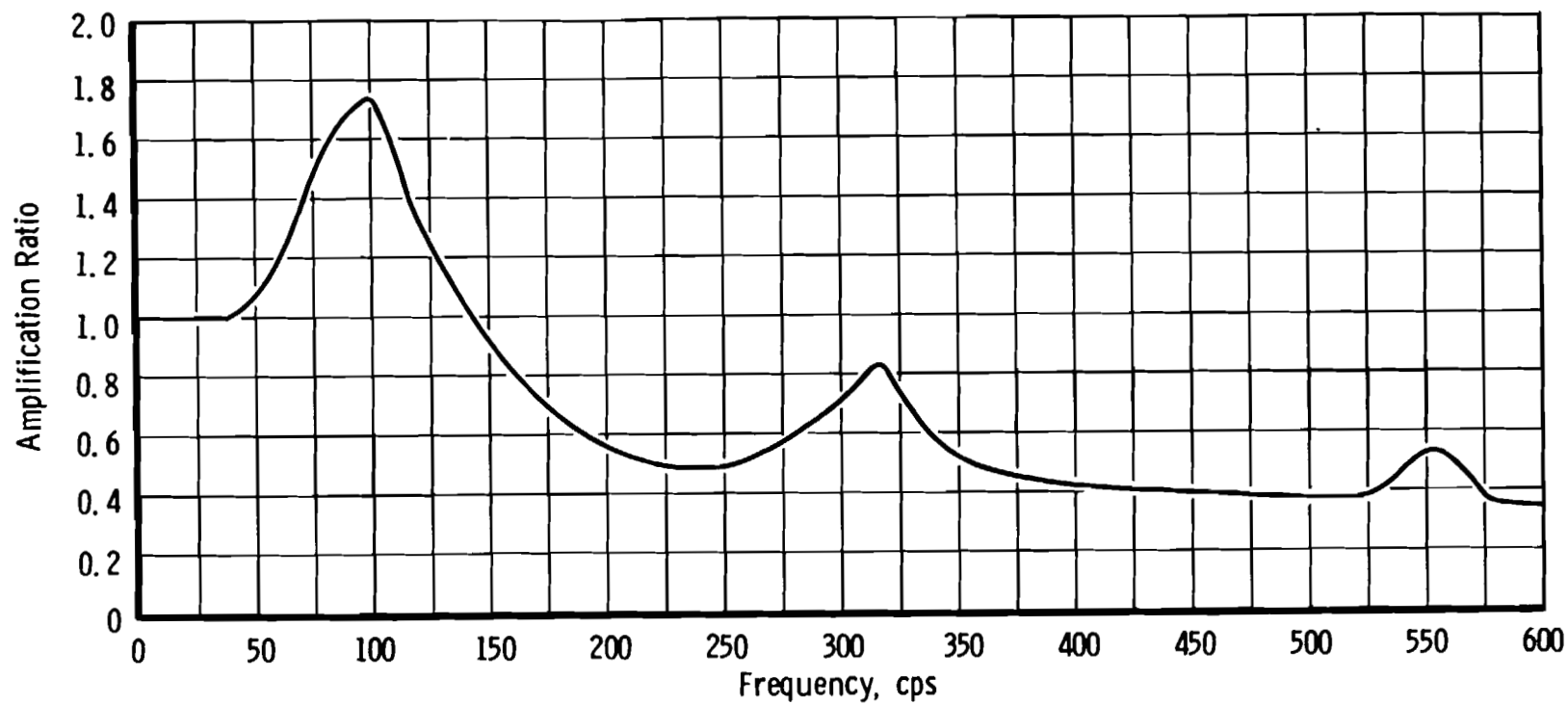
$$K_{\Delta f} = \sqrt{\frac{A_2}{A_1}}$$

A_1 and A_2 are the areas under the curves shown in Fig. I-1b. This technique is completely valid only for the case of a uniform frequency distribution of amplitude in the data and becomes a less effective correction as the spectral distribution deviates from the uniform case. Sample calculation of the effectiveness of the correction on several different sloping distributions indicate improvements in the data amplitude

such that indicated data values, which are on the order of 40 percent in error because of nonlinear response characteristics, are brought to within 10 percent of the true value.

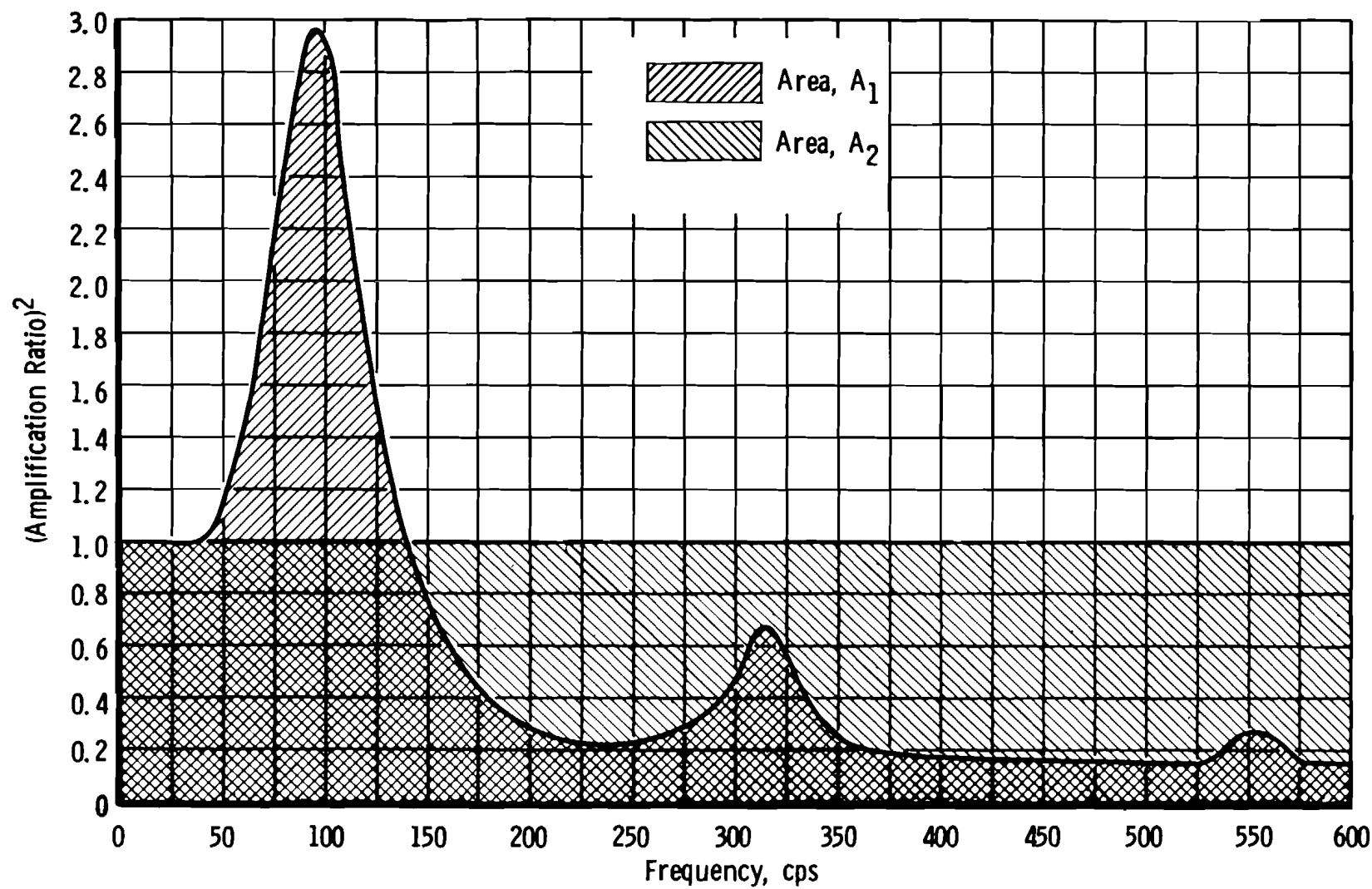
Figure I-2 illustrates a typical vibration response curve for the piezoelectric sensors mounted in a cantilevered single probe rake immersed in the stream. No correction can be reasonably made for the erratic response indicated, and therefore only the data within the frequency range from 0 to 200 cps are considered to be valid. The data above 200 cps were eliminated by an electronic blocking filter, or they were simply neglected in the spectral distribution presentations used in data analysis.

The data shown in Fig. I-3a were obtained from a variable capacitance wall static sensor. The sharp spikes which appear in the spectra show some correlation with the vibration of the duct in which the sensor was mounted (see Fig. I-3b). Cooling water flow through the sensor was also found to affect the data. Estimates of the random wall static pressure were made by neglecting the sharp spikes in measuring the area under the curve of a power spectral density plot using a planimeter.



a. Amplitude Ratio versus Frequency

Fig. I-1 Typical Frequency Response Characteristics for 27-in. Tube and Transducer Combination



b. Square of Amplitude Ratio versus Frequency

Fig. 1-1 Concluded

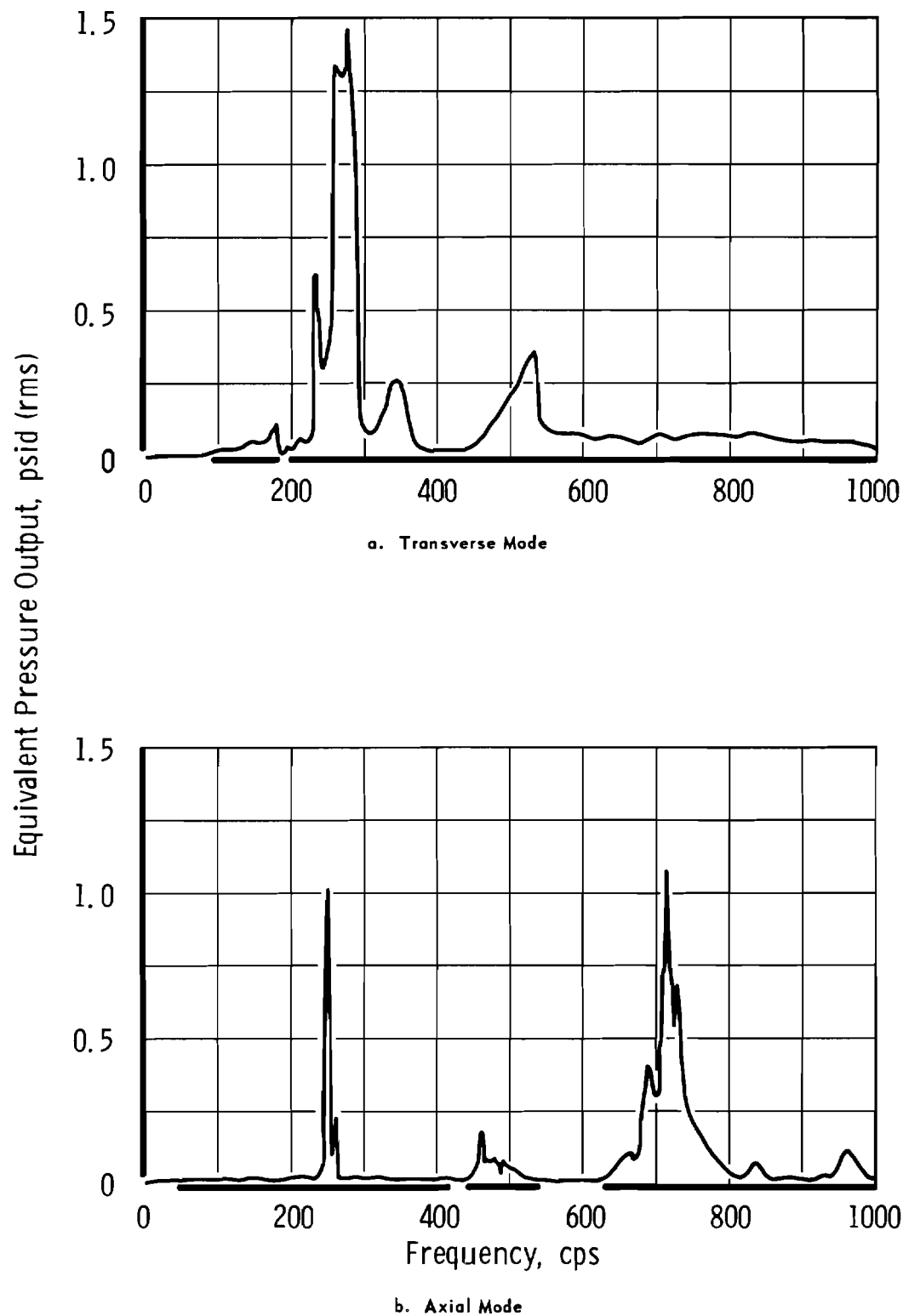
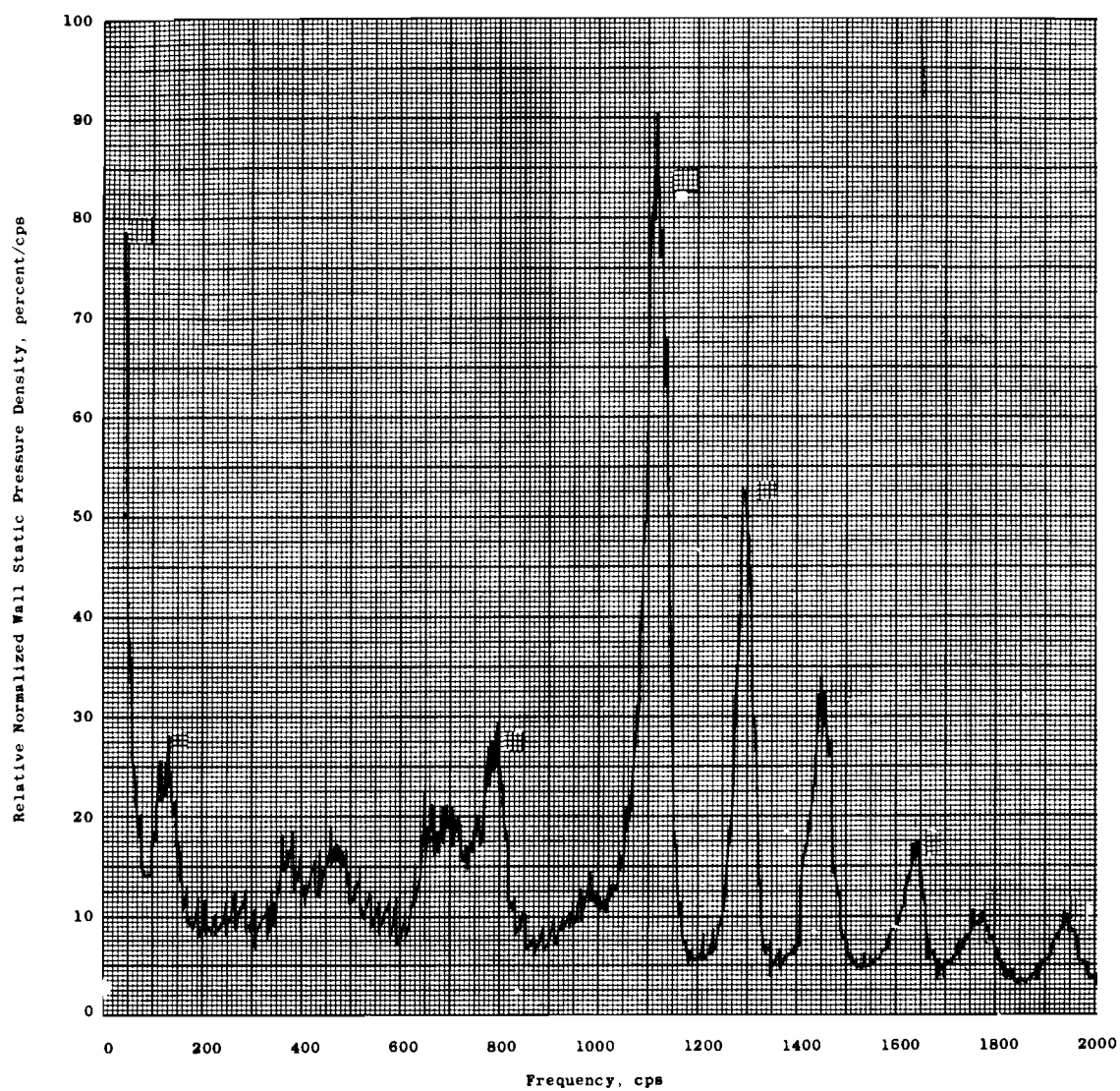
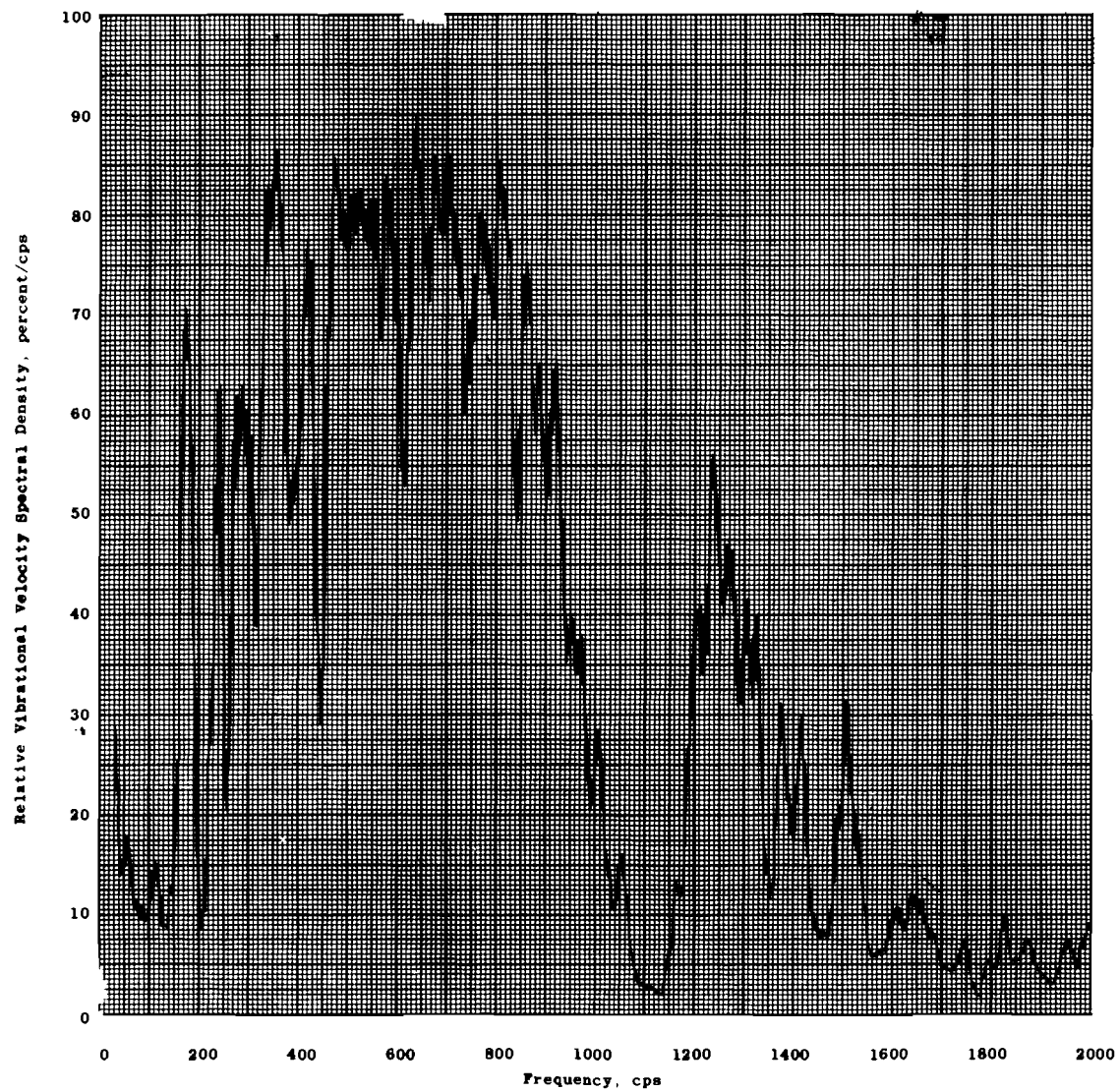


Fig. I-2 Typical Vibration Response for Piezoelectric Sensors Mounted in a Cantilevered Probe



a. Wall Static Pressure Spectrum

Fig. I-3 Correlation of Indicated Wall Static Pressure with Duct Vibration



b. Duct Vibration Spectrum

Fig. I-3 Concluded

DOCUMENT CONTROL DATA - R&D

(Security classification of title, body of abstract and indexing annotation must be entered when the overall report is classified)

1. ORIGINATING ACTIVITY (Corporate author) Arnold Engineering Development Center (AEDC), ARO, Inc. Operating Contractor, Arnold Air Force Station, Tennessee		2a. REPORT SECURITY CLASSIFICATION UNCLASSIFIED	
		2b. GROUP N/A	
3. REPORT TITLE AN INVESTIGATION AND CALIBRATION OF A DEVICE FOR THE GENERATION OF TURBULENT FLOW AT THE INLET OF A TURBOJET ENGINE			
4. DESCRIPTIVE NOTES (Type of report and inclusive dates) N/A			
5. AUTHOR(S) (Last name, first name, initial) Kimzey, W. F. ARO, Inc.			
6. REPORT DATE October 1965		7a. TOTAL NO. OF PAGES 142	7b. NO. OF REFS 6
8a. CONTRACT OR GRANT NO. AF40(600)-1200 b. System 110A c. Program Element 64403034 d.		9a. ORIGINATOR'S REPORT NUMBER(S) AEDC-TR-65-195 9b. OTHER REPORT NO(S) (Any other numbers that may be assigned this report) N/A	
10. AVAILABILITY/LIMITATION NOTICES Qualified requesters may obtain copies of this report from DDC. DDC release to CFSTI and foreign announcement and distribution of this report are not authorized.			
11. SUPPLEMENTARY NOTES N/A		12. SPONSORING MILITARY ACTIVITY Aeronautical Systems Division (ASD), Air Force Systems Command (AFSC), Wright-Patterson AF Base, Ohio	
13. ABSTRACT An investigation and calibration of a device consisting of an airflow metering venturi with a variable position aerodynamic centerbody for the production of turbulent flow at the inlet of a turbojet engine was conducted in an altitude test cell. The device provided turbulent flow conditions by producing shock-wave systems of variable severity. Turbulence and distortion values were obtained at the front face of a simulated turbojet engine compressor inlet located slightly downstream of the turbulence producing device. Various screen configurations with area blockages of from zero to 70 percent were inserted between the device and the simulator front face, and their effect on distortion and turbulence characteristics at several different corrected airflow settings was determined. Wave analysis techniques were applied to the turbulent pressure data, and the effects on turbulence of Reynolds number, corrected airflow, center- body position, and screen configuration were determined. Values of peak-to-peak turbulent pressure amplitude up to 28.4 (0- to 50-cps bandwidth) and 57.0 (0- to 600-cps bandwidth) percent of the steady- state total pressure level were obtained with total pressure distur- tion values up to 52 percent. An airflow coefficient for the turbulence generating device and the structural integrity of the apparatus were also determined.			

14 KEY WORDS	LINK A		LINK B		LINK C	
	ROLE	WT	ROLE	WT	ROLE	WT
turbulent flow						
inlet						
turbojet engines						
distortion						
shock waves						
structural integrity						
performance						

INSTRUCTIONS

1. **ORIGINATING ACTIVITY:** Enter the name and address of the contractor, subcontractor, grantee, Department of Defense activity or other organization (*corporate author*) issuing the report.

2a. **REPORT SECURITY CLASSIFICATION:** Enter the overall security classification of the report. Indicate whether "Restricted Data" is included. Marking is to be in accordance with appropriate security regulations.

2b. **GROUP:** Automatic downgrading is specified in DoD Directive 5200.10 and Armed Forces Industrial Manual. Enter the group number. Also, when applicable, show that optional markings have been used for Group 3 and Group 4 as authorized.

3. **REPORT TITLE:** Enter the complete report title in all capital letters. Titles in all cases should be unclassified. If a meaningful title cannot be selected without classification, show title classification in all capitals in parenthesis immediately following the title.

4. **DESCRIPTIVE NOTES:** If appropriate, enter the type of report, e.g., interim, progress, summary, annual, or final. Give the inclusive dates when a specific reporting period is covered.

5. **AUTHOR(S):** Enter the name(s) of author(s) as shown on or in the report. Enter last name, first name, middle initial. If military, show rank and branch of service. The name of the principal author is an absolute minimum requirement.

6. **REPORT DATE:** Enter the date of the report as day, month, year, or month, year. If more than one date appears on the report, use date of publication.

7a. **TOTAL NUMBER OF PAGES:** The total page count should follow normal pagination procedures, i.e., enter the number of pages containing information.

7b. **NUMBER OF REFERENCES:** Enter the total number of references cited in the report.

8a. **CONTRACT OR GRANT NUMBER:** If appropriate, enter the applicable number of the contract or grant under which the report was written.

8b, 8c, & 8d. **PROJECT NUMBER:** Enter the appropriate military department identification, such as project number, subproject number, system numbers, task number, etc.

9a. **ORIGINATOR'S REPORT NUMBER(S):** Enter the official report number by which the document will be identified and controlled by the originating activity. This number must be unique to this report.

9b. **OTHER REPORT NUMBER(S):** If the report has been assigned any other report numbers (*either by the originator or by the sponsor*), also enter this number(s).

10. **AVAILABILITY/LIMITATION NOTICES:** Enter any limitations on further dissemination of the report, other than those

imposed by security classification, using **standard statements** such as:

- (1) "Qualified requesters may obtain copies of this report from DDC."
- (2) "Foreign announcement and dissemination of this report by DDC is not authorized."
- (3) "U. S. Government agencies may obtain copies of this report directly from DDC. Other qualified DDC users shall request through _____."
- (4) "U. S. military agencies may obtain copies of this report directly from DDC. Other qualified users shall request through _____."
- (5) "All distribution of this report is controlled. Qualified DDC users shall request through _____."

If the report has been furnished to the Office of Technical Services, Department of Commerce, for sale to the public, indicate this fact and enter the price, if known.

11. **SUPPLEMENTARY NOTES:** Use for additional explanatory notes.

12. **SPONSORING MILITARY ACTIVITY:** Enter the name of the departmental project office or laboratory sponsoring (*paying for*) the research and development. Include address.

13. **ABSTRACT:** Enter an abstract giving a brief and factual summary of the document indicative of the report, even though it may also appear elsewhere in the body of the technical report. If additional space is required, a continuation sheet shall be attached.

It is highly desirable that the abstract of classified reports be unclassified. Each paragraph of the abstract shall end with an indication of the military security classification of the information in the paragraph, represented as (TS), (S), (C), or (U).

There is no limitation on the length of the abstract. However, the suggested length is from 150 to 225 words.

14. **KEY WORDS:** Key words are technically meaningful terms or short phrases that characterize a report and may be used as index entries for cataloging the report. Key words must be selected so that no security classification is required. Identifiers, such as equipment model designation, trade name, military project code name, geographic location, may be used as key words but will be followed by an indication of technical context. The assignment of links, rules, and weights is optional.